

AN ABSTRACT OF THE THESIS OF

Faye Lyn Barras for the degree of Doctor of Philosophy in Physics presented on June 12, 2014.

Title: First Principles Studies of Optical, Electronic and Mechanical Properties of Organic Molecules and Solids.

Abstract approved: _____

Guenter Schneider

This thesis presents the results of quantum-mechanical first principles calculations of optical, electronic and mechanical properties of organic molecules and solids, which have diverse potential applications such as photovoltaics, flexible electronics, and mechanical catalysts with applications in force sensors and self-healing materials.

The electronic and optoelectronic properties of organic thin films formed from π -conjugated molecules depends strongly on the packing of the molecules in the crystal and the presence of both donor and acceptor molecules. Based on a common backbone, for example anthradithiophene, the addition of sidegroups and endgroups changes both the packing and the electronic character of the molecule. The electronic and optical properties of two families of high performance organic materials functionalized with various side- and endgroups, anthradithiophene and indenofluorene, are studied using first principles density functional calculations. I report comprehensive independent particle properties including bandstructures, HOMO and LUMO levels and effective masses, as well as the formation of type II bulk heterojunctions between donor and acceptor molecules.

Mechanochemistry is a emerging field, which investigates the influence of mechanical action (forces, stress) on the direction, yield, and outcome of chemical reactions. In mechanocatalysis, mechanical force is used to break bonds in the molecule to activate a

catalyst, which can for example trigger a polymerization reaction in a self-healing material. First principles total energy calculations are used to investigate a potential mechanocatalyst based on a N-heterocyclic carbene, $C_{18}H_{25}N_3OS$. Rupture forces as a function of force loading rates are calculated using the COGEF (COntstrained Geometries simulate External Force) model. My theoretical results are in good agreement with experimental atomic force microscopy results.

©Copyright by Faye Lyn Barras

June 12, 2014

All Rights Reserved

First Principles Studies of Optical, Electronic and Mechanical Properties of Organic
Molecules and Solids.

by

Faye Lyn Barras

A THESIS

submitted to

Oregon State University

in partial fulfillment of
the requirements for the
degree of

Doctor of Philosophy

Presented June 12, 2014
Commencement June 2015

Doctor of Philosophy thesis of Faye Lyn Barras presented on June 12, 2014

APPROVED:

Major Professor, representing Physics

Chair of the Department of Physics

Dean of the Graduate School

I understand that my thesis will become part of the permanent collection of Oregon State University libraries. My signature below authorizes release of my thesis to any reader upon request.

Faye Lyn Barras, Author

ACKNOWLEDGMENTS

Academic

Primarily, I would like to acknowledge the support, ideas and opportunities my adviser, Guenter Schneider, has provided throughout my experience at Oregon State University. I would also like to thank my committee members, David Roundy, Janet Tate, and Oksana Ostraverkhova for their guidance. I would like to thank my collaborators: Randolph Beerwerth who worked with me on the indenofluorene molecules, and Monique Jacobs and Kerstin Blank who provided an experimental point of view for the mechanochemistry chapter. And finally, I want to thank the Oregon State University physics department and Oregon State University itself for the opportunity and support in my pursuit of this degree.

Personal

I would like to thank and acknowledge my parents for their financial and emotional support despite the long distance, my friends at Oregon State University for their support and encouragement, and my church family in Lebanon for all their encouragement, support, and prayers.

TABLE OF CONTENTS

	<u>Page</u>
1 INTRODUCTION	2
1 Charge transport, transfer and excitation	3
1.1 Charge transport theory	3
Hopping transport and Marcus theory	6
Band transport	8
1.2 Charge excitation and transfer	10
Excitons and Eximers	11
2 Covalent Mechanochemistry: breaking covalent bonds.....	15
2.1 Experimental Methods	16
2.2 Theoretical methods and history	17
2 ELECTRONIC STRUCTURE OF ANTHRADITHIOPHENE DERIVATIVES	18
1 Introduction.....	18
2 Theoretical Methods.....	20
3 Results and Discussion	23
3.1 Molecular properties	23
Ionization potential, Electron Affinity and HOMO-LUMO gap.....	23
Reorganization energies.....	26
3.2 Crystal properties.....	28
Geometries, band structures, and density of states	28
Effective masses	30
4 Summary and Conclusions.....	38
3 ELECTRONIC STRUCTURE OF INDENOFUORENE DERIVATIVES	41
1 Introduction.....	41
2 Theory and Methods	43
3 Results and Discussion	45
3.1 Molecular properties	45
HOMO-LUMO gap, Ionization potentials, and Electron Affinities.....	46

TABLE OF CONTENTS (Continued)

		<u>Page</u>
	Reorganization energies.....	48
	3.2 Crystal properties.....	50
	Geometries, band structures, and density of states	50
	Effective masses	55
4	Summary and Conclusions.....	58
5	Acknowledgments	60
4	<i>AB INITIO</i> CALCULATIONS TO EXPLORE COVALENT MECHANOCHEM- ISTRY	61
1	Introduction.....	61
2	Theory	61
	2.1 COGEF potential and the tilted potential energy surface	62
	2.2 Arrhenius model and the Harmonic approximation	65
	Morse potential model.....	67
	Analysis of the Arrhenius model in the context of the Morse potential ...	68
3	Small Molecules Test	70
	3.1 Curve crossing	75
4	Mechanocatalyst, C ₁₈ H ₂₅ N ₃ OS	78
	4.1 Theoretical calculations and tests	79
	Optimization of the relaxed molecule	81
	4.2 Adiabatic bond scission: desired bond	82
	4.3 Calculations for different bond breakage	85
	4.4 Molecular dynamics: different energy pathways	86
	Taking torsion angle and bond angles into consideration.....	87
	Molecular dynamics calculations comparison	88
	4.5 Theoretical results	90
	Fit to Arrhenius model	90
5	Summary and future research.....	91
6	Acknowledgements	92

TABLE OF CONTENTS (Continued)

	<u>Page</u>
5 SUMMARY	93
BIBLIOGRAPHY	95

LIST OF FIGURES

<u>Figure</u>	<u>Page</u>
1.1 Herringbone arrangement of (a) pentacene and (b) anthradithiophene. . .	4
1.2 HOMO (left) and LUMO (right) molecular orbitals (a) anthradithiophene, (b) fluorinated anthradithiophene functionalized with triisopropylsilylethynyl side groups (ADT-TIPS-F), and (c) indeno[1,2-b]fluorene. Functionalized derivatives such as ADT-TIPS-F also have their HOMO and LUMO orbitals located on the molecular backbone.	5
1.3 Free energy curves for the diabatic model. The red curve corresponds to the reactant, and the blue to the product. In the case of electron transfer for identical molecules, $\Delta G_0=0$ and the minima of the two curves would be at the same level. Note that the activation energy, ΔG^\ddagger , will increase as the spacing between $x_{R,0}$ and $x_{P,0}$ increases.	6
1.4 (a)Molecular structure of ADT-TES-F. The molecular orbitals of the HOMO (b) and LUMO (c) levels of ADT-TES-F are concentrated on the ADT backbone. The molecular orbital diagrams are the results of NWChem calculations and generated by ECCE. [21]	12
1.5 Schematic diagram of a type II heterojunction.....	13
1.6 HOMO and LUMO orbitals of two-molecule type II bulk heterojunctions. The HOMO and LUMO orbitals for the combination of ADT-TES-F with C ₆₀ ((a) and (b) respectively), and with ADT-TIPS-CN ((c) and (d) respectively) are shown. The minimum spacing between all the molecules is the same. An excimer is more likely to form if there is overlap between the HOMO and LUMO orbitals. The molecular orbitals are calculated using the application of density functional theory in NWChem [23], and the isosurface images have been generated in ECCE [21].	14
2.1 Molecular structures of (a) the <i>sys</i> -isomer of ADT, and (b) the <i>anti</i> -isomer of functionalized ADT. R ₁ =Si <i>i</i> -Pr ₃ (triisopropylsilyl), Si(CH ₂ CH ₃) ₃ (triethylsilyl) or (CH ₃ CH ₂ C(CH ₃)) ₃ Si (trise <i>c</i> -butylsilyl), and R ₂ =H, F, or CN. Diagrams of these side groups are illustrated in figure 2.2.	20
2.2 Diagrams of the side groups considered for these ADT derivatives: (a) triethylsilylethynyl (TES), -CSi(CH ₂ CH ₃) ₃ , (b)triisopropylsilylethynyl (TIPS), -CSi <i>i</i> -Pr ₃ =-CSi(CH(CH ₃) ₂) ₃ , and (c) trise <i>c</i> -butylsilylethynyl (TSBS), -CSi(C(CH ₃)CH ₂ CH ₃) ₃	21

LIST OF FIGURES (Continued)

<u>Figure</u>	<u>Page</u>
2.3 Crystal structure of ADT-TES-F. The a and b vectors define the plane of anthradithiophene backbones, while c links these planes. The anthradithiophene derivatives discussed in this chapter that have TIPS and TES side groups have similar structures.	24
2.4 (a)Molecular structure of ADT-TES-F. The molecular orbitals of the HOMO (b) and LUMO (c) levels of ADT-TES-F are concentrated on the ADT backbone. The molecular orbital diagrams are the results of NWChem calculations and generated by ECCE. [21]	25
2.5 Diagram comparing the HOMO and LUMO levels of ADT-derivatives. ..	26
2.6 Molecular structure of ADT-TIPS-CN overlaid with diagrams of the ADT backbone long axis (l_l), short axis (l_s), and backbone normal (ñ). This picture was generated using Ecce [21].	31
2.7 Band structures of single crystal anthradithiophene and derivatives ADT-TSBS-F, ADT-TES, and ADT-TIPS. The reciprocal coordinates of the high-symmetry points used in the band structures - Γ , X, N, Z, Y, L, R and M - are, expressed in terms of the reciprocal space lattice vectors, (0,0,0), (0.5,0,0), (0.5,0,0.5), (0,0,0.5), (0,0.5,0), (0.5,0.5,0), (0.5,0.5,-0.5) and (0,0,0.5,-0.5) respectively.	33
2.8 Band structures of single crystal anthradithiophene derivatives ADT-TES-F, ADT-TIPS-F, ADT-TES-CN and ADT-TIPS-CN. The reciprocal coordinates of the high-symmetry points used in the band structures - Γ , X, N, Z, Y, L, R and M - are, expressed in terms of the reciprocal space lattice vectors, (0,0,0), (0.5,0,0), (0.5,0,0.5), (0,0,0.5), (0,0.5,0), (0.5,0.5,0), (0.5,0.5,-0.5) and (0,0,0.5,-0.5) respectively.	34
2.9 Crystal structure and effective mass eigenvectors of ADT-based molecules. ADT, ADT-TSBS-F, ADT-TES and ADT-TIPS crystal structures are overlaid with their lattice vectors (green) and calculated effective mass eigenvectors for both holes (red) and electrons (blue). The label on each eigenvectors is the corresponding eigenvalue, the effective mass for that direction in units of electron mass. For each crystal structure, perspectives of a slice through the planes (upper) and of a single plane (the ab planes) (lower) are shown.	36

LIST OF FIGURES (Continued)

Figure	Page
2.10 Crystal structure and effective mass eigenvectors of ADT-based molecules <i>continued</i> . ADT-TES-F, ADT-TIPS-F, ADT-TES-CN and ADT-TIPS-CN crystal structures are overlaid with their lattice vectors (green) and calculated effective mass eigenvectors for both holes (red) and electrons (blue). The label on each eigenvectors is the corresponding eigenvalue, the effective mass for that direction in units of electron mass. For each crystal structure, perspectives of a slice through the planes (upper) and of a single plane (the ab planes) (lower) are shown.	37
3.1 Functionalized indeno[1,2-b]fluorene. (a) Molecular diagram. R' =H,F or Br, and TIPS =Si <i>i</i> -Pr ₃ (triisopropylsilyl). (b) Indenofluorene functionalized with TIPS side group and fluorene end groups (IF-TIPS-F). The second image was generated by ECCE. [21]	43
3.2 Diagram comparing the HOMO and LUMO levels of IF, IF-derivatives, ADT-TES-F, and C ₆₀ buckyball. These are results from calculations using NWChem [23] with the B3LYP functional and 6-31(1)G Gaussian basis set.	47
3.3 Charts showing intramolecular reorganization energies (meV) for holes λ_h and electrons λ_e of isolated molecules of the indenofluorene derivatives. The intramolecular reorganization energy for a hole(electron) $\lambda_{h(e)}$ is the sum of the relaxation energy of a cationic(anionic) molecule from the neutral geometry to the ionic geometry ($\lambda_{h(e)}^{+(-)} = E_0^{+(-)} - E_{+(-)}^{+(-)}$) and the relaxation energy of the neutral molecule from cationic(anionic) to neutral geometry ($\lambda_{h(e)}^0 = E_{+(-)}^0 - E_0^0$).[44] The reorganization energies for ADT-TES-F is included as a point of reference (see chapter 2)	49
3.4 Crystal structure of IF-TIPS-F. Vectors a and b define the plane of backbones, and c defines the vector crossing the planes. a is be the vector with the greatest component along the long axis (see figure 3.6) of the molecular backbone.	50
3.5 ab -plane of crystalline IF-TIPS. The structure has two nonparallel molecules per unit cell.de ^d	51
3.6 Molecular structure of IF-TIPS-F overlaid with diagrams of the indeno[1,2-b]fluorene skeleton's long axis (l_l), short axis (l_s), and backbone normal (n). This picture was generated using Ecce [21].	53

LIST OF FIGURES (Continued)

<u>Figure</u>		<u>Page</u>
3.7	Band structures of single crystal indenofluorene derivatives. The reciprocal coordinates of the high-symmetry points used in the band structures - Γ , X, Y, Z, L, M, N, R - are, expressed in reciprocal space lattice vectors, $(0,0,0)$, $(0.5,0,0)$, $(0,0.5,0)$, $(0,0,0.5)$, $(0.5,-0.5,0)$, $(0,0.5,0.5)$, $(0.5, 0, 0.5)$ and $(0.5,-0.5,0.5)$ respectively.	54
3.8	Crystal structure and effective mass eigenvectors of molecules with an indeno[1,2-b]fluorene skeleton. (a) IF-TIPS and (b) IF-TIPS-F crystal structures are overlaid with their lattice vectors (green) and calculated effective mass eigenvectors for both holes (red) and electrons (blue). The label on each eigenvector is the corresponding eigenvalue, the effective mass for that direction in units of electron mass. For each crystal structure, perspectives of a slice through the planes (upper) and of a single plane (the ab planes) (lower) are shown.	58
3.9	Crystal structure and effective mass eigenvectors of molecules with an indeno[1,2-b]fluorene skeleton <i>continued</i> . IF-TIPS-Br crystal structure is overlaid with its lattice vectors (green) and calculated effective mass eigenvectors for both holes (red) and electrons (blue). The label on each eigenvector is the corresponding eigenvalue, the effective mass for that direction in units of electron mass. For each crystal structure, perspectives of a slice through the planes (upper) and of a single plane (the ab planes) (lower) are shown.	59
4.1	Example of a potential energy surface with respect to a reaction coordinate, corresponding to a chemical reaction such as $[A] \rightleftharpoons [B] + [C]$	63
4.2	Model of a single C-N bond (see table 4.1). Morse potential with $D_e=340$ kJ/mol and $F_{max}=7.2$ nN with applied external forces of $F=0$ (black), $0.5 \cdot F_{max}$ (blue), $0.75 \cdot F_{max}$ (green) and F_{max} (red). These graphs correspond to a model for the C-N bond in dimethyl ammonium. F_{max} is the maximum slope of the potential, see equation 4.11. A positive force elongates the minimum energy bond length and lowers the activation energy required to break the bond.	64
4.3	Infinitely long one-dimensional diatomic molecule.	66

LIST OF FIGURES (Continued)

Figure	Page
4.4 Plot of a Morse potential with $D_e = 340$ kJ/mol and $F_{max} = 7.24$ nN. These values correspond to the values calculated for the C-N bond in dimethyl ammonium.	68
4.5 The effect of varying loading rates on the probability of bond breakage with respect to external applied force. Plot of probability of C-N bond breaking vs applied force for loading rates in powers of 10 from 10 pN/s to 100 mN/s, using a Morse potential model and Arrhenius kinetics at 300K with $D_e = 340$ kJ/mol and $F_{max}=7.2$ nN	69
4.6 The effect of increasing temperature from 200K to 400K (blue to red) in steps of 20K on the probability of bond breakage with respect to external applied force. A Morse potential model for the C-N bond and Arrhenius kinetics at 300K is used with $D_e = 340$ kJ/mol and $F_{max}=7.2$ nN. (a) is the plot of probability of a bond breaking vs applied force. (b) is the plot of	70
4.7 The effect of a change in the dissociation energy within a 25% range above (blue) and below (green) $D_e = 340$ kJ/mol on C-N bond breakage. A Morse potential with $F_{max}=7.2$ nN is assumed, and Arrhenius kinetics are applied under the conditions of 300K and loading rate 10 nN/s. The solid black lines correspond to $D_e = 340$ kJ/mol. (a) is a plot of probability vs applied force, and (b) demonstrates how	71
4.8 The effect of a change in the maximum force within a 25% range above (blue) and below (green) $F_{max}=7.2$ nN on C-N bond breakage. A Morse potential with $D_e = 340$ kJ/mol is assumed, and Arrhenius kinetics are applied under the conditions of 300K and loading rate 10 nN/s. The solid black lines correspond to $F_{max}=7.2$ nN kJ/mol.	71
4.9 (a) $H_3SiCH_2CH_3$, (b) $H_3SiCH_2CH_3$ (propane), (c) H_3CNHCH_3 (dimethyl ammonium), (d) H_3CNHCH_3 (dimethyl ether)	73
4.10 (a) COGEF potential for dimethyl ammonium overlaid with a Morse potential with the same dissociation energy (340 kJ/mol) and maximum slope (7.24 nN) for comparison. (b) Morse potential of (a) for DMA and its effective potential when a constant force of 2.59 nN is applied. The minimum (x_I) on the reaction coordinate shifts when a force is applied. .	74

LIST OF FIGURES (Continued)

<u>Figure</u>	<u>Page</u>
4.11 COGEF potential (black) and effective potential (blue) of dimethyl ammonium over which a Morse potential (red) and its effective potential (green) with dissociation energy of 1800 kJ/mol is laid for comparison. The maximum force of Morse potential is the same as that of the COGEF potential. A constant force of 2.59 nN is applied to the effective potentials as in figure 4.10. (b) is a wider perspective of (a) in order to compare the two D_e values.	75
4.12 (a) Probability vs applied force and (b) force vs $\log_{10}(\tau)$ and (c) bond strength (i.e. force at which the bond is most likely to break) vs loading rate for the small molecules considered in table 4.1. The loading rate is set at 10 nN/s and the Arrhenius model was used calculate this data. The temperature was set to 300 K.	76
4.13 COGEF potentials of (a) SiC2H8 and (b) propane for longer ranges of the reaction coordinates. The NWChem calculations for longer ranges jump between the singlet and triplet state for the two molecule product. Results using Gaussian basis sets dzp_dunning (black) and 6-311++g3df_3pd (blue) are shown.	77
4.14 COGEF potentials of (a) SiC2H8 and (b) propane where the singlet state is specified in the NWChem input files (black), where the triplet state energy is calculated from each optimized singlet step (blue), and where the initial relaxed state (singlet) is stretched, but with triplet state specified (green). The singlet and triplet curve crossings occur just after the maximum force (circled in red on the graphs). The Gaussian basis set dzp_dunning was used in all these calculations.	78
4.15 Results from AFM experiments performed by Monique Jacobs [26]. The central part of the red molecule is the focus of this section. The multiple peaks in the number of events with respect to applied force indicates that at least two different bonds broke. The force loading rates recorded for these experiments were on the order of 0.1 nN/s. Used with permission.	79
4.16 (a) Closer picture of the relevant section of the mechanocatalyst in figure 4.15. The black line indicates where the molecule needs to break in order to activate the catalyst. (b) Diagram of the NHC-NCS molecule with the catalyst, <i>N</i> -heterocyclic carbene, highlighted.	80

LIST OF FIGURES (Continued)

<u>Figure</u>	<u>Page</u>
4.17 The C ₁₈ H ₂₅ N ₃ OS molecule in its unstretched state. The numbers overlaid on the atoms are for referencing different bonds and anchor atoms. The line labeled z=r(C0-C13)) indicates the reaction coordinate described as the distance between carbon atoms C0 and C13. Increasing this distance stepwise, produces a desired scission.....	80
4.18 Representation of two relaxed structures of NHC-NCS. The lowest energy structure (a) has free energy -1338.348 Ha and torsion angle 58.8°, and another geometry that appears to be a local minimum (b) with free energy -1338.333 Ha and torsion angle 104.1°. Most of the NCS part of the molecule is in a plane, and the torsion angle is defined by atoms S46, C16, C17 and N44 (see figure 4.17 for atom numbers). The free energies are those calculated with the 6-31G basis set.	83
4.19 COGEF potential for the NHC-NCS molecule with reaction coordinate C0-C13. The 6-31G basis set has been used in each step. The blue line is the COGEF potential of the lowest energy starting structure, figure 4.18(a), and the green line corresponds to figure 4.18(b) at step 0. From the graph it is evident that that both COGEF potentials merge before the C16-C17 bond breaks. The steps progress by stretching the molecule in increments of 0.1 Å.	84
4.20 COGEF potential for C ₁₈ H ₂₅ N ₃ OS. Atoms C0 and C13 (see figure 4.17) are the anchor atoms defining the reaction coordinate. Stretching along this reaction coordinate produces a desired scission between atoms C16 and C17 as indicated in figure 4.17.	85
4.21 (a) Diagram of the the torsion angle defined by the S46-C16-C17-N44 bond. This torsion angle increases as the molecule is stretched. (b) shows the context in the molecule of the magnified section in (a).	87

LIST OF FIGURES (Continued)

<u>Figure</u>	<u>Page</u>
4.22 Torsion angle (left scale) versus reaction coordinate C0-C13, overlaid with COGEF potential (right scale, black). The torsion angle is defined as counterclockwise rotation about the C16-C17, where atoms S46, C16, C17 and N44 fully define the torsion. The blue line is the torsion angle after each step has being optimized, and the green is the torsion angle after the stretch for each step, but before optimization. This plot shows that the molecule can be considered as two parts joined by the C16-C17 bond. The parts rotate with respect to each other as the molecule is stretched. The 6-31G basis set was used in the COGEF potential calculation.....	89
4.23 (a) Probability vs applied force and (b) force vs $\log_{10}(\tau)$ and (c) bond strength (i.e. force at which the most bonds break) vs loading rate for reaction coordinates of of $C_{18}H_{25}N_3OS$ considered in table 4.4. The loading rate is set at 1 nN/s and the Arrhenius model was used calculate this data. The temperature was set to 300 K. (d) is the color key for these graphs. Each color corresponds to a specific bond that broke when the molecule was stretched. Multiple lines of the same color correspond to the same bonds breaking when different anchor atoms are chosen. There is not significant variation in these lines within the limits of the Morse potential model.	91

LIST OF TABLES

<u>Table</u>	<u>Page</u>
2.1 Table of chemical formulas, and experimental and calculated HOMO-LUMO gaps (in eV) for isolated molecules of the ADT derivatives.	27
2.2 Vertical and adiabatic ionization potentials and electron affinities for the ADT-derivatives (in eV) for isolated molecules. Here we define $IP = E(M^+) - E(M)$ and $EA = E(M^-) - E(M)$. The final column, $IP + EA_{adiabatic}$ is the sum of the adiabatic ionization potential and electron affinity for each molecule. Ideally, in a calculation with no approximations, this would equal the HOMO-LUMO gap of the molecule.	28
2.3 Intramolecular reorganization energies (meV) for holes λ_h and electrons λ_e of isolated ADT derivative molecules.	29
2.4 Lattice parameters for anthradithiophene derivative single crystals. The volume quoted is the volume per molecule.	31
2.5 Orientation of molecules with respect to the lattice. Each column lists the angle between the two vectors indicated at the top of the column. $\hat{\mathbf{n}}$ represents the vector perpendicular to the ADT backbone of the molecules, and \mathbf{l}_s and \mathbf{l}_l represent the short and long axes of the ADT backbone. Figure 2.6 illustrates these vectors for ADT-TIPS-CN. The distance between lattice planes (\mathbf{c}_\perp) and angle of \mathbf{a} with respect to the \mathbf{ab} -plane normal are also listed for each crystal.	32
2.6 HOMO-LUMO gaps and band dispersions of the HOMO and LUMO bands for single crystal ADT derivatives (in eV), calculated using GGA in PW91.	35
2.7 Effective mass eigenvalues and eigenvectors for holes and electrons of the anthradithiophene derivatives. The eigenvectors are expressed as components of the normalized real-space lattice vectors, $\hat{\mathbf{a}}$, $\hat{\mathbf{b}}$ and $\hat{\mathbf{c}}$. Table 2.4 gives the lattice parameters of the real-space lattice vectors. All effective masses are quoted in units of m_e , i.e. $m^* = m_{\text{eff}}/m_e$	40

LIST OF TABLES (Continued)

<u>Table</u>	<u>Page</u>
3.1 Table of calculated HOMO-LUMO gaps for isolated molecules. The molecules considered are indeno[1,2-b]fluorene (TIPS) and derivatives of IF that have been functionalized on either side with a triisopropylsilylethynyl (TIPS) side groups. Derivatives with fluorine (F), bromine (Br) or no end groups have been considered. The experimentally determined band gap for IF-TIPS is 1.9 eV [57]. The B3LYP column corresponds to results calculated using NWChem, and the GGA column is for results calculated in VASP when each molecule is surrounded by vacuum. All values are in units of electron volts.	47
3.2 Vertical and adiabatic ionization potentials and electron affinities for IF-derivatives for isolated molecules (in eV). Here we define $IP = E(M^+) - E(M)$ and $EA = E(M^-) - E(M)$. $IP+EA_{adiabatic}$ is the sum of the adiabatic ionization potential and electron affinity for each molecule.	48
3.3 Chemical composition and experimental lattice parameters for indenofluorene derivatives with TIPS side groups. IF-TIPS has two molecules per unit cell. Note: The volume V_m quoted is the volume per molecule.	51
3.4 Orientation of molecules with respect to the lattice. Each column lists the angle between the two vectors indicated at the top of the column. $\hat{\mathbf{n}}$ represents the vector perpendicular to the indenofluorene (IF) backbone of the molecules, and \mathbf{l}_s and \mathbf{l}_l represent the short and long axes of the IF backbone. Figure 3.6 illustrates these vectors for IF-TIPS-F. The distance between lattice planes (\mathbf{c}_\perp) and angle of \mathbf{a} with respect to the \mathbf{ab} -plane normal are also listed for each crystal.	52
3.5 Details about the valence and conduction bands for single crystals of each indenofluorene derivative, including the band dispersions. The valence band maxima (VBM) correspond to the HOMO levels of the isolated molecules, and the conduction band minima (CBM) with the LUMO levels. The symbols used for the k-points correspond to those described in figure 3.7. These values are calculated using the PBE functional in VASP. All values quoted are in eV. The calculated values for anthradithiophene with trisopropylsilylethynyl and fluorine end group substituents (ADT-TES-F) serve as reference points.	55

LIST OF TABLES (Continued)

<u>Table</u>		<u>Page</u>
3.6	Effective mass eigenvalues and eigenvectors for holes and electrons of single crystal indenofluorene derivatives. The eigenvectors are expressed in terms of components of the normalized real-space lattice vectors, $\hat{\mathbf{a}}$, $\hat{\mathbf{b}}$ and $\hat{\mathbf{c}}$. All effective masses are quoted in units of m_e	57
4.1	Table of dissociation energies and maximum forces extracted from COGEF potentials of four test molecules. The second column indicates which bond broke in each molecule. The last two columns of this table are published values calculated using the program Gaussian with basis set D95(d,p) [60]. The reaction coordinate of each molecule is the distance between the two farthest spaced hydrogen atoms in the molecule.	74
4.2	Table of data extracted from COGEF potentials of $\text{C}_{18}\text{H}_{25}\text{N}_3\text{OS}$. The reaction coordinate (x) is the distance between two carbon atoms at the extremities of the molecule indicated in figure 4.17.	84
4.3	Table of data maximum force extracted from COGEF potentials of $\text{C}_{18}\text{H}_{25}\text{N}_3\text{OS}$, where the step size is varied. The reaction coordinate is defined as the distance between two carbon atoms at the extremities of the molecule indicated in figure 4.17, and the 6-31G basis set has been used.	85
4.4	Table of data extracted from COGEF potentials of $\text{C}_{18}\text{H}_{25}\text{N}_3\text{OS}$. The reaction coordinate (z) is the distance between two carbon atoms at the extremities of the molecule indicated in figure 4.17. The 3-21G Gaussian basis set was used in these calculations.	86

**FIRST PRINCIPLES STUDIES OF OPTICAL, ELECTRONIC AND
MECHANICAL PROPERTIES OF ORGANIC MOLECULES AND
SOLIDS.**

1 INTRODUCTION

Organic materials differ from atomic or ionic crystals in that the bonding between the molecular components is due to much weaker van der Waals interactions as opposed to covalent or ionic bonds. The intramolecular bonding in organic molecules themselves, however, is defined by covalent bonds.

The weak intermolecular bonding results in lower charge mobility in organic crystals and thin films when compared to inorganic materials such as Si. The mechanical and elastic properties of the crystal are directly affected by the van der Waals bonding between the molecules. Organic crystals are highly compressible, and have low mechanical strength and low melting and sublimation temperatures.[1, 2] These materials also have poor conduction of electric charge due to the weak electronic coupling between the molecule.[3, 4, 5] However, organic solids have the advantage of being solution processable, flexible, and have low production costs.[6, 7] Furthermore, organic crystals have tunable optical and electronic properties,[8] and have interesting features that are not or only weakly present in inorganic materials that are a consequence of charge carriers having the tendency to be localized on individual molecules. Frenkel exciton formation, excimer formation and hopping transport are a few such properties related to charge carrier localization on the molecule.[1]

The use of mechanical force to influence and guide chemical reactions has gained considerable interest in recent years and has been termed Mechanochemistry.[9] A particular interesting application is the breaking of covalent bonds within a molecule using mechanical force, which can be used in force sensors or to activate a catalyst, which in this context is called a mechanocatalyst. Latent mechanocatalysts are large organic molecules where a catalyst is incorporated into the molecular structure and which can be activated by breaking specific bonds within the molecule using mechanical force. One potential appli-

cation is in self-healing materials, where for example the activation of the latent catalyst starts a polymerization reaction.

1 Charge transport, transfer and excitation

Charge transport and transfer properties are largely governed by the relatively weak intermolecular bonding that creates a competition between the localization of charge carriers on each molecule, and delocalization over the entire lattice. Whether a charge carrier or exciton is constrained to stay on a molecule or whether it can travel through the crystal or film is strongly dependent on the molecular structure itself as well as the arrangement of the molecules.

Lattice vibrations (phonons) and molecular vibrations, crystal defects, polarization, and temperature and pressure are a few effects that combine to aid or hinder transport throughout a crystal. If it is possible for a charge carrier to travel through a crystal, it is accompanied by local electronic and nuclear polarization "clouds" which make the charge carrier bulkier and heavier, essentially making the conduction levels of charge carriers the conduction levels of polarons. Another localization effect is that of an optical excitation in an organic molecule which may lead to the formation of an exciton. The large binding energies within organic excitons are the cause of the separation into charge carriers, a hole and an electron, being one of the central problems in organic electronics.

1.1 Charge transport theory

In π -conjugated organic molecules, such as anthradithiophene, the charge carrier is most likely to reside on the π -conjugated molecular backbone,[10] which is delocalized (in the aromatic case) over the pi-orbitals of carbon bonds in the π -conjugated rings. The intermolecular transfer integral, t , is one of the key charge transport parameters at the microscopic level. This values expresses how easily a charge carrier is transferred

between two adjacent molecules and describes the electronic coupling between two adjacent molecules. t is directly related to the degree of orbital overlap of the highest occupied molecular orbitals (HOMO) or the lowest unoccupied molecular orbital (LUMO). In a band structure picture, the transfer integral is related to the width of the valence and conduction bands, which respectively correspond to the HOMO and LUMO orbitals.[11]

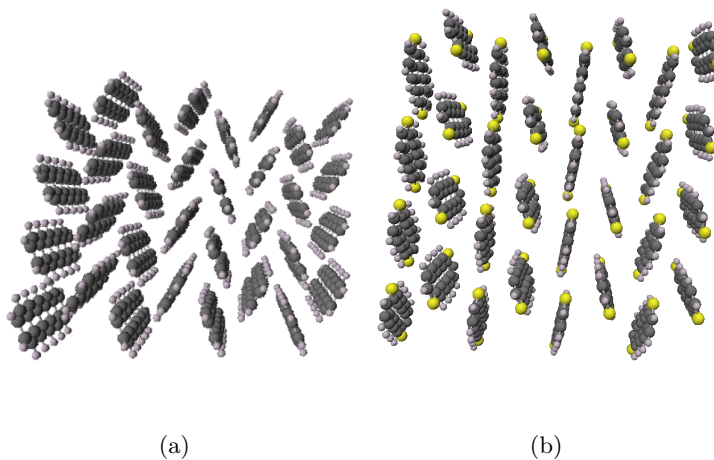


FIGURE 1.1: Herringbone arrangement of (a) pentacene and (b) anthradithiophene.

With sufficient intermolecular overlap between the π -orbitals in adjacent molecules in perfectly ordered materials, coherent band-like transport may occur at low temperatures. π -conjugated molecules such as pentacene, anthradithiophene or indenofluorene have crystal lattices with herringbone-like ordering (also known as Ac-type crystals, where there are two non-parallel near-neighbor molecules in a unit cell [1]), see figure 1.1.[10, 12] In these configurations, the planar molecular backbone are at angles with respect to each other and do not allow for optimal overlap of the π -orbitals centered on the backbone, see figure 1.2. A better overlap would occur if the backbones were parallel to each other, provided that there was not too much offset between neighboring molecules. Functionalization of these π -conjugated molecules has been shown to force the crystal structure of these molecules into an arrangement where the molecular backbone planes are oriented

parallel with each other as opposed to a herringbone-type arrangement.[10, 13, 14]

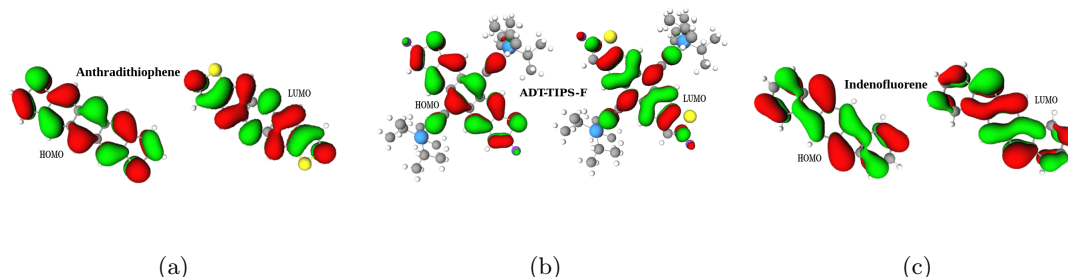


FIGURE 1.2: HOMO (left) and LUMO (right) molecular orbitals (a) anthradithiophene, (b) fluorinated anthradithiophene functionalized with triisopropylsilyl ethynyl side groups (ADT-TIPS-F), and (c) indeno[1,2-b]fluorene. Functionalized derivatives such as ADT-TIPS-F also have their HOMO and LUMO orbitals located on the molecular backbone.

The electronic structure of organic molecular crystals has also been described as islands of charge density separated by channels of electronless space.[1, 2] From this point of view, charge transport can only occur if the charge carrier hops between neighboring molecules. This is a better description for higher temperatures where the effective bandwidths are narrowed due to scattering of the charge carriers by phonons in the system.[11] Once again, the transfer integral, and consequently HOMO(LUMO) molecular orbital overlap, is important for charge transport. The stronger the electronic coupling between the molecules, the higher the likelihood of the occurrence of hopping transport.

The eigenvectors corresponding to the lowest effective masses derived from *ab initio* density functional theory calculations of the band structure of an organic molecular crystal give a good approximation for the directions in the crystal that have the best HOMO (highest occupied molecular orbital) or LUMO (lowest occupied molecular orbital) orbital overlap, and are thus most favorable for band-like and hopping transport.

The average velocity of a charge carrier through a crystal is given by the mobility of the carrier multiplied by the applied electric field. In the case of an anisotropic crystal, the mobility will be tensor. Mechanisms of charge carrier transport in organic molecular

crystals can be separated into two main categories: tunneling (coherent) transport and hopping (incoherent) transport. Both of these contribute additively to the overall mobility of the crystal (equation 1.1).[15]

$$\mu = \mu_{tun} + \mu_{hop} \quad (1.1)$$

Hopping transport and Marcus theory

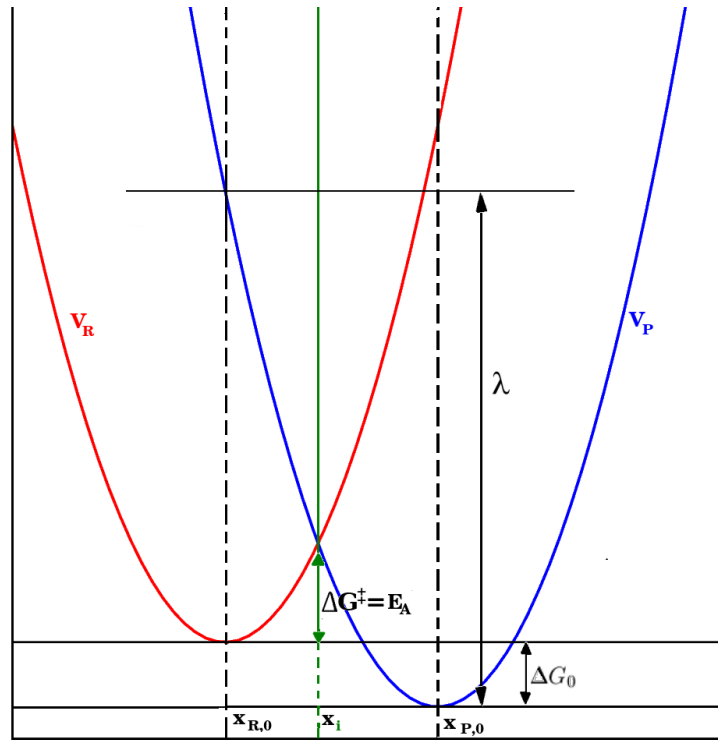


FIGURE 1.3: Free energy curves for the diabatic model. The red curve corresponds to the reactant, and the blue to the product. In the case of electron transfer for identical molecules, $\Delta G_0=0$ and the minima of the two curves would be at the same level. Note that the activation energy, ΔG^\ddagger , will increase as the spacing between $x_{R,0}$ and $x_{P,0}$ increases.

Hopping transport is a temperature activated mechanism, and can be described as a reaction where the charge carrier (electron or hole) is transferred from one molecule to an identical neighboring molecule.



A useful illustration of this reaction is the so called diabatic model[16, 17]. Here, the potential energies of two molecules are modeled as two adjacent parabolas ($V_R = \frac{1}{2}k(x - x_{R,0})^2$ and $V_P = \frac{1}{2}k(x - x_{P,0})^2 + \Delta G_0$) that have the same width but different positions along the reaction coordinate, see figure 1.3. Neglecting entropy, the free energy barrier is given by $\Delta G = V_R(x_i) - V_R(x_R)$, where x_i is the intersection between the two parabola. The reorganization energy, λ , is the difference in energy on the product potential V_P between the positions corresponding to the minima of the reactant and products, $x_{R,0}$ and $x_{P,0}$ respectively. In other words the reorganization energy is the energy required to rearrange the electronic and ionic configurations of a molecule as it changes from neutral to charged as charge transfers onto the molecule. The total difference in free energy can be written in terms of the reorganization energy as $\Delta G = \frac{1}{4\lambda}(\lambda + \Delta G_0)^2$. [16] Given that the molecules are identical ($\Delta G_0 = 0$), the rate constant k_T for hopping between neighboring molecules is described by Arrhenius kinetics for a reaction,

$$k_T = A \exp \left[\frac{-\lambda}{4k_B T} \right] \quad (1.3)$$

The reorganization energy in equation 1.3 is strongly dependent on the distance between the charges as well as the reorganization of the electronic structure of the molecules due to a charge being added or removed. From another perspective, hopping charge transfer is more probable if the electronic coupling between adjacent molecule, represented by the transfer integral T which can be determined from a tight-binding approximation, is higher. Furthermore, t is exponentially related to the distance between the two molecules. The same trend is reflected in the diabatic model. The activation energy of a charge transfer has a squared dependence on the distance between the two molecules ($x_{P,0} - x_{R,0}$). This brings us back to the picture of the molecules as islands of electron density in a sea of electronless space: it becomes harder to transfer electrons between islands if there is more 'sea' between the islands.

When motion within a film or crystal is described as a series of uncorrelated hops, the mobility is given by 1.4.[10]

$$\sigma = \frac{ea^2}{k_BT}k_T \quad (1.4)$$

In equation 1.4, a is the distance between molecules, and k_T is the electron (or hole) transfer rate. k_T is strongly dependent on the intermolecular transfer integral (J) and the reorganization energies.

Band transport

Band transport, sometimes called tunneling transport,[11] is described in lowest order by the Drude model, which can be derived from quantum many-body theory.[18] In the original, simple derivation, the Drude model describes a gas of charged electrons. In a metal the much heavier ions are at fixed positions within the gas and the electrons are assumed to be free and independent. In other words, the valence electrons are not constrained to the environment of a particular ion, but can move freely throughout the crystal, not interacting with other electrons or ions unless there is a collision. The second assumption is that the collisions are instantaneous, and randomly alter the velocity of the electrons. These collisions are assumed to be between ions in the lattice. Applying these assumptions, with an average collision time τ in a constant electric field, the average velocity of an electron is given by

$$\mathbf{v}_{\text{avg}} = -\frac{e\mathbf{E}\tau}{m} \quad (1.5)$$

In an isosymmetric crystal, $\mathbf{E} = \mathbf{j}/\sigma$, and the conductivity of a crystal becomes

$$\sigma = \frac{e\tau(T)}{m_{\text{eff}}} \quad (1.6)$$

In equation 1.6, n is the number of electrons per unit volume. The Sommerfield theory of metals improves on the Drude model by taking into account the Pauli exclusion principle, which leads to a change of the electronic velocity distribution to the quantum mechanical

Fermi-Dirac distribution.[19] Drude’s model and the Sommerfield theory of metals can be expanded to apply to three dimensional inorganic crystals by using a semiclassical model. A semiclassical model allows us to make a band-like approximation for the conductivity of holes and electrons within the valence and conducting bands. Only partially filled bands, such as the valence band missing an electron (hole transport) or the conduction band containing an electron excited from the the valence band, are relevant to conduction. After calculating the band structure of the crystal using density functional theory, it is assumed that the charge does not transfer to a different band.

Within a single band the effective mass in equation 1.6 is given by

$$\left(\frac{1}{m^*}\right)_{ij} = \frac{1}{\hbar^2} \frac{\partial^2 E(\mathbf{k})}{\partial k_i \partial k_j}. \quad (1.7)$$

Equation 1.7 can be derived from this semiclassical theory, and relates the effective mass tensor of a hole(electron)to the valence(conduction) band energies with respect to \mathbf{k} -space. Since the effective mass, m_{eff} , of the electron or hole is a tensor, it is dependent on the direction of propagation.

Assuming a periodic crystal, the band structure is calculated using Bloch wave functions. However, this is not a sufficient condition for band transport. Excluding effects such as lattice and molecular vibrations in the crystal, there has to be enough intermolecular electronic coupling between molecules for band-like transport to occur. Thus, the band-like theory for charge transport works better for inorganic crystals where there are less localization effects. Intramolecular bonding in organic molecules is covalent, so delocalization of charge carriers within the molecules is expected, however the HOMO and LUMO have to have sufficient intermolecular overlap for charge carriers to be delocalized over multiple molecules. The lower effective mass eigenvalues correspond to higher band widths. The eigenvectors that correspond with these lower effective masses indicate the directions in which the crystal is likely to have a higher degree of molecular orbital overlap.

Band-like transport is only likely to occur at low temperatures when phonon scat-

tering and molecular vibrations are not present to decrease the effective band width. The condition that the mean free path of a charge carrier in a crystal is much greater than the lattice vectors is necessary. The lower the effective mass vector, the higher the order of delocalization, which directly corresponds to the band width.

With increasing temperature, the number of crystal phonons and molecular vibrations increases, and the molecule is more likely to experience hopping or tunneling transport.[1] However, as stated earlier, band effective masses in conjunction with equation 1.6 can be used as a comparative guide for conductivity within organic crystals. Organic crystals tend to have the best conductivity in the direction where the orbitals of the molecules have the most overlap in the crystal, particularly when aromatic *pi*-conjugated orbitals are involved. In these instances, charges are delocalized over the orbital on the backbone of the molecule and, in cases where the orbital overlap is also good, can result in relatively high conduction values.[10] For example, the π -conjugated materials described in chapters 2 and 3 have lower effective mass when the molecules are arranged in such a manner that π bonds, which are the main contributors to the wave functions of the valence and conduction bands, have the most overlap.

1.2 Charge excitation and transfer

In order for effective functionality of electronic devices such as field effect transistors or solar cells, charge carriers need to be generated and transported through a film or crystal, as well as transferred between different materials. When a molecule in a crystal is excited by a photon large enough to overcome the energy band gap, an electron is excited from the occupied orbitals (usually the HOMO) into the unoccupied orbitals. The properties of the molecule and its environment will determine what will happen to this excited electron. Localization effects in an organic molecular crystal tend to be relatively strong, so the excited electron may be trapped with the associated hole as an exciton on the molecule or recombine completely. Another case is the exciton being transported through

the crystal but then recombine with a different hole on a different molecule. Instead of unimolecular recombination, bimolecular combination may occur where an electron and hole each on two adjacent molecule form a charge transfer state and will either recombine through radiative or nonradiative pathways, or separate for charge conduction depending on the local conditions.[20] Thus charge separation and recombination are key factor affecting transport in a crystal.

Excitons and Eximers

The higher degree of localization that occurs in organic molecular crystals increases the likelihood of exciton and eximer formation. An exciton is the bond state between an electron and a hole, two particles of opposite charge that are attracted to each other by Coulomb's electrostatic force. There are two general categories of excitons: Frenkel excitons and Wannier excitons. Frenkel excitons are excitons occur where the electrostatic interaction between the electron and hole is relatively strong and the physical range of the exciton is on the order of a unit cell - or in the case of organic molecular crystal, molecular excitons can occur, where the exciton is entirely localized on a molecule. Frenkel excitons occur when there is a low dielectric constant, and consequently less shielding of the Coulomb interaction. The other type of exciton, Wannier-Mott excitons are more likely to occur in inorganic solids. These are excitons whose size is larger than a unit cell, and thus have much lower binding energies compared to Frenkel excitons. This means that the energy levels of the electron and hole will be just slightly within the edges of the semiconductor band gap. Transport of excitons within an organic molecular crystal may also occur, and may be used to carry an exciton to an electron trap so that the hole is available for further transport. An exciton has the advantage over a single charge carrier in that it is neutral and thus has less lattice and molecular polarization effects, however exciton transport is not a focus in my thesis.

In a semiconductor, an electron and hole are created when the electron is excited

(usually photo-excited) from its ground state into the conduction band. If the Coulomb force between the particles is strong enough and the electron and hole molecular orbitals (HOMO and LUMO) have sufficient overlap, the two can form a bound state. The energy difference of the hole and electron tends to be just slightly lower than that of the energy band gap. Any of the π -conjugated molecules discussed in this thesis have HOMO and LUMO orbitals which strongly overlap each other (see figure 1.4), and so the probability of excitons forming in these molecules is high, and if an exciton forms there will be competition between exciton recombination or separation into charge carriers for charge transport. When an exciton recombines, fluorescence will be observed.

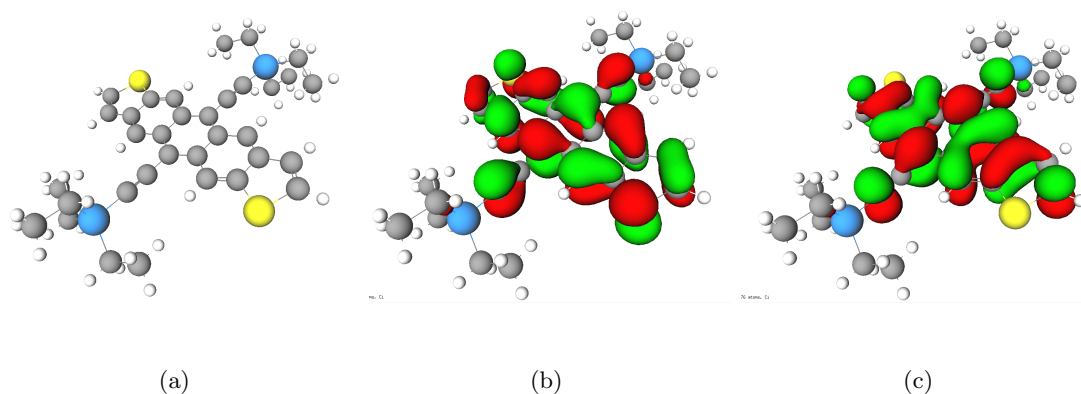


FIGURE 1.4: (a)Molecular structure of ADT-TES-F. The molecular orbitals of the HOMO (b) and LUMO (c) levels of ADT-TES-F are concentrated on the ADT backbone. The molecular orbital diagrams are the results of NWChem calculations and generated by ECCE. [21]

An excimer is an excited dimer, and example of the bimolecular excitons mentioned earlier. In the case where two different molecules are involved, the excimer is called an exiplex. Formation of exiplexes are one way to quench fluorescence in a crystal or thin film by physically separating the electron and hole upon excitation, and hindering the formation of an unimolecular exciton. As I mentioned in the previous section (section 1), defects in the crystal such as slightly different molecules forming electron traps can hinder

charge transport within a crystal, but in certain cases doping a crystal with a different molecule aids in the tuning of charge transport properties. A type-II bulk heterojunction is a heterojunction between two molecules where the HOMO and LUMO levels of one molecule (acceptor) are offset slightly below the levels of the other (donor), see figure 1.5.

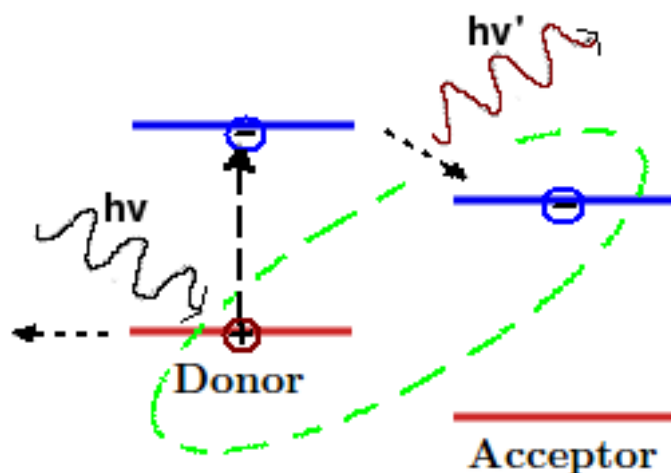


FIGURE 1.5: Schematic diagram of a type II heterojunction.

When an acceptor molecule in such a junction is photo-excited or an exciton comes into this junction, it is energetically favorable for the electron to travel from the LUMO level on the electron donor molecule to the LUMO level on the acceptor molecule, thus separating the exciton or the electron from the hole on the acceptor molecule. If a film is doped with a strong electron acceptor, photo-excited electrons are trapped on the dopant molecules leaving holes free to travel through the material, thus assisting charge transport. However, when a material is doped with weaker electron acceptors, a photo-excited electron that has moved to the acceptor and the hole on the donor can form a bound state, an exciplex. When an exciplex is formed, charge generation for charge transport is delayed, and a transient photocurrent has a longer lifetime. Changing the concentration of the donor within a film of acceptor molecules allows tuning of the material. Materials in which exciplex formation occurs have potential applications where slower charge generation

and recombination is required such as in photodetectors and image storage devices where effective storage of photo-generated charge carriers is required.[22]

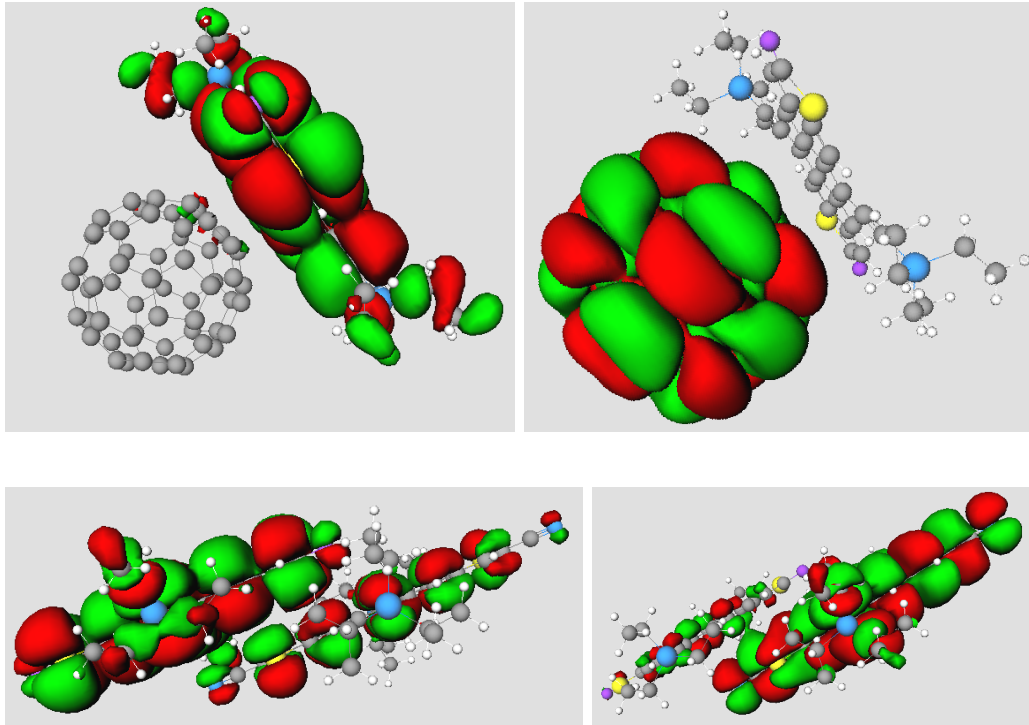


FIGURE 1.6: HOMO and LUMO orbitals of two-molecule type II bulk heterojunctions. The HOMO and LUMO orbitals for the combination of ADT-TES-F with C_{60} ((a) and (b) respectively), and with ADT-TIPS-CN ((c) and (d) respectively) are shown. The minimum spacing between all the molecules is the same. An excimer is more likely to form if there is overlap between the HOMO and LUMO orbitals. The molecular orbitals are calculated using the application of density functional theory in NWChem [23], and the isosurface images have been generated in ECCE [21].

The C_{60} buckyball is a well-known, strong electron acceptor, however it has the disadvantage that its structure is completely different from that of a π -conjugated molecule such as ADT-TES-F. It has already been established, see section 1, that charge transport is strongly dependent of the crystal structure, thus an electron acceptor molecule with similar structure would be far less detrimental to the intrinsic charge transport properties of a π -conjugated crystal. ADT-TIPS-CN form a type-II heterojunction with ADT-TES-

F, and it has a very similar structure to ADT-TES-F, thus it is a good candidate to use to tune the transport properties of ADT-TES-F,[22] however the HOMO and LUMO levels are not as far offset with respect to those of ADT-TES-F than C_{60} . Also, the two molecule combination of C_{60} and ADT-TES-F has a LUMO orbital which is entirely on the the C_{60} molecule and the HOMO orbital is entirely on the ADT-TES-F molecule. By contrast, the HOMO and LUMO levels of the two molecule combination of ADT-TES-F and ADT-TES-CN are both spread over the two molecules and overlap, and thus the electron and hole are more likely to form a bound state (exciplex) since their orbitals are not physically separated. Figure 1.6 compares HOMO and LUMO orbitals of two molecule combinations of ADT-TES-F and C_{60} , and ADT-TES-F and ADT-TIPS-CN.

2 Covalent Mechanochemistry: breaking covalent bonds

Not only do organic molecules have potential application in devices such as solar cells or eld effect transistors, where charge transport and transfer across intra- and intermolecular bonds is essential, but also in molecular force sensors or mechanocatalysts where the covalent bond properties within a molecule are exploited.

Molecular force sensors are useful in the study of biological systems. Mechanically reversible force sensors that do not adversely affect the biological environment would have many application in study of biological systems.[24, 25, 26]

In mechanocatalysts, mechanical force is used to break bonds in the molecule to activate the catalyst. This has advantages over chemical or photo activation, where the solution in which the catalyst resides might be altered by the addition of a new chemical or photons. However, specific bonds need to be broken to activate a mechanocatalyst. More information about the covalent bonds within a molecule, their bond strengths, and the probability of bond rupture becomes essential in order to design such devices. The

strength of intramolecular covalent bonds can also be investigated with ab-initio calculations. Bond strengths and activation energies can be approximated from adiabatic, isotensional stretching of a molecule in a stepwise fashion. Information is extracted from the potential energy surface along the reaction coordinate. The focus in this thesis will be on a mechanocatalyst containing a N-heterocyclic carbene, $C_{18}H_{25}N_3OS$. This molecule is a section of a much larger molecule that has been used in atomic force microscopy experiments. A specific C-C within $C_{18}H_{25}N_3OS$ has to break so that the N-heterocyclic carbene might be activated. The purpose of my theoretical calculations is to get a better idea of what the probability is for this bond to break compared to other bonds in the molecule when the molecule is mechanically stretched.

2.1 Experimental Methods

The two main methods for investigating covalent bonds in molecules are atomic force microscopy (AFM) experiments and ultrasound (sonication) experiments. The breaking strength of molecules has been tested by attaching an AFM tip to one end of a molecule with the other end adhered to a surface, and pulling at a constant force load rate (force-probe AFM). A different approach using AFM applies a constant force (force-clamp AFM) by controlling the force using a feedback system, this method would correspond to the theoretical isotensional density functional theory approach.[9]

Sonication experiments attach the molecule of interest between two long polymer chains. The stretching forces that occur when cavitation bubbles, created when the solution is exposed to ultrasound waves, collapse cause the bonds in the molecule to break.[9] Ultrasound-induced reaction occur on much smaller time scales than those of the AFM experiments, however the forces that occur on the molecule are not directly accessible, and there are also local heating effects due to the ultrasound that have to be considered.[26]

2.2 Theoretical methods and history

Generally, molecular dynamics calculations are useful to theoretically examine chemical reactions, however the calculations can be demanding on computational resources and are not feasible for reactions that occur on large time scales. The use of mechanical force can speed up a reaction

2 ELECTRONIC STRUCTURE OF ANTHRADITHIOPHENE DERIVATIVES

1 Introduction

Organic π -conjugated materials, such as functionalized pentacene and anthradithiophene, have been shown to have promising electronic properties such as high photoconductivity, and good charge carrier mobilities greater than $1 \text{ cm}^2/\text{Vs}$ [27] and high on/off ratios in organic field effect transistors,[6, 28] making them good candidate materials for use in organic electronic devices such as solar cells, photodetectors, and field effect transistors.[6] While these electronic properties may not be as good as those of inorganic semiconductors such as Si, this group of materials has the advantage of flexibility, solution-processability, and low production costs.

Typically, charge carriers in organic semiconductors are electrons or holes associated with π -orbitals. Unlike well-known inorganic semiconductors such as Si or CdTe, which are held together by covalent bonds and have delocalized orbitals, the individual molecules in organic crystals are held together by van der Waals interactions and have orbitals localized on each molecule. Consequently, charge transport mediated by phonons is one of the main mechanisms for charge transport in organic semiconductors, making charge mobility strongly temperature-dependent. However charge mobility results for pentacene have been recorded, that are independent of temperature for temperatures below 120 K.[29] This result suggests that there is sufficient molecular orbital overlap between individual molecules in the crystal that band-like conduction is possible.[6] Hence, the degree of intermolecular overlap of the π -orbitals is a critical factor for charge mobility, and has a strong relationship with crystal morphology. Anthradithiophene (ADT) is a π -conjugated organic material that crystallizes in a herringbone structure. [10, 3] The herringbone structure results in poor overlap of the π -orbitals between the molecules and correspondingly low

mobility. The addition of large side-groups to ADT induces a change in morphology from herringbone to planar packing,[10, 30] which leads to improved overlap of the π -orbitals between the molecules and higher mobility compared to ADT in a herringbone structure. When compared to much studied pentacene,[3, 28] the presence of sulfur in the thiophene rings makes ADT more susceptible to end-group functionalization than pentacene. These end groups add stability to the structure, [30] and also change the electrochemical properties of the molecule.

In this chapter, we will look at the electronic properties of the anthradithiophene derivatives that have fluorine or cyano (CN) end-groups functionalized with either triisopropylsilylethynyl (TIPS) or triethylsilylethynyl (TES) sidegroups, see figure 2.1. Not only have large charge mobilities $> 1.5\text{cm}^2/(\text{Vs})$ been measured for these materials, but they also have high photoconductivity and a strong photoluminescence in solution-deposited films.[30] The end groups change the electronegativity of the molecules, shifting the HOMO and LUMO levels, allowing the creation of donor-acceptor of pairs such as ADT-TES-F (donor) and ADT-TIPS-CN (acceptor) to form Förster resonant energy transfer complexes. These exiplexes result in a slower charge carrier recombination with possible application in situations where effective storage of photogenerated charge carriers is required. [22] This paper analyzes the highest occupied molecular orbital (HOMO) and lowest unoccupied molecular orbital (LUMO) energy levels to predict which molecular pairs would promote good electron transfer. Theoretical analysis of the effective masses of the single crystals for each molecule indicate at most two-dimensional electron/hole transfer. The effective masses, and consequently the contribution to carrier mobility by band-like transport, are strongly dependent on the molecular packing. The calculated effective mass tensor indicates a strong intermolecular carrier mobility across the π -stacked planes, as well as intramolecular charge transport across the ADT backbones of the molecule.

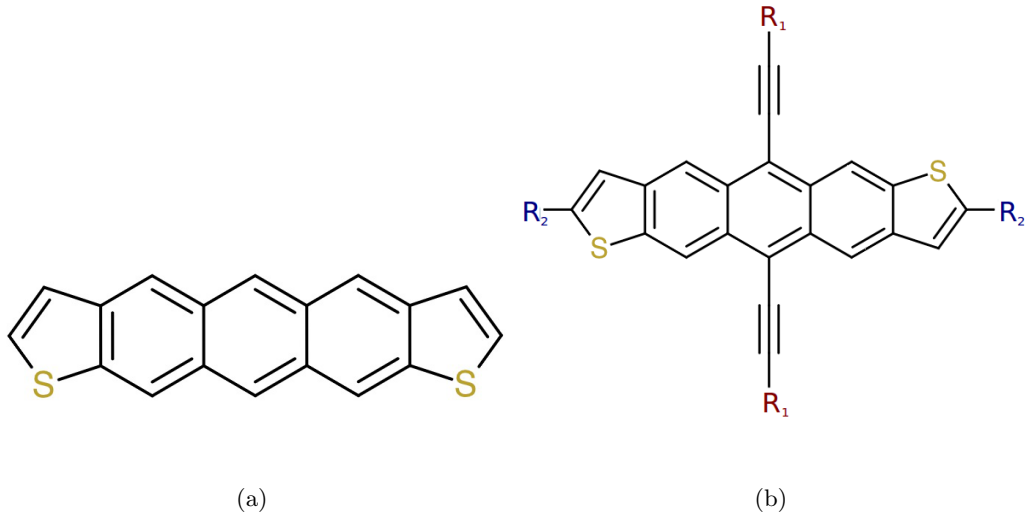


FIGURE 2.1: Molecular structures of (a) the *sys*-isomer of ADT, and (b) the *anti*-isomer of functionalized ADT. R_1 =Si-*i*-Pr₃ (triisopropylsilyl), Si(CH₂CH₃)₃ (triethylsilyl) or (CH₃CH₂C(CH₃))₃Si (tri-*sec*-butylsilyl), and R_2 =H, F, or CN. Diagrams of these side groups are illustrated in figure 2.2.

2 Theoretical Methods

The theoretical results presented in this paper are derived from *ab-initio* calculations performed in VASP and NWChem.

For the electronic and optical properties of the molecular crystals, the projector-augmented wave method [31, 32] implemented in VASP [33, 34, 35, 36] within the generalized gradient approximation with the PW91 exchange functional [37, 38] was used. Apart from the ADT and ADT-TES-CN structures, the crystal structures used for *ab-initio* calculations of these organic crystals were those experimentally determined by John Anthony’s group [39, 28]. Since the experimentally determined crystal structures are not available for ADT and ADT-TES-CN, these structures were calculated using the energy minimization methods available in VASP. Relaxation of the ions and unit cells in VASP using a conjugate-gradient algorithm, the generalized gradient approximation in DFT,

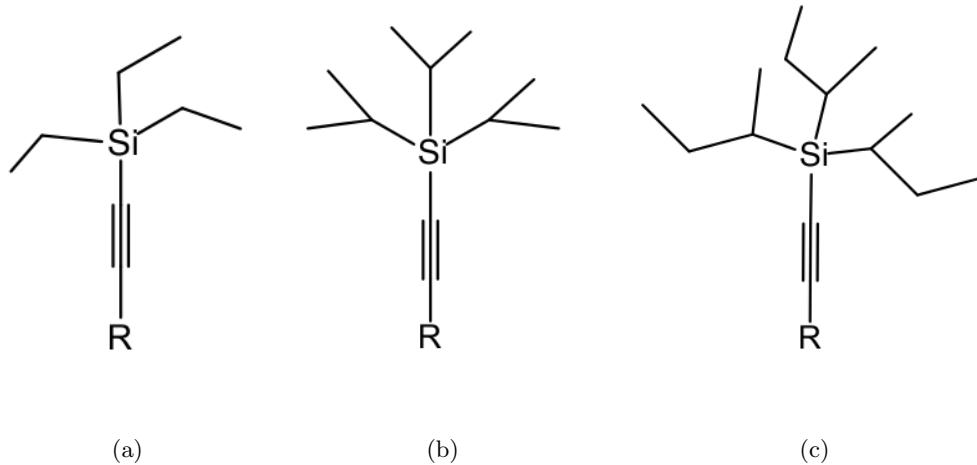


FIGURE 2.2: Diagrams of the side groups considered for these ADT derivatives: (a) triethylsilylethynyl (TES), $-\text{CSi}(\text{CH}_2\text{CH}_3)_3$, (b) triisopropylsilylethynyl (TIPS), $-\text{CSi-}i\text{-Pr}_3$, and (c) trisec-butylsilylethynyl (TSBS), $-\text{CSi}(\text{C}(\text{CH}_3)_2\text{CH}_2\text{CH}_3)_3$.

and a van der Waals energy correction yielded the distances and angles quoted in tables 2.4 and 2.5 for these two molecular structures. The approximation for the van der Waals correction to the free energy followed the DFT-D2 method of Grimme.[40] The Perdew-Burke-Ernzerhof exchange functional was used in the geometry optimization. In order to get the lowest energy structure, the ADT crystal was assumed to have a herringbone structure with two molecules per unit cell, and ADT-TES-CN was assumed to be similar to the ADT-TES-F structure with the starting structure the same as the experimental crystal structure of ADT-TES-F but with the fluorine molecules substituted with cyano (CN) groups. For all of the crystal structures, the real-space lattice vectors have been redefined so that vectors **a** and **b** define the plane of ADT backbones, and **c** describes the vector crossing the planes, while still preserving the original crystal structure. Within the plane, **a** is the vector with the largest component along the ADT backbone, see figure 2.3.

A cutoff energy of 900 eV was used, with Monkhorst-Pack grids in reciprocal space chosen as follows: 6x3x8 for ADT-TES, 5x2x4 for ADT-TES-F, 2x3x6 for ADT-TIPS,

3x3x5 for ADT-TIPS-F, and 3x2x1 for ADT-TIPS-CN. The isomers of anthradithiophene and its derivatives are isoenergetic and only the results for the anti-isomers are quoted. All density of states plots had Fermi smearing applied with $\sigma=0.05$ eV.

Calculation of the effective mass requires the second derivative of the band energy with respect to Cartesian coordinates in reciprocal space, see equation 2.4. The valence (conduction) band energy is assumed to be three dimensional parabolic function in reciprocal space near the extremum point. In order to calculate this function, the band energies for a three dimensional grid in reciprocal space about the extremum point were calculated. Each calculation used the charge density file (CHGCAR) from the original DFT calculation for each molecular crystal. Due to the existence of local maxima and minima for the valence and conduction bands, the grid points used to calculate the parabolic functions for the absolute extrema have to be limited in range. Small energy ranges (dE) on the order of room temperature thermal energy and maximum distances (dk) from the extremum point in reciprocal space determined which grid points were used in the linear least-squares fit to determine the energy function. dE and dk values were chosen so that there was a good correspondence between the position and value of the extremum points of the fitted and DFT data, as well as a small root-mean-square value (of order 10^{-4} eV) for the deviation of the fitted function from the band energies of the relevant data points. Each effective mass tensor is diagonalized to calculate its eigenvalues and eigenvectors. In some cases, due to the low dispersion of the transport band in a particular direction in k-space, an effective mass eigenvalue is strongly dependent on the choice of energy range around the extremum for the parabolic fit. In these cases a minimum value for the effective mass eigenvalue is quoted.

The geometry for each isolated, neutral molecule was optimized using the Gaussian basis set approach to density functional theory as implemented in NWChem [23] using the B3LYP hybrid functional [41] and the 6-31G basis set [42] in conjunction with the

energy minimization algorithms built into NWChem. The relaxed and vertical energies of singly charged molecules were calculated in the same manner. The optimized geometries for the neutral molecules were also used to calculate values for the HOMO-LUMO gaps within the generalized gradient approximation with the PW91 functional as implemented in VASP and analyzed at the Γ -point with Fermi-smearing of width $\sigma=0.026$ eV. In order to simulate an isolated molecule, the molecules were separated by a minimum of 12 Å on all sides.

3 Results and Discussion

3.1 Molecular properties

Ionization potential, Electron Affinity and HOMO-LUMO gap

The anthradithiophene (ADT) derivatives considered in this report are those that have hydrogen, fluorine or cyano (CN) end-groups, and are functionalized with either triisopropylsilylethynyl (TIPS), triethylsilylethynyl (TES), or tri*sec*-butylsilylethynyl (TSBS) side groups attached to the center carbon ring, see figures 2.1 and 2.4(a). The end groups on the terminal thiophene rings affect the electronegativity of the molecules. Figure 2.5 is diagram of the calculated relative alignment of the highest occupied molecular orbital (HOMO) and lowest unoccupied molecular orbital (LUMO) levels for these molecules. DFT calculations using the B3LYP hybrid functional for the molecules with the fluorine or cyano end groups yield relatively good values for the HOMO and LUMO levels compared to experimental pulse voltammetry measurements. [43]

In a type II heterojunction, where the HOMO level of one molecule is higher (donor) than that of the other molecule (acceptor), and similarly for the LUMO levels, it is energetically favorable for an electron photoexcited in the donor molecule to fall into the first excited state of the acceptor molecule, leaving the hole on the donor free to travel through the rest of the material before the electron and hole can form an exciton and

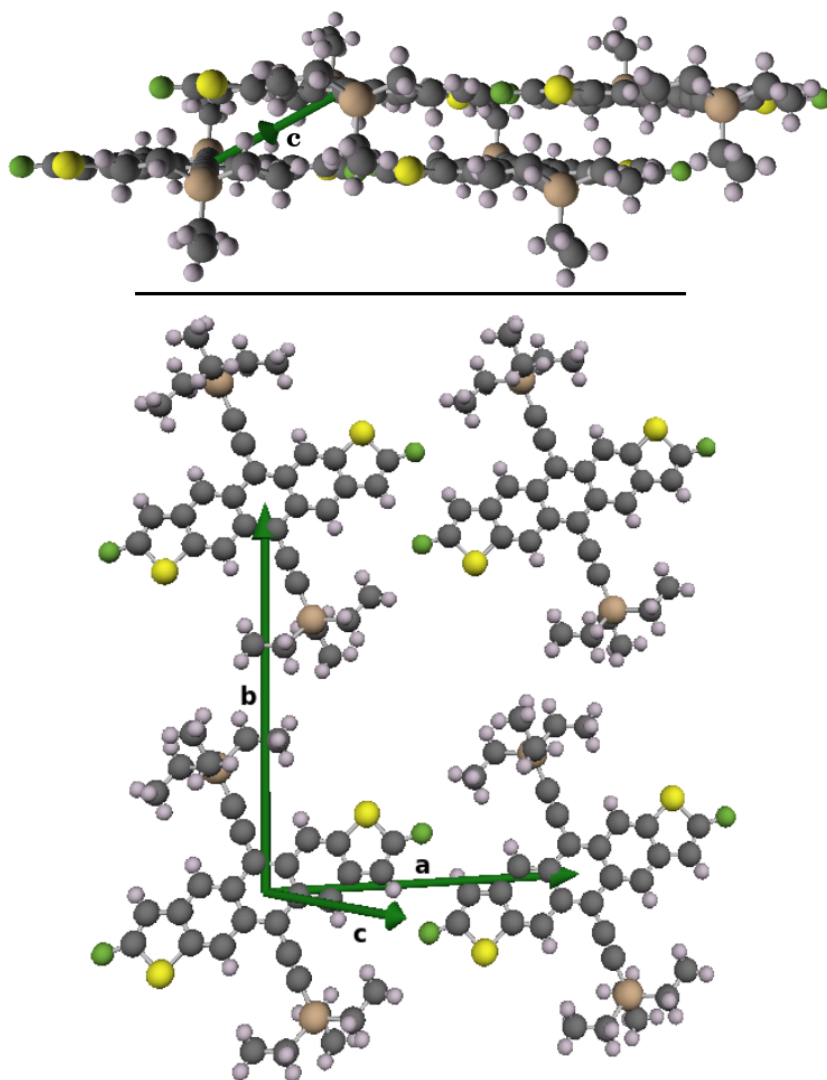


FIGURE 2.3: Crystal structure of ADT-TES-F. The **a** and **b** vectors define the plane of anthradithiophene backbones, while **c** links these planes. The anthradithiophene derivatives discussed in this chapter that have TIPS and TES side groups have similar structures.

recombine. The molecules form a bulk heterojunction across which charge transport is promoted once the system has been excited. One of the factors affecting the flow of electrons and holes across this heterojunction is the relative levels of the HOMO and LUMO levels of the two molecules. Figure 2.5 clearly indicates ADT-TES-F and ADT-TIPS-CN are two such pairs. This agrees with experiment, where adding different concentrations of

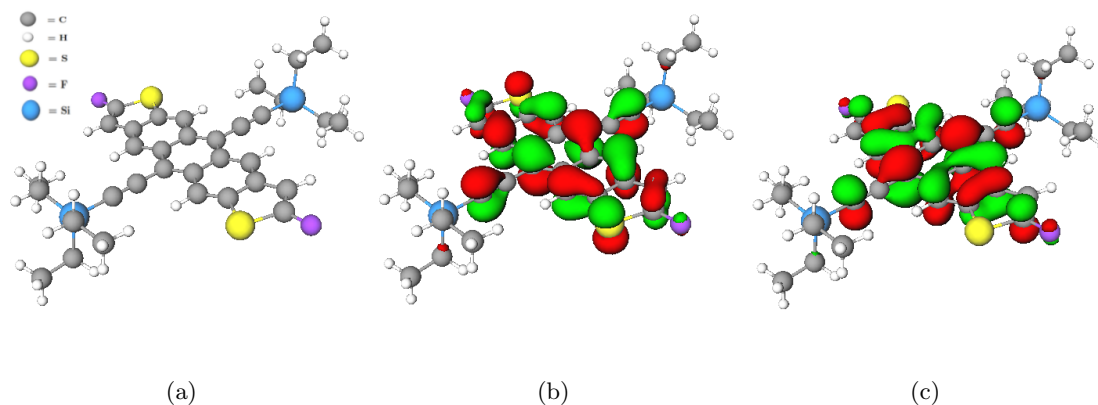


FIGURE 2.4: (a)Molecular structure of ADT-TES-F. The molecular orbitals of the HOMO (b) and LUMO (c) levels of ADT-TES-F are concentrated on the ADT backbone. The molecular orbital diagrams are the results of NWChem calculations and generated by ECCE. [21]

ADT-TIPS-CN (acceptor) to pristine ADT-TES-F (donor) altered transient photocurrent and photoluminescence readings, making it possible to tune photoluminescent properties of these derivatives .[22] The advantage of using donor-acceptor pairs with similar crystal structure is that the overall crystal structure is not changed significantly, and hence good transport properties conserved.

Figure 2.5 is a diagram of the calculated relative alignment of the HOMO and LUMO levels for these molecules. Clearly, the fluorine and cyano endgroups lower the electronegativity of the molecules.

Table 2.1 contains experimental and theoretical values for the band gaps of these materials. The theoretical values calculated in GGA were for isolated molecules, and are underestimated if we compare them to experimental electrochemical results for molecules in solution. The B3LYP functional, calculated using NWChem, produces values that are closer to experiment than the GGA results, calculated using VASP, and show a similar trend in the molecules displayed in the experimental values.

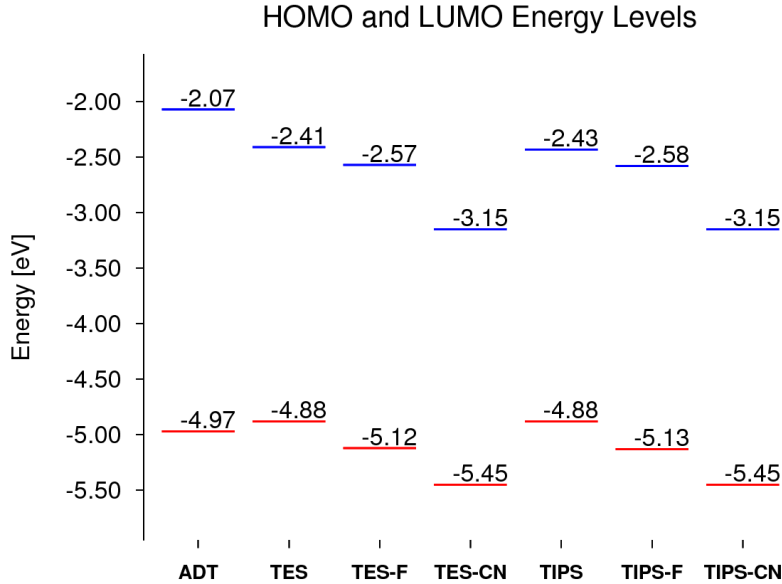


FIGURE 2.5: Diagram comparing the HOMO and LUMO levels of ADT-derivatives.

Reorganization energies

Hopping transport within a single crystal can be described as an electron/hole transfer reaction in which the charge on a singly-charged molecule is transferred to a neutral molecule as in equation 2.1 where A, B are two identical molecules such as ADT-TES.



From this perspective, we can apply Marcus theory [17, 16] to get an expression for the rate constant, k_T of this transfer reaction, see equation 2.2. In this equation, k_B is Boltzmann's constant, T is the temperature and A is a prefactor related to the electron coupling between two adjacent molecules. λ is the reorganization energy which, if one ignores the intermolecular contributions such as polarization of the surrounding medium and molecular vibrations, can be attributed to the change in geometry when a molecule changes from a neutral to singly-charged state and *visa versa*. The intramolecular reorganization energy for a hole(electron) $\lambda_{h(e)}$ is the sum of the relaxation energy of a

TABLE 2.1: Table of chemical formulas, and experimental and calculated HOMO-LUMO gaps (in eV) for isolated molecules of the ADT derivatives.

molecule	Formula	Expt	B3LYP	GGA
ADT	$C_{18}H_{10}S_2$	-	2.90	1.55
ADT-TES	$C_{34}H_{38}S_2Si_2$	2.51	1.19	0.81
ADT-TES-F	$C_{34}H_{36}F_2S_2Si_2$	2.30	2.55	1.47
ADT-TES-CN	$C_{36}H_{36}S_2Si_2N_2$	-	2.30	1.23
ADT-TIPS	$C_{40}H_{50}S_2Si_2$	2.50	1.34	1.19
ADT-TIPS-F	$C_{40}H_{48}F_2S_2Si_2$	2.30	2.59	1.42
ADT-TIPS-CN	$C_{42}H_{48}S_2Si_2N_2$	2.06	2.35	1.25
ADT-TSBS-F	$C_{46}H_{60}F_2S_2Si_2$	-	2.54	

cationic(anionic) molecule from the neutral geometry to the ionic geometry ($\lambda_{h(e)}^{+(-)} = E_0^{+(-)} - E_{+(-)}^{+(-)}$) and the relaxation energy of the neutral molecule from cationic(anionic) to neutral geometry ($\lambda_{h(e)}^0 = E_{+(-)}^0 - E_0^0$).[44]

$$k_T = A \exp \left[\frac{-\lambda}{4k_B T} \right] \quad (2.2)$$

The hole reorganization energies for the ADT derivatives range from 150% to 180% of that for ADT, and 110% to 150 % for the electron reorganization energies, and for ADT and all it derivatives considered here the electron reorganization energy is always higher than the hole reorganization energy. This result corresponds well with the fact the the materials have are *p*-type in nature. Addition of the fluorine end-groups corresponds with higher reorganization energies, while cyano end groups do not seem to have much effect on the reorganization energy. Interestingly, ADT-TIPS-CN has the lowest reorganization energies, while ADT-TES-F has the highest.

TABLE 2.2: Vertical and adiabatic ionization potentials and electron affinities for the ADT-derivatives (in eV) for isolated molecules. Here we define $IP = E(M^+) - E(M)$ and $EA = E(M^-) - E(M)$. The final column, $IP+EA_{adiabatic}$ is the sum of the adiabatic ionization potential and electron affinity for each molecule. Ideally, in a calculation with no approximations, this would equal the HOMO-LUMO gap of the molecule.

	IP		EA		IP+EA _{adiabatic}
	vertical	adiabatic	vertical	adiabatic	
ADT	6.34	6.30	-0.68	-0.76	5.54
ADT-TES	6.03	5.96	-1.25	-1.36	4.44
ADT-TES-F	6.27	6.19	-1.41	-1.52	4.67
ADT-TES-CN	6.55	6.47	-2.06	-2.15	4.32
ADT-TIPS	6.02	5.95	-1.29	-1.39	4.56
ADT-TIPS-F	6.25	6.17	-1.44	-1.56	4.61
ADT-TIPS-CN	6.52	6.45	-2.08	-2.17	4.28
ADT-TSBS-F					

3.2 Crystal properties

Geometries, band structures, and density of states

Electronic coupling between adjacent molecules and reorganization energy λ are two major parameters for charge mobility. A strong molecular orbital overlap, which is strongly dependent on crystal morphology, and a low reorganization energy are necessary for efficient charge transfer between molecules. The herringbone arrangement of molecules in single crystal ADT [3], does not allow for a good overlap of molecular orbitals. The addition of large side groups to the ADT backbone induces planar structures, with the ADT backbones parallel to the *ab* planes. [39, 28] The lattice parameters for the crystal

TABLE 2.3: Intramolecular reorganization energies (meV) for holes λ_h and electrons λ_e of isolated ADT derivative molecules.

	λ_h^+	λ_h^0	λ_h	λ_e^-	λ_e^0	λ_e
ADT	46	46	92	82	80	162
ADT-TES	70	72	143	111	112	224
ADT-TES-F	81	83	164	117	118	235
ADT-TES-CN	75	68	144	96	89	185
ADT-TIPS	69	70	139	108	112	220
ADT-TIPS-F	79	80	160	119	113	233
ADT-TIPS-CN	68	70	138	90	88	178
ADT-TSBS-F						

structures of the anthradithiophene derivatives discussed in this chapter, all of which can be described as triclinic structures, are listed in table 2.4. In table 2.5, we can see that all the molecules with TIPS and TES sides groups have backbones which are parallel to the molecular planes (within a few degrees). While both side groups, TIPS and TES, induce a planar crystal geometry, the smaller TES side group allows closer packing of the molecules.^a The closer packing corresponds to higher molecular orbital overlap of the HOMO and LUMO orbitals, critical for good carrier transport. The fluorine and cyano end groups also appear to bring the molecules closer together within the planes, allowing more HOMO-LUMO orbital overlap, and the cyano end groups in particular seem to cause the distance between the planes to decrease.

^aThe crystal structures for ADT and ADT-TES-CN these molecules were theoretically determined using VASP (see section 2 for details)

π -conjugated molecules such as these ADT derivatives have their HOMO and LUMO molecular orbitals concentrated mainly on the ADT backbone, see figure 2.4, so a planar stacking would improve π -orbital overlap, provided that planes are not too far apart. Charge carriers that are less localized on the molecule will have higher molecular orbital overlap and wider conducting bands. This is reflected in the data in table 2.6

The electronic band structures and density of states of the ADT derivatives are shown in figures 2.7 and 2.8. The bands around the HOMO-LUMO gap are less disperse for molecules functionalized with TIPS, which implies that there is less intermolecular overlap of the HOMO or LUMO molecular orbitals as expected due to the fact that TIPS is a larger side group. In general, the HOMO band is more disperse than the LUMO band, corresponding well with the *p*-type nature of these organic semiconductors. The band dispersion values for the HOMO and LUMO bands are recorded in table 2.6. The band dispersions of the crystals composed of molecules with the TES side group are greater than that of pure ADT. The opposite is true for the larger TIPS and TSBS side groups. It would seem that the TES side group is just large enough to induce planar geometries while not too large, like TIPS, to cause a planar separation that is not conducive to band-like charge transport.

Effective masses

With the induced planar packing, we expect higher degrees of band-like intermolecular charge transport where there is overlap of π -orbitals, namely across the planes of ADT (pentacene) backbones, as well as the expected intramolecular charge transport across the backbone of the molecule. This is reflected in the eigenvectors of the three-dimensional effective mass tensor.

Using the Drude model, mobility can be modeled with equation 2.3. In this model, effective mass is a temperature independent quantity, while the scattering time τ which is a temperature dependent quantity, the calculation of which would involve phonon cal-

TABLE 2.4: Lattice parameters for anthradithiophene derivative single crystals. The volume quoted is the volume per molecule.

molecule	a (Å)	b (Å)	c (Å)	α	β	γ	Volume (Å ³)
ADT ^a	16.00	18.61	5.729	156.67°	62.97°	117.32°	298.8
ADT-TES	13.67	17.23	6.732	100.20°	30.99°	91.41°	777.6
ADT-TES-F	13.89	17.24	7.115	98.57°	29.78°	89.99°	807.4
ADT-TES-CN ^a	15.42	19.85	6.788	102.27°	29.89°	91.00°	951.1
ADT-TIPS	27.78	19.76	8.786	63.60°	50.51°	106.72°	1882.4
ADT-TIPS-F	16.95	18.15	8.180	84.05°	26.22°	72.25°	968.6
ADT-TIPS-CN	23.85	17.03	8.672	86.94°	30.86°	62.48°	1051.25
ADT-TSBS-F	15.07	24.57	16.45	132.03°	90.00°	80.34°	1102.3

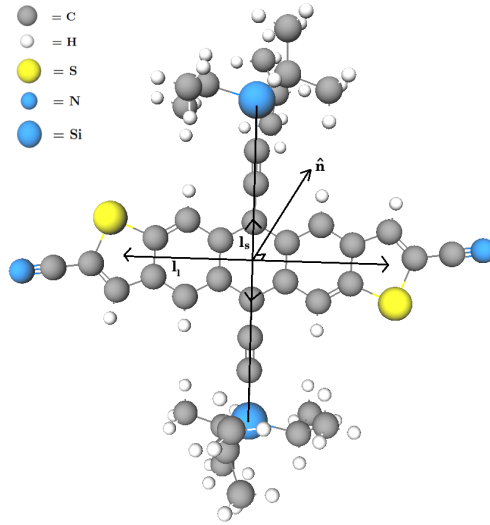


FIGURE 2.6: Molecular structure of ADT-TIPS-CN overlaid with diagrams of the ADT backbone long axis (\mathbf{l}_l), short axis (\mathbf{l}_s), and backbone normal ($\hat{\mathbf{n}}$). This picture was generated using Ecce [21].

culations as well as consideration of crystal defects. The Drude model is generally too simplistic for complex materials like organic semiconductors to get accurate mobility val-

TABLE 2.5: Orientation of molecules with respect to the lattice. Each column lists the angle between the two vectors indicated at the top of the column. $\hat{\mathbf{n}}$ represents the vector perpendicular to the ADT backbone of the molecules, and \mathbf{l}_s and \mathbf{l}_l represent the short and long axes of the ADT backbone. Figure 2.6 illustrates these vectors for ADT-TIPS-CN. The distance between lattice planes (\mathbf{c}_\perp) and angle of \mathbf{a} with respect to the \mathbf{ab} -plane normal are also listed for each crystal.

molecule	$\mathbf{a} \times \mathbf{b}$ and $\hat{\mathbf{n}}$	\mathbf{l}_l and \mathbf{a}	\mathbf{l}_s and \mathbf{b}	$\mathbf{a} \times \mathbf{b}$ and \mathbf{c}	\mathbf{c}_\perp (\AA)
ADT ^{bc}	3.1°	17.2°	10.3°	66.8°	2.26
ADT-TES	3.7°	21.7°	21.0°	60.6°	3.30
ADT-TES-F	4.8°	20.4°	21.0°	59.1°	3.37
ADT-TES-CN ^a	7.4°	33.5°	20.1°	60.1°	3.11
ADT-TIPS	0.9°	3.8°	19.9°	66.5°	3.58
ADT-TIPS-F	5.2°	3.1°	18.4°	66.7°	3.31
ADT-TIPS-CN	4.8°	11.8°	18.9°	66.9°	2.92
ADT-TSBS-F ^d	7.2°	14.6°	27.9°	42.8°	

ues. In order to do so, transport mechanism such as hooping and tunneling should also be considered. However, the effective mass tensors do give a good indication as to which directions are favorable for charge transport.

$$\mu = \frac{e\tau(T)}{m_{\text{eff}}} \quad (2.3)$$

The inverse effective mass tensor can be calculated using equation 2.4 where subscripts i and j denote Cartesian coordinates in reciprocal space and $E(\mathbf{k})$ is the band energy as a function of the wave vector \mathbf{k} . [45] In table 2.7, the results of the calculations described in section 2, the eigenvectors of the diagonalized effective mass tensors are expressed in terms of units vectors in the direction of the real space lattices vectors. Their corresponding eigenvalues are expressed in units of electron rest mass.

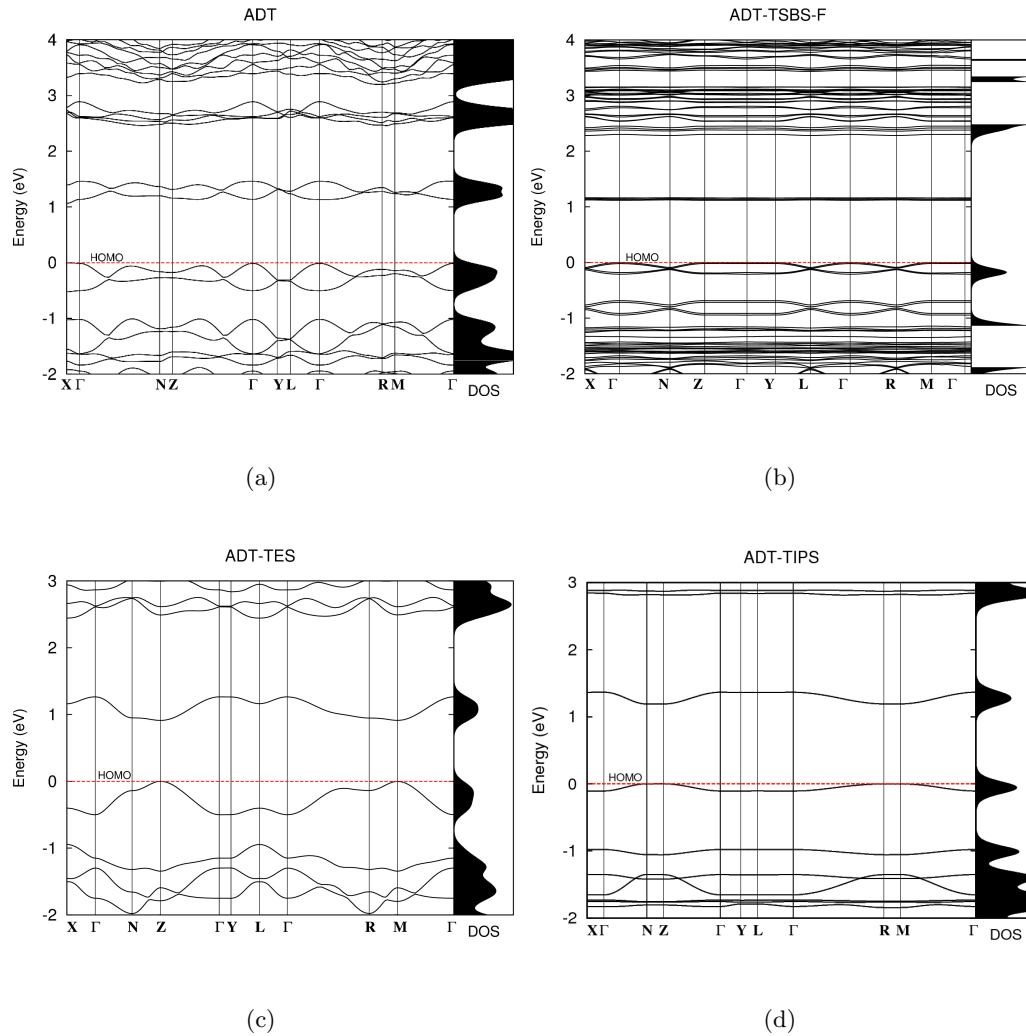


FIGURE 2.7: Band structures of single crystal anthradithiophene and derivatives ADT-TSBS-F, ADT-TES, and ADT-TIPS. The reciprocal coordinates of the high-symmetry points used in the band structures - Γ , X, N, Z, Y, L, R and M - are, expressed in terms of the reciprocal space lattice vectors, $(0,0,0)$, $(0.5,0,0)$, $(0.5,0,0.5)$, $(0,0,0.5)$, $(0,0.5,0)$, $(0.5,0.5,0)$, $(0.5,0.5,-0.5)$ and $(0.0,0.5,-0.5)$ respectively.

$$\left(\frac{1}{m^*}\right)_{ij} = \frac{1}{\hbar^2} \frac{\partial^2 E(\mathbf{k})}{\partial k_i \partial k_j} \quad (2.4)$$

In general, the ADT-derivatives considered here are expected to have two-dimensional band-like charge transport, namely the intermolecular charge transport across the planes

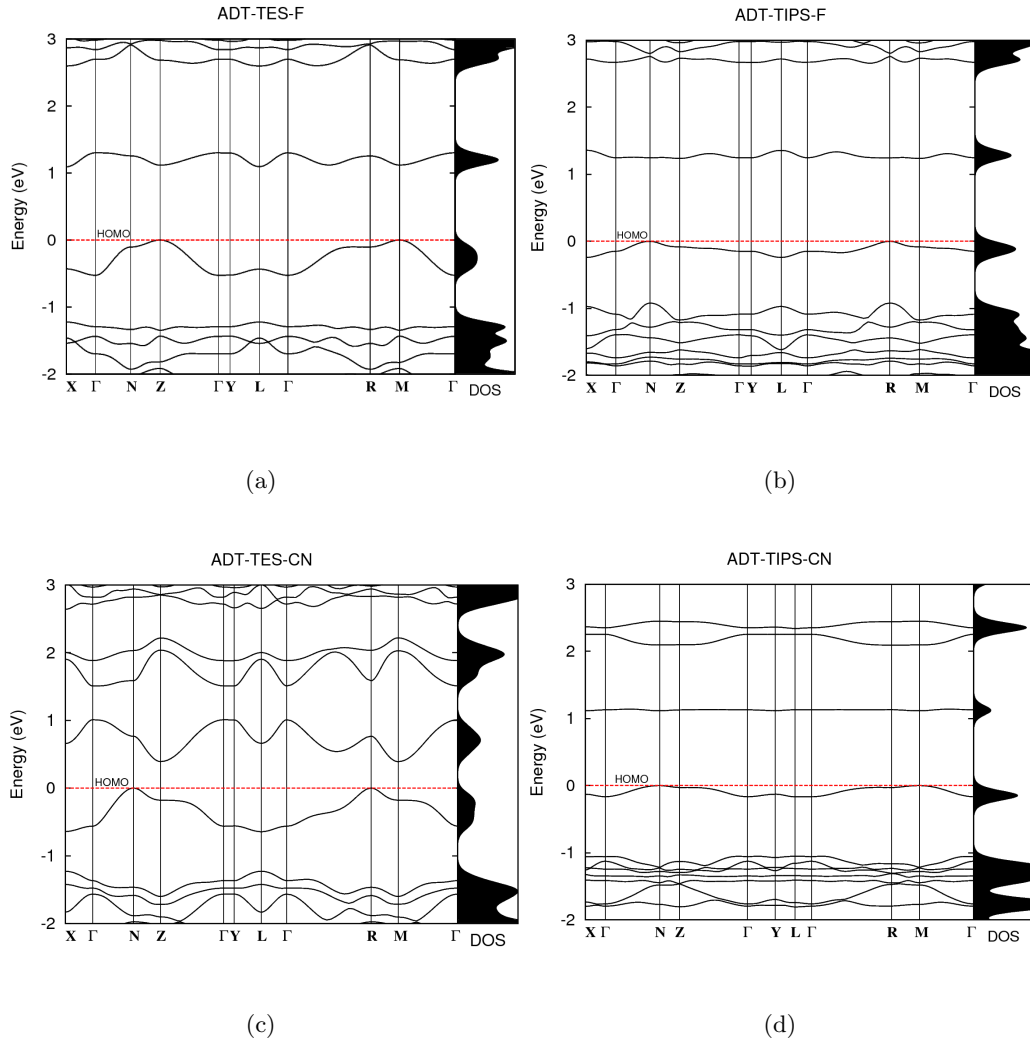


FIGURE 2.8: Band structures of single crystal anthradithiophene derivatives ADT-TES-F, ADT-TIPS-F, ADT-TES-CN and ADT-TIPS-CN. The reciprocal coordinates of the high-symmetry points used in the band structures - Γ , X, N, Z, Y, L, R and M - are, expressed in terms of the reciprocal space lattice vectors, $(0,0,0)$, $(0.5,0,0)$, $(0.5,0,0.5)$, $(0,0,0.5)$, $(0,0.5,0)$, $(0.5,0.5,0)$, $(0.5,0.5,-0.5)$ and $(0.0,0.5,-0.5)$ respectively.

of ADT backbones as well the intramolecular transport along each ADT backbone. Transport across the large side groups is unlikely, as expected, since the fraction of the HOMO and LUMO molecular orbitals in these regions of the molecule are negligible. This is demonstrated by the insignificant or zero contribution of the \mathbf{b} lattice vector for eigen-

TABLE 2.6: HOMO-LUMO gaps and band dispersions of the HOMO and LUMO bands for single crystal ADT derivatives (in eV), calculated using GGA in PW91.

	Band Dispersions (eV)		
	HL gap	HOMO	LUMO
ADT	1.06	0.31	0.24
ADT-TES	0.81	0.43	0.37
ADT-TES-F	1.09	0.53	0.21
ADT-TES-CN	0.39	0.64	0.61
ADT-TIPS	1.19	0.11	0.18
ADT-TIPS-F	1.26	0.24	0.12
ADT-TIPS-CN	1.11	0.18	0.03
ADT-TSBS-F	1.15	0.009	0.001

vectors corresponding to the smaller effective mass eigenvalues recorded in table 2.7 and illustrated for ADT-TES-F in figures 2.9 and 2.10.

One can observe a trend in the effective masses in table 2.7. The lowest effective mass for each molecule decreases mostly with fluorination and less significantly with addition of cyano end groups. These values correspond to the eigenvector that has the largest component across the planes. One can also note that, in real space, the eigenvectors corresponding to the highest effective mass eigenvalue mostly lie in the direction of the \mathbf{b} lattice vector, see figures 2.9 and 2.10. This is the direction in which we expect the lowest charge mobility and since the \mathbf{b} is an in-plane vector which cuts through the side groups of these ADT derivatives. Functionalization with TIPS gives rise to higher effective masses compared to functionalization with TES, and a comparison of the magnitudes of the other effective mass eigenvalues of those molecules with TIPS side groups indicates that TIPS-

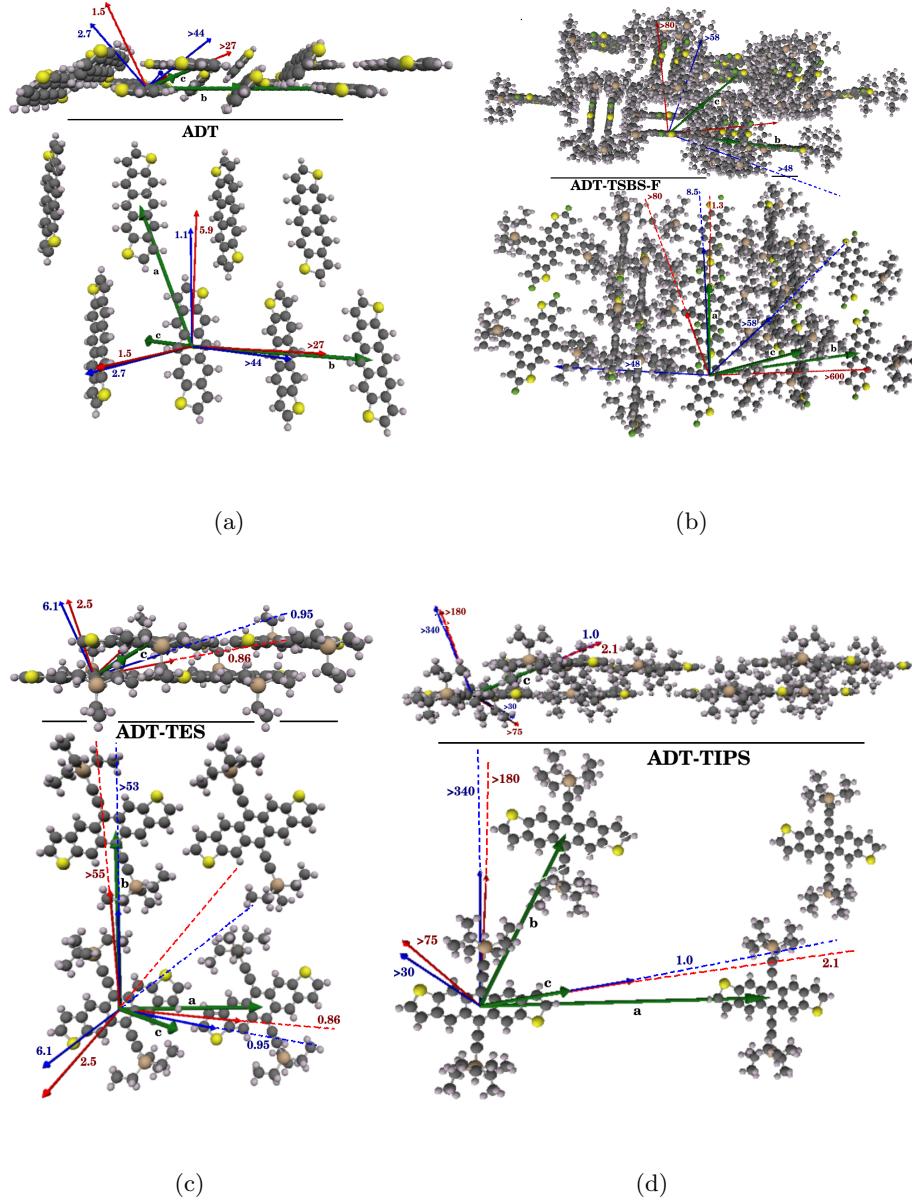


FIGURE 2.9: Crystal structure and effective mass eigenvectors of ADT-based molecules. ADT, ADT-TSBS-F, ADT-TES and ADT-TIPS crystal structures are overlaid with their lattice vectors (green) and calculated effective mass eigenvectors for both holes (red) and electrons (blue). The label on each eigenvectors is the corresponding eigenvalue, the effective mass for that direction in units of electron mass. For each crystal structure, perspectives of a slice through the planes (upper) and of a single plane (the **ab** planes) (lower) are shown.

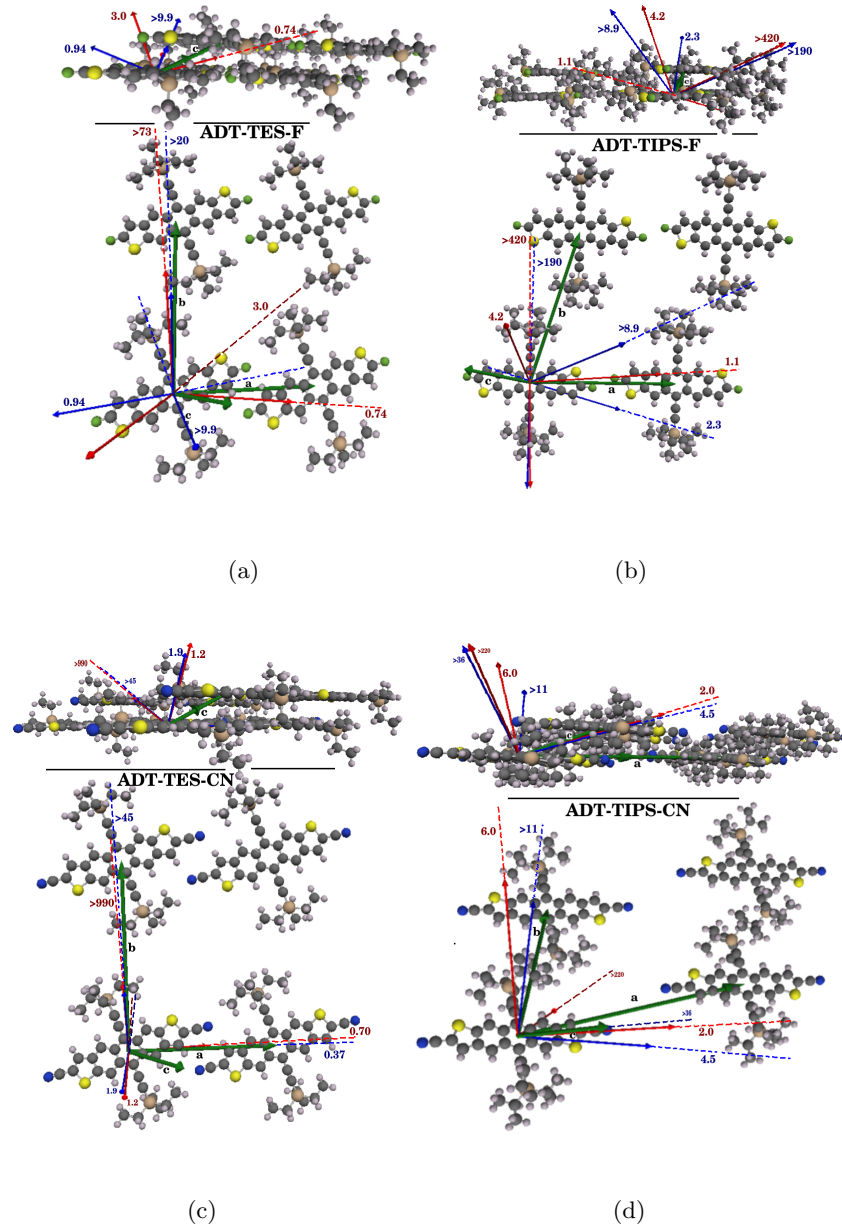


FIGURE 2.10: Crystal structure and effective mass eigenvectors of ADT-based molecules *continued*. ADT-TES-F, ADT-TIPS-F, ADT-TES-CN and ADT-TIPS-CN crystal structures are overlaid with their lattice vectors (green) and calculated effective mass eigenvectors for both holes (red) and electrons (blue). The label on each eigenvector is the corresponding eigenvalue, the effective mass for that direction in units of electron mass. For each crystal structure, perspectives of a slice through the planes (upper) and of a single plane (the **ab** planes) (lower) are shown.

functionalized molecules tend toward a one-dimensional charge carrier transport. This is likely due to the fact that the larger side group on the ADT-TIPS derivatives requires more spacing in the ab planes. This might shed some light on the considerably smaller hole mobility of vapor-deposited films of ADT-TIPS compared to that of ADT-TES. The hole mobility of ADT-TIPS films was experimentally recorded as less than 10^{-4} cm^2/Vs , while that of ADT-TES was 1.0 cm^2/Vs . However, this possibly has more to do with the fact that the ADT-TIPS films tended to be amorphous while the ADT-TES films were more uniform.[28] Molecules with more bulky side groups have been associated with lower crystallinity [46], which can be explained by the fact that looser packing corresponds with lower intermolecular bonding.

Out of all the ADT derivatives considered, the low effective masses calculated for ADT-TES-F identify it as the most promising candidate with respect to band transport. The relatively close packing of the molecules in ADT-TES-F also promotes better hopping transport.

4 Summary and Conclusions

We have reported theoretical single molecule results for band gap, ionization potentials and electron affinities. While the addition of side groups TES and TIPS to anthradithiophene clearly changes the crystal structure to one in which more overlap of the HOMO and LUMO orbitals is possible, this does not seem to have much effect on the single molecule results. However, functionalization of the end thiophene rings of the ADT backbone with fluorine and cyano, clearly changes the electronegativity of the molecules, a conclusion that agrees well with experimental measurements.

The band structure and effective mass reported here indicate that there is more band dispersion, and consequently lower effective masses, for ADT derivatives with the smaller

side group, TES. Overall, ADT-TES-F seems to be the best candidate for conduction of holes, in particular. From calculation of the effective mass tensors of these molecules, charge transport properties are expected to be best in a direction across the molecular planes or along the ADT backbone. Thus, one can conclude that for good charge mobility in thin films, the molecules should be arranged so that planes of the ADT backbones are in an a-top parallel arrangement with the molecules slightly offset along the long-axis of the molecular backbone, as if one had taken a slice through the ac plane of the single crystal.

Experimentally, valid photocurrent absorption and mobility measurement results are more common with ADT-TES-F than any of the other derivatives here. There have been some promising results made with doping ADT-TES-F with ADT-TIPS-CN. [22] The similar molecular shape and packing means that the charge transport properties should not significantly disturb those of pristine ADT-TES-F film/crystal. Thus similarity in structures and offset of HOMO and LUMO values make ADT-TES-F and ADT-TIPS-CN are good type II heterojunction candidates.

In conclusion, the reported results correspond well enough to experimental measurements to promote further theoretical investigation, such as use of time-dependent density functional, of these and similar molecules. The trends among comparable derivatives observed by experiment seem to hold up well under theoretical investigation.

TABLE 2.7: Effective mass eigenvalues and eigenvectors for holes and electrons of the anthradithiophene derivatives. The eigenvectors are expressed as components of the normalized real-space lattice vectors, $\hat{\mathbf{a}}$, $\hat{\mathbf{b}}$ and $\hat{\mathbf{c}}$. Table 2.4 gives the lattice parameters of the real-space lattice vectors. All effective masses are quoted in units of m_e , i.e. $m^* = m_{\text{eff}}/m_e$.

	Hole Effective Mass				Electron Effective Mass			
	m^*	a	b	c	m^*	a	b	c
ADT	>27	-0.07	-0.04	0.99	>44	-0.04	0.59	1.53
	5.9	1.13	0.20	-0.27	2.7	0.16	2.47	1.97
	1.5	0.05	2.53	2.32	1.1	1.12	-0.02	-0.46
ADT-	>55	-0.49	1.05	0.61	>53	-0.34	1.05	0.49
TES	2.5	-1.83	-0.01	-1.91	6.1	1.93	-0.08	-1.88
	0.86	0.67	-0.01	0.37	0.95	0.43	-0.03	0.61
ADT-	>73	0.56	-1.04	-0.64	>20	-0.67	1.04	0.83
TES-F	3.0	-1.97	-0.01	1.90	>9.9	-1.20	-0.11	1.80
	0.74	0.37	0.01	0.65	0.94	1.57	-0.01	-0.73
ADT-	>43	0.73	-1.09	-0.86	>45	-0.73	1.09	0.86
TES-	1.2	1.67	0.00	-2.01	1.9	1.72	0.00	-2.01
CN	0.71	-1.11	0.00	0.13	0.37	1.04	0.00	-0.05
ADT-	>180	-2.29	-1.55	2.16	>340	2.29	1.65	-2.19
TIPS	>75	0.15	1.22	-0.64	>30	-0.03	-1.09	0.46
	2.1	0.02	0.01	0.98	1.0	0.00	0.00	1.00
ADT-	>420	1.24	-1.15	-1.00	>190	1.16	-1.15	-0.93
TIPS-F	4.2	1.81	0.00	-2.22	>8.9	2.27	-0.04	-1.83
	1.1	1.36	0.00	-0.42	2.3	-0.44	0.00	1.37
ADT-	>220	2.15	-0.13	-1.85	>36	-2.69	0.53	2.23
TIPS-	6.0	2.56	-1.71	-2.16	>11	-1.97	1.61	1.79
CN	2.0	0.15	-0.09	0.88	4.5	0.23	-0.27	0.80
ADT-	>600	-0.14	0.79	-0.30	>58	0.15	-0.69	-1.33
TSBS-F	>80	0.20	-1.14	-1.33	>48	0.17	-1.20	-0.30
	1.3	1.00	0.01	0.00	8.5	1.00	-0.01	0.04

3 ELECTRONIC STRUCTURE OF INDENOFUORENE DERIVATIVES

1 Introduction

Over the last century, interest in and knowledge about extended hydrocarbons has increased to the point that certain hydrocarbons are considered to be good candidates for organic electronic devices.[6] Molecules with polycyclic backbones, such as pentacene and its derivatives, have shown good optical and electronic properties in their amorphous and crystalline forms. At room temperature, crystals and films of these molecules are unlikely to have mobilities on the order of inorganic semiconductors such as silicon due to many contributing factors. Structural defects, exciton formation, charge recombination and localization effects due to interaction of charge carriers with the electronic and nuclear vibrations all contribute to reduce charge carrier mobilities in organic films and solids. Defects within the lattice and molecular structure can also lead to electron trapping at low temperatures.[15, 1, 20] However, organic molecules with pentacene and other polycyclic hydrocarbons such as anthracene, dibenzopentalene and anthradithiophene as their backbone have been shown to have charge mobilities and other electronic properties such as on/off ratios within useful ranges, making them good candidates for organic electronics such as thin-film transistors, solar cells and photodetectors. In fact, single crystal charge mobilities up to $5\text{ cm}^2/Vs$ for pentacene have been measured.[10] Organic materials have the advantage of tunability, low production costs, flexibility and solution-processability.

Electronic coupling between neighboring molecules in a crystal is an important factor in charge transport properties. This can be described by the transfer integral in the tight-binding approximation, and is directly related to the degree of molecular orbital overlap between neighboring highest occupied molecular orbitals (HOMO) in the case of hole transport and lowest unoccupied molecular orbitals (LUMO) in the case of electron

transport. In planar π -conjugated materials such as pentacene and its derivatives, the HOMO and LUMO orbitals reside mainly on the backbone of the molecule. The overlap of the molecular orbitals, and consequently the molecular packing in the crystal, can be tuned to some extent by adding bulky side groups to the molecule.[47, 48, 49] In the case of indeno[1,2-b]fluorene derivatives, addition of the bulky side group triisopropylsilylethynyl induces an approximately planar-like packing in the crystal. These bulky substituents also kinetically stabilize the molecules compared to the more thermally unstable skeleton without side groups.[50, 27] The electronegativity and stability of the molecule can also be tuned by end-group functionalization, such as halogenation.

As has been the case with inorganic materials, if one molecule has promising properties, then isostructural analogues are of interest. Pentacene and derivatives functionalized with large side-groups have shown good results, although pentacene is prone to oxidative degradation.[51, 52] This can be reduced by functionalization,[27, 53] but isostructural analogues to pentacene such as anthradithiophene also show promising transport properties.[49] This chapter considers another isostructural analogue of pentacene, indeno[1,2-b]fluorene, also known as dibenzo[a,g]-s-indacene,[50]. I will be discussing the molecular and crystal properties of three indeno[1,2-b]fluorene derivatives that have been functionalized with triisopropylsilylethynyl (TIPS), see figure 3.1(a), one of which is represented in figure 3.1(b). This indenofluorene differs from pentacene and anthradithiophene, in that while it is planar and π -conjugated, the number of carbon atoms does not obey Huckel's rule for aromaticity and the backbone is in fact antiaromatic and has 20 π electrons, 2 fewer than pentacene, on its backbone.[52] Antiaromatic compounds tend to be highly unstable, but indeno[1,2-b]fluorene is kinetically stabilized by bulky substituents.

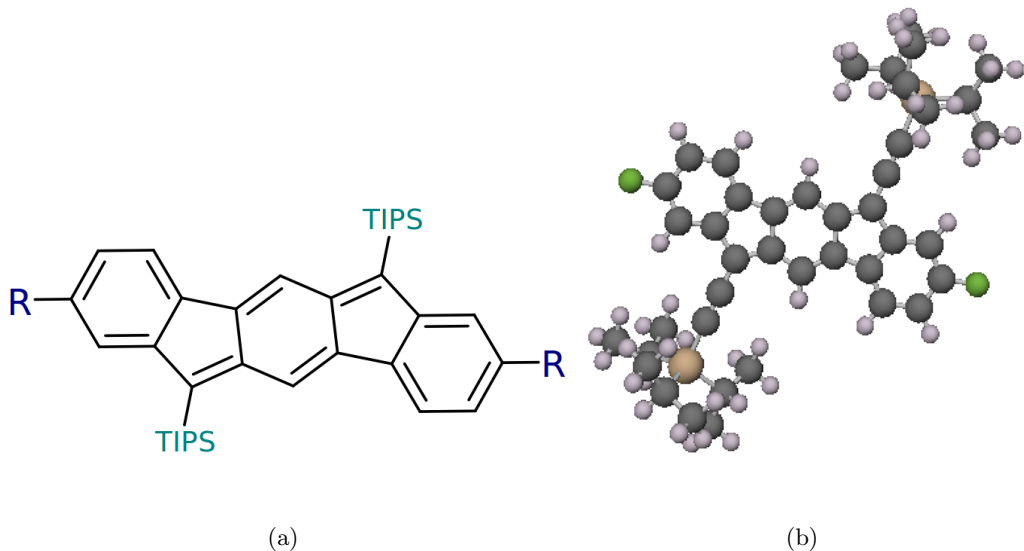


FIGURE 3.1: Functionalized indeno[1,2-b]fluorene. (a) Molecular diagram. $\mathbf{R}'=\text{H}, \text{F}$ or Br , and $\mathbf{TIPS}=\text{Si}i\text{-Pr}_3$ (triisopropylsilyl). (b) Indenofluorene functionalized with TIPS side group and fluorene end groups (IF-TIPS-F). The second image was generated by ECCE. [21]

2 Theory and Methods

The crystal structures for the three indenofluorene (IF) derivatives functionalized with triisopropylsilylethynyl bulky sidegroups were experimentally determined by the Haley lab at the University of Oregon.[54] In all the results reported here, the real-space lattice vectors have been redefined so that vectors \mathbf{a} and \mathbf{b} define the plane of IF backbones, and \mathbf{c} describes the vector crossing the planes, while still preserving the original crystal structure, see figure 3.4. The molecular geometry of each isolated molecule was optimized using density functional theory implemented in NWChem [23] with the B3LYP hybrid functional [41] in conjunction with the stepper energy minimization algorithm built into NWChem. NWChem uses a Gaussian basis set approach to calculate the Kohn-Sham orbitals, and the 6-31G basis set (6-311G basis set in the case of IF-Br) [42] was chosen. In this context, the stepper geometry optimization method searches for the ge-

ometry that corresponds to a minimum on the potential energy surface of the molecule. The energy tolerance of the geometry optimization was set at 10^{-8} eV. The relaxed and vertical energies of singly charged molecules were calculated in the same manner.

The projector-augmented wave method [31, 32] implemented in VASP [33, 34, 35, 36] within the generalized gradient approximation with the Perdew-Burke-Ernzerhof (PBE) exchange functional [55, 56] was used to determine the electronic and optical properties of the molecular crystals. A cutoff energy of 900 eV was used in these calculations, with Monkhorst-Pack grids in reciprocal space chosen as appropriate for the dimensions for each crystal structure: 3x4x2 for IF-TIPS, 4x4x2 for IF-TIPS-F, and 2x3x4 for IF-TIPS-Br. All density of states plots had Fermi smearing applied with $\sigma=0.05$ eV.

The effective mass was determined by assuming that, near the band maximum (minimum), the valence (conduction) band energy has the form of a three dimensional parabolic function with respect the Bloch wave vectors. The band energies for a three dimensional grid in reciprocal space about the extremum point for each valence and conduction band were calculated. Each calculation used the charge density file (CHGCAR) from the original DFT calculation for each molecular crystal, and Fermi smearing with $\sigma=0.03$ eV. A linear least squares fit was applied to the energies from this grid in order to determine the parabolic coefficients for the band energy $E(\mathbf{k})$ at the extremum point. These coefficients are used to approximate the second derivative of the band energy with respect to the Bloch wave vectors, and applied to equation 3.4 to calculate the effective mass tensor.

Due to the existence of other local maxima and minima in the valence and conduction bands within the Brillouin zone, the grid points used to calculate the parabolic functions for the absolute extrema have to be limited in range about the extremum in order to get a good fit. The range of grid points in reciprocal space about the extremum are chosen such that the energy range of these points is on the order of room temperature

thermal energy. Necessary conditions determining the choice of the ranges dE and dk were that 1. there be a good correspondence between the position and value of the extremum points of the fitted and DFT data, 2. the root-mean-square value of the fitted function with respect to the DFT energy values for the relevant data points was small (of order 10^{-4} eV), and 3. the resultant effective mass eigenvalues all had the same sign. Each effective mass tensor calculated is diagonalized to calculate its eigenvalues and eigenvectors. In some cases, due to the low dispersion of the transport band in a particular direction in k -space, an effective mass eigenvalue is strongly dependent on the choice of energy range and reciprocal space range of grid points about the extremum. In these cases a minimum value for the effective mass eigenvalue is quoted in table 3.6.

The optimized geometries for the isolated neutral molecules were also used to calculate values for the HOMO-LUMO gaps within the generalized gradient approximation with the PBE functional as implemented in VASP and analyzed at the Γ -point with Fermi-smearing of width $\sigma=0.026$ eV. In order to simulate an isolated molecule, the molecules were separated by a minimum of 12 Å on all sides.

3 Results and Discussion

3.1 Molecular properties

The halogenated IF-TIPS molecules and their crystals have many structural similarities to pentacene[13, 47] and anthradithiophene[39, 28] derivatives such as the conjugated, planar heterocyclic backbone and the large side-groups which induce a planar structure in the crystal. A big difference is that the pentacene and anthradithiophene obey Huckel’s rule for aromatic compounds, while the indenofluorene is antiaromatic ($4n$, $n=5$, π electrons). Consequently electrons will not be delocalized over the molecular backbone.

HOMO-LUMO gap, Ionization potentials, and Electron Affinities

Molecules with HOMO and LUMO levels offset from one another are potential candidates for compounds with type II bulk heterojunctions. The results for the calculated HOMO and LUMO levels are diagrammed in figure 3.2 and recorded in table 3.1. The experimentally determined HOMO-LUMO gap of IF-TIPS, 1.9 eV, agrees well with the calculated value using B3LYP. From the data, we observe that functionalization with the bulky TIPS side-group lowered the electron affinity of the molecule as well as the HOMO-LUMO gap. However, the HOMO-LUMO gap is still in the transparent range. Further end-group halogenation changed the electronegativity of the molecule and the HOMO and LUMO levels are shifted downward. Both IF-TIPS-F and IF-TIPS-Br could act as electron acceptors for ADT-TES-F, an organic material that has observable photocurrent in films, see section 4. The electron affinities are within the range of that of the good electron acceptor, C₆₀. The GGA HOMO-LUMO gaps generated in VASP underestimated, as expected, but they do show the same trend of decreasing HOMO and LUMO levels with higher halogenation, with the exception of the LUMO value for IF-TIPS-F.

The calculated adiabatic ionization potentials reflect the same trends seen in the HOMO levels calculated using B3LYP. The ionization potential increases as the halogenation of IF-TIPS goes down the periodic table. All the electron affinities are exothermic, expected for *p*-type semiconductors, and show the same trends of decreasing LUMO levels for the indenofluorene molecules in figure 3.2. The ionization potential (electron affinity) is defined as the difference between the free energy of a positively (negatively) charged molecule and a neutral molecule. The sum of the ionization potential and electron affinity for each molecule also shows the same trend to the calculated HOMO-LUMO gaps. For all the indenofluorene derivatives, the $IP + EA_{adiabatic}$ are approximately the same, as are the HOMO-LUMO gap (although about 2 eV higher than the HOMO-LUMO gaps).

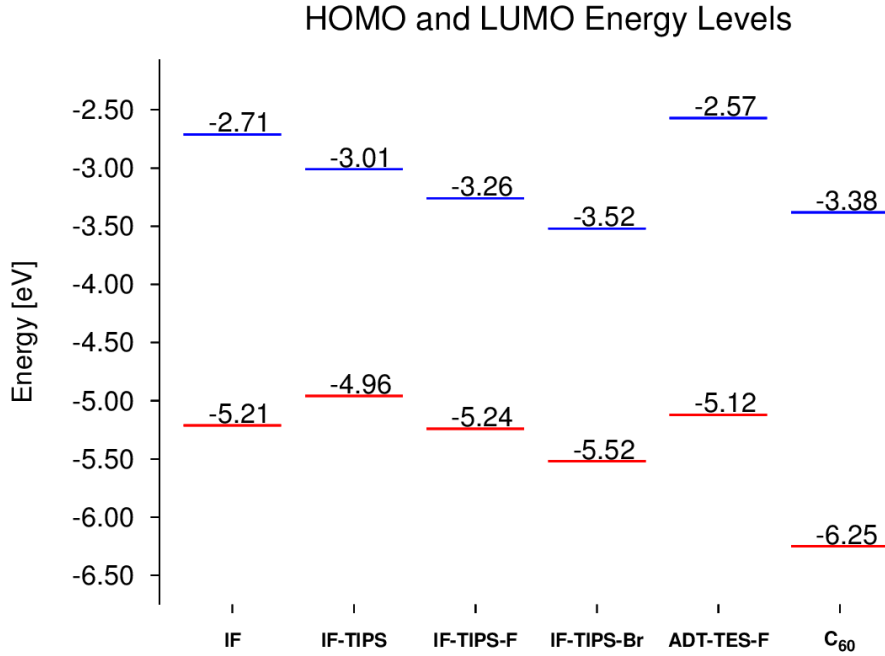


FIGURE 3.2: Diagram comparing the HOMO and LUMO levels of IF, IF-derivatives, ADT-TES-F, and C₆₀ buckyball. These are results from calculations using NWChem [23] with the B3LYP functional and 6-31(1)G Gaussian basis set.

TABLE 3.1: Table of calculated HOMO-LUMO gaps for isolated molecules. The molecules considered are indeno[1,2-b]fluorene (TIPS) and derivatives of IF that have been functionalized on either side with a triisopropylsilylethynyl (TIPS) side groups. Derivatives with fluorine (F), bromine (Br) or no end groups have been considered. The experimentally determined band gap for IF-TIPS is 1.9 eV [57]. The B3LYP column corresponds to results calculated using NWChem, and the GGA column is for results calculated in VASP when each molecule is surrounded by vacuum. All values are in units of electron volts.

molecule	B3LYP			GGA		
	HOMO	LUMO	HOMO-LUMO	HOMO	LUMO	HOMO-LUMO
IF	-5.21	-2.71	2.50	-	-	-
IF-TIPS	-4.96	-3.01	1.96	-4.63	-3.54	1.09
IF-TIPS-F	-5.24	-3.26	1.98	-4.83	-3.51	1.33
IF-TIPS-Br	-5.52	-3.52	1.99	-4.90	-4.63	1.27

TABLE 3.2: Vertical and adiabatic ionization potentials and electron affinities for IF-derivatives for isolated molecules (in eV). Here we define $IP = E(M^+) - E(M)$ and $EA = E(M^-) - E(M)$. $IP+EA_{adiabatic}$ is the sum of the adiabatic ionization potential and electron affinity for each molecule.

	IP		EA		IP+EA _{adiabatic}
	vertical	adiabatic	vertical	adiabatic	
IF	6.62	6.51	-1.28	-1.40	5.11
IF-TIPS	6.43	5.96	-1.57	-2.00	3.96
IF-TIPS-F	6.35	6.23	-2.13	-2.26	3.97
IF-TIPS-Br	6.57	6.46	-2.44	-2.57	3.89

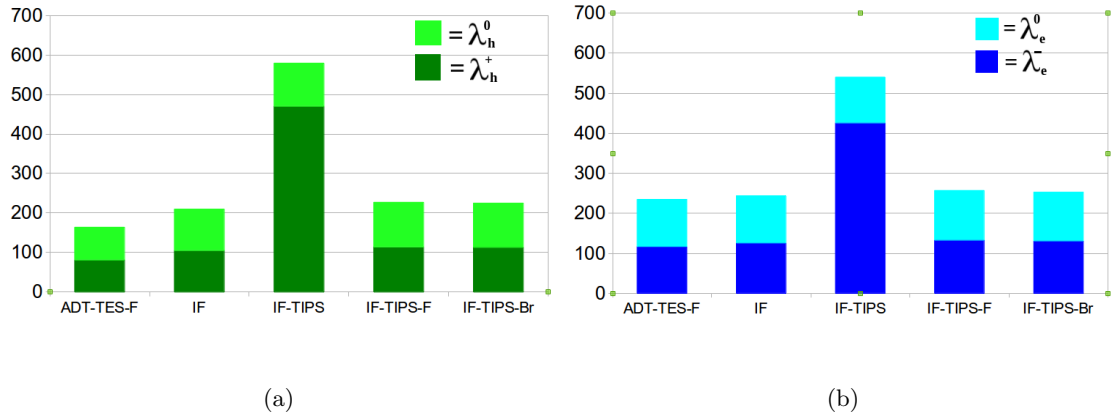
Reorganization energies

Hopping charge transport can be modeled as a charge transfer reaction where the charge carrier is transferred between two identical molecules. The charge carrier on a singly-charged molecule is transferred to a neutral molecule. This transfer involves the energy required to overcome the potential energy barrier due to the separation of the molecules, as well as the charge reorganization energies involved once the charge has transferred. The mobility of hopping transport is proportional to the probability per unit time that charge can be transferred between molecules, k_T . If Arrhenius kinetics is used to describe the hopping reaction, k_T can be written as [10, 58]

$$k_T = A \exp \left[-\frac{(\lambda - 2t)^2}{4k_B T} \right] \quad (3.1)$$

In equation 3.1, t is the transfer integral between the two molecules, and the prefactor A proportional to t^2 for weak intermolecular coupling between neighboring molecules.[10, 15] The transfer integral is strongly dependent on the distance and ori-

FIGURE 3.3: Charts showing intramolecular reorganization energies (meV) for holes λ_h and electrons λ_e of isolated molecules of the indenofluorene derivatives. The intramolecular reorganization energy for a hole(electron) $\lambda_{h(e)}$ is the sum of the relaxation energy of a cationic(anionic) molecule from the neutral geometry to the ionic geometry ($\lambda_{h(e)}^{+(-)} = E_0^{+(-)} - E_{+(-)}^{+(-)}$) and the relaxation energy of the neutral molecule from cationic(anionic) to neutral geometry ($\lambda_{h(e)}^0 = E_{+(-)}^0 - E_0^0$).[44] The reorganization energies for ADT-TES-F is included as a point of reference (see chapter 2)



entation of neighboring molecules with respect to each other. Furthermore, the lower the reorganization energy λ , the more likely the charge transfer will occur.

Figure 3.3 compares the reorganization energies of the indenofluorene derivatives. The reorganization energies here ignore the contribution from intermolecular polarization. IF-TIPS has a considerably higher hole and electron reorganization energies compared to indenofluorene itself and halogenated IF-TIPS, but the other indenofluorene molecules have reorganization energies approximately the same magnitude as ADT-TES-F. If one were to use these molecules to dope a pristine ADT-TES-F film, IF-TIPS-F and IF-TIPS-Br would be better choices due to their lower reorganization energies, making them better candidates than IF-TIPS [57] for formation of type-II bulk heterojunctions.

3.2 Crystal properties

Geometries, band structures, and density of states

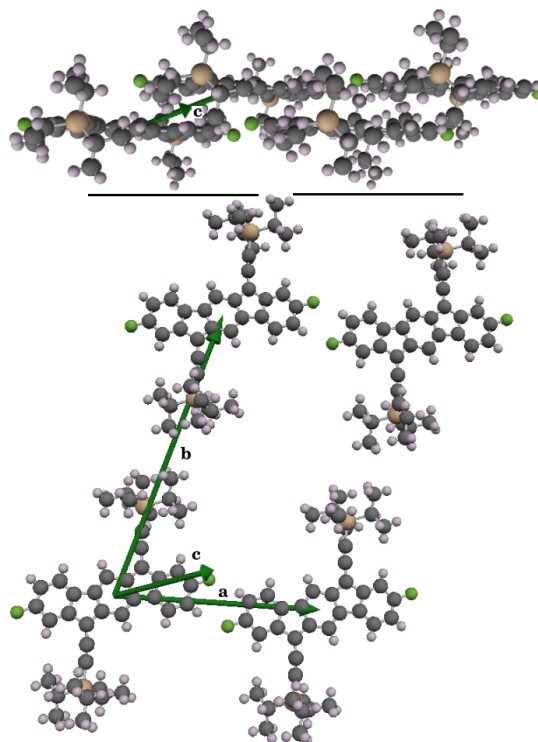


FIGURE 3.4: Crystal structure of IF-TIPS-F. Vectors **a** and **b** define the plane of backbones, and **c** defines the vector crossing the planes. **a** is be the vector with the greatest component along the long axis (see figure 3.6) of the molecular backbone.

The halogenated indenofluorene derivatives have crystal structures similar to those of the anthradithiophene derivatives in chapter 2 with a single molecule per unit cell. Vectors **a** and **b** define the planes of indeno[1,2-b]fluorene backbones, and all three molecular structures considered here have their backbones mostly parallel to this plane, see table 3.4. The IF-TIPS parent structure has two molecules per unit cell with a planar herringbone arrangement, with the backbone of one molecule rotated roughly 60 degrees with respect to the other, see figure 3.5.

TABLE 3.3: Chemical composition and experimental lattice parameters for indenofluorene derivatives with TIPS side groups. IF-TIPS has two molecules per unit cell. Note: The volume V_m quoted is the volume per molecule.

molecule	formula	a (Å)	b (Å)	c (Å)	α	β	γ	$V_m(\text{Å}^3)$
IF-TIPS	$2(\text{C}_{42}\text{H}_{52}\text{Si}_2)$	13.67	17.23	6.732	100.2°	30.99°	91.41°	927.7
IF-TIPS-F	$\text{C}_{42}\text{H}_{50}\text{F}_2\text{Si}_2$	14.85	22.06	7.91	58.36°	28.41°	73.94°	934.1
IF-TIPS-Br	$\text{C}_{42}\text{H}_{50}\text{Br}_2\text{Si}_2$	27.78	19.76	8.786	63.60°	50.50°	106.72°	950.7

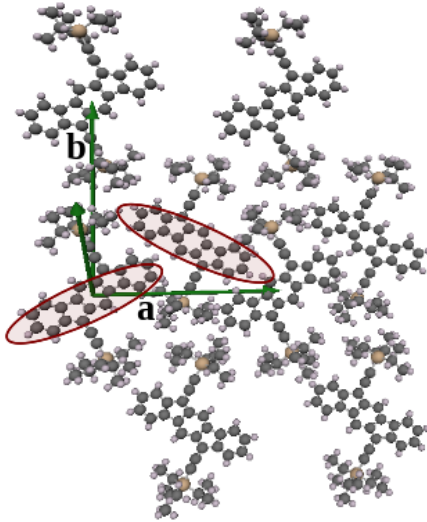


FIGURE 3.5: **ab**-plane of crystalline IF-TIPS. The structure has two nonparallel molecules per unit cell.^e

The lattice parameters for the indenofluorene derivatives here are listed in table 3.3. All the IF derivatives can be expressed as triclinic structures. Vector **a** is chosen to be the vector that has the largest component along the long axis of the molecular backbone. In the case of IF-TIPS, the choice of **a** is the same for both molecules, with the long axes of the two molecules sitting on either side of **a**. The backbones of these two molecules are slightly tilted about the long axis with respect to the **ab**-plane, and in opposite directions

TABLE 3.4: Orientation of molecules with respect to the lattice. Each column lists the angle between the two vectors indicated at the top of the column. $\hat{\mathbf{n}}$ represents the vector perpendicular to the indenofluorene (IF) backbone of the molecules, and \mathbf{l}_s and \mathbf{l}_l represent the short and long axes of the IF backbone. Figure 3.6 illustrates these vectors for IF-TIPS-F. The distance between lattice planes (\mathbf{c}_\perp) and angle of \mathbf{a} with respect to the \mathbf{ab} -plane normal are also listed for each crystal.

molecule	$\mathbf{a} \times \mathbf{b}$ and $\hat{\mathbf{n}}$	\mathbf{l}_l and \mathbf{a}	\mathbf{l}_s and \mathbf{b}	$\mathbf{a} \times \mathbf{b}$ and \mathbf{c}	\mathbf{c}_\perp (\AA)
ADT-TES-F	4.8°	20.4°	21.0°	59.1°	3.37
IF-TIPS (molecule 1) ^e	8.1°	33.6°	9.3°	63.8°	5.69
IF-TIPS (molecule 2) ^e	8.1°	26.8°	9.3°		
IF-TIPS-F	4.73°	14.0°	30.0°	68.0°	2.97
IF-TIPS-Br	12.28°	4.54°	61.5°	64.5°	3.51

with respect to each other. ^e End group halogenation forces the packing into a side-slipped parallel packing, see figures 3.4 and 3.9, and The size of the halogen substituent appears to be directly related to the volume per molecule in the crystal, see the last column in table 3.3. The spacing between the bromine substituted indenofluorene planes is higher than that of the fluorinated backbones. This explained by the fact that the backbones in crystalline IF-TIPS-Br are tilted 8° more with respect to the \mathbf{ab} -plane, see column 2 of table 3.4.

^e According to the experimental cif file[54], the backbone normals of the two molecules in the IF-TIPS unit cell are oriented 14.7° with respect to each other, with their long axes 60.3° with respect to each other.

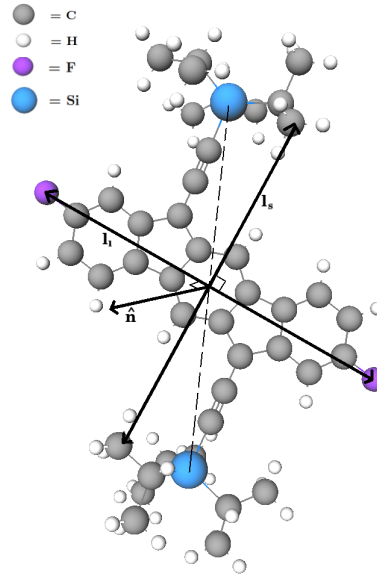


FIGURE 3.6: Molecular structure of IF-TIPS-F overlaid with diagrams of the indeno[1,2-b]fluorene skeleton's long axis (\mathbf{l}_l), short axis (\mathbf{l}_s), and backbone normal ($\hat{\mathbf{n}}$). This picture was generated using Ecce [21].

The arrangement of the molecules within the crystal lattice is important because this arrangement determines the degree of overlap for the molecular orbital corresponding to the charge carrier. If band-like transport will occur within the crystal, the overlap needs to be high for charge delocalization. As a single crystal, the closer packing of the IF-TIPS-S planes is promising for good one-dimensional charge transport across the planes, and a low effective mass is expected. Molecular orbital overlap is also important in charge transfer reactions such that occur in hopping transport or in bulk heterojunctions. For doping of pristine ADT-TES-F,[57] crystalline IF-TIPS-F has the closest molecular orientation and unit cell to that of ADT-TES-F, and is potentially a good electron acceptor that would result in a low level of disruption of the crystal structure of ADT-TES-F and its associated electronic charge transport properties.

A qualitative view of the degree of molecular orbital overlap can be determined from the single-electron valence and conduction band energy dispersions, see table 3.5 and figure 3.7. The band dispersion for the IF-TIPS lattice is very low, and observable

currents through pure IF-TIPS films upon photo-excitation are not expected. By contrast, the band dispersions of IF-TIPS-F and IF-TIPS-Br are higher than that of ADT-TES-F, an organic crystal that is known to have observable conductivity. Thus, purely from a band structure approach, we conclude that the molecular orbital overlap is relatively high and halogenated IF-TIPS crystals have high mobilities.

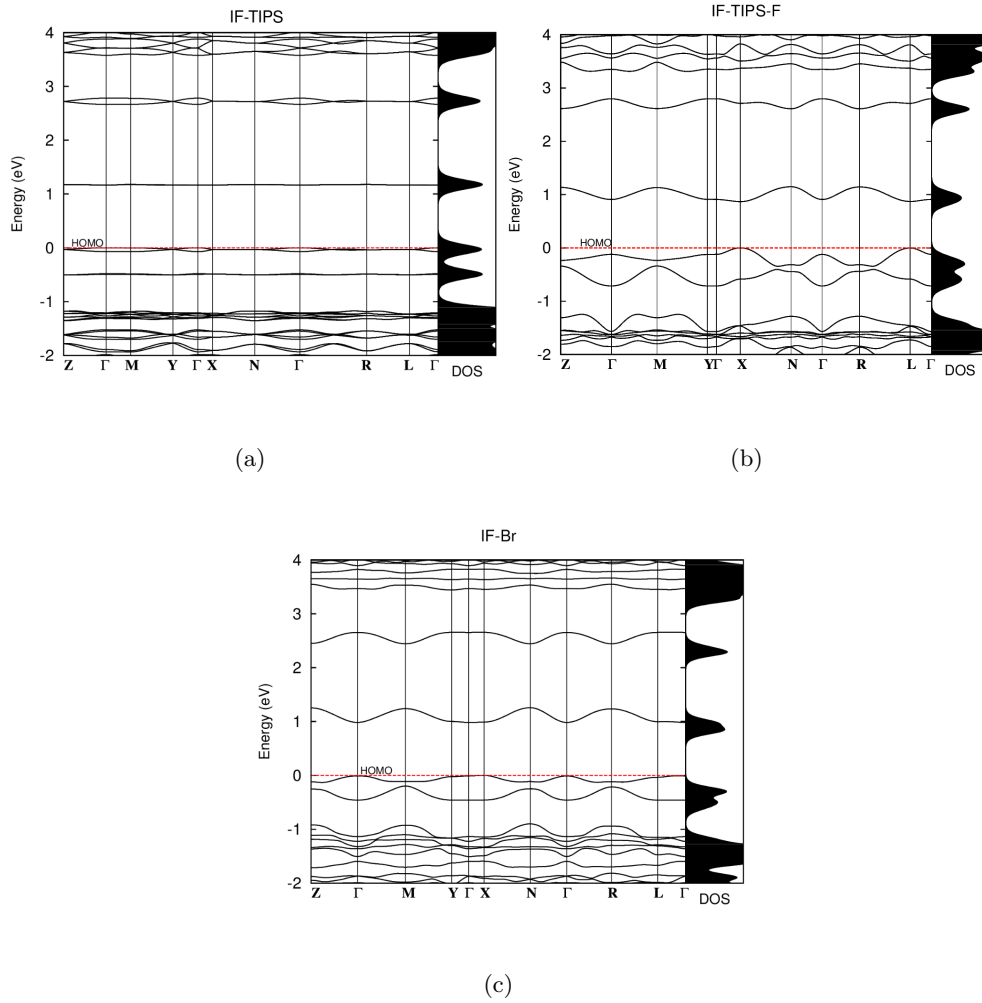


FIGURE 3.7: Band structures of single crystal indenofluorene derivatives. The reciprocal coordinates of the high-symmetry points used in the band structures - Γ , X, Y, Z, L, M, N, R - are, expressed in reciprocal space lattice vectors, $(0,0,0)$, $(0.5,0,0)$, $(0,0.5,0)$, $(0,0,0.5)$, $(0.5,-0.5,0)$, $(0,0.5,0.5)$, $(0.5, 0, 0.5)$ and $(0.5,-0.5,0.5)$ respectively.

TABLE 3.5: Details about the valence and conduction bands for single crystals of each indenofluorene derivative, including the band dispersions. The valence band maxima (VBM) correspond to the HOMO levels of the isolated molecules, and the conduction band minima (CBM) with the LUMO levels. The symbols used for the k-points correspond to those described in figure 3.7. These values are calculated using the PBE functional in VASP. All values quoted are in eV. The calculated values for anthradithiophene with trisopropylsilylethynyl and fluorine end group substituents (ADT-TES-F) serve as reference points.

	Band gap	Valence Band			Conduction Band		
		VBM	k-point	dispersion	CBM	k-point	dispersion
ADT-TES-F	1.06	0.558	M	0.526	1.650	X	0.209
IF-TIPS	1.16	-0.470	Γ	0.037	0.693	Γ	0.015
IF-TIPS-F	0.87	-0.089	X	0.348	0.779	X	0.279
IF-TIPS-Br	0.98	-0.216	X	0.131	0.767	Γ	0.274

Effective masses

We have already stated that conduction through the IF-TIPS crystal is unlikely, but could potentially be good in IF-TIPS-F or IF-TIPS-Br provided that localization effects do not overpower any delocalization through the crystal lattice. Higher degrees of intermolecular charge transport are expected between the planes and along the direction in which delocalization within the molecule occurs, see section 3.1. Since the backbone of the indeno[1,2-b]derivatives are antiaromatic, the eigenvector corresponding to the lowest effective mass is expected to point across the planes.

According to the Drude model, the temperature independent effective mass is inversely proportional to the conductivity.

$$\mu = \frac{e\tau(T)}{m_{\text{eff}}} \quad (3.2)$$

As temperature increases, phonons will decrease the mean free path of charge carriers in the defects and consequently the scattering time τ . τ is also limited by the uncertainty

principle, which adds a necessary condition for band-like transport.[1]

$$\tau(T) \ll \delta E \quad (3.3)$$

Thus for any realistic mobility due to tunneling (band-like transport), the band dispersion (δE) cannot be too small, otherwise localization effects will dominate the charge transport properties in the crystal. From another perspective, if the mean free path is much greater than the lattice vector lengths, then band transport can occur ($\bar{l} \gg a$).[2, 1] If this is not the case, then hopping transport is likely to dominate. The mean free path is associated with the relaxation time by the average velocity of the charge carrier, $v_{avg} = \tau \bar{l}$. The Drude model is too simplistic for complex materials like organic semiconductors, and the effective masses will be higher due to interaction of the charge carrier with molecular and crystal vibrations. However, low effective mass eigenvalues will directly correspond to areas of high HOMO (or LUMO) overlap, and is a qualitative measure of the transfer integral. Lower effective masses correspond to higher transfer integrals.

The effective mass tensor was calculated using equation 3.4 derived from a semi-classical model for an inorganic crystal.[19, 45]

$$\left(\frac{1}{m^*} \right)_{ij} = \frac{1}{\hbar^2} \frac{\partial^2 E(\mathbf{k})}{\partial k_i \partial k_j} \quad (3.4)$$

Table 3.6 contains the results of these calculations, expressed in terms of diagonalized effective masses and their corresponding eigenvalues. The low band dispersion of the IF-TIPS valence and conduction bands resulted in high calculated effective masses as expected. By contrast the halogenated IF-TIPS crystals each had one direction in which the effective mass was low. IF-TIPS-F had the lowest effective mass eigenvalue for both hole and electron carriers, which corresponded well with the close, parallel molecular packing of the crystal. For both the low hole and electron effective masses of the indenofluorene derivatives, the corresponding eigenvector had a small or negligible component along the (normalized) \mathbf{b} lattice vector. The lattice vector \mathbf{b} points across the molecule's bulky

side groups where there is minimal orbital contribution to the HOMO and LUMO. This is slightly less clear in the case of IF-TIPS-Br, where the **b** component is not negligible. This is clarified upon examination of the **ab** plane for this molecule in figure 3.9. The eigenvector points along a direction that has a large component along the indenofluorene backbone and the vector **c**, and the **b** direction does not point directly across the bulky side groups. In figures 3.8 and 3.9, lattice vectors and effective mass eigenvectors are superimposed over slices through the crystal. For all three molecules, the eigenvector corresponding to the lowest effective mass points out of the **ab**-plane, and one-dimensional transport is expected to occur in single crystals of these molecules.

TABLE 3.6: Effective mass eigenvalues and eigenvectors for holes and electrons of single crystal indenofluorene derivatives. The eigenvectors are expressed in terms of components of the normalized real-space lattice vectors, $\hat{\mathbf{a}}$, $\hat{\mathbf{b}}$ and $\hat{\mathbf{c}}$. All effective masses are quoted in units of m_e .

molecule	Hole Effective Mass				Electron Effective Mass			
	m^*	a	b	c	m^*	a	b	c
IF-parent	>52	0.00	1.02	-1.74	>130	1.0	-0.01	0.01
	8.0	0.00	-1.73	0.99	>80	-0.01	-1.95	1.46
	3.3	1.0	0.00	0.00	9.4	0.00	0.46	-1.38
IF-F	>28	1.26	1.31	-1.82	>25	1.58	1.28	-2.09
	3.5	-1.95	0.12	1.85	7.4	-1.74	0.34	1.47
	0.60	-0.44	-0.01	-0.59	0.68	-0.28	-0.01	-0.74
IF-Br	>16	-2.62	0.60	1.87	>26	-2.63	0.64	1.88
	6.0	-0.46	1.66	-1.06	9.4	-0.43	1.68	-0.98
	1.0	-0.18	0.36	0.87	0.79	-0.04	0.12	0.94

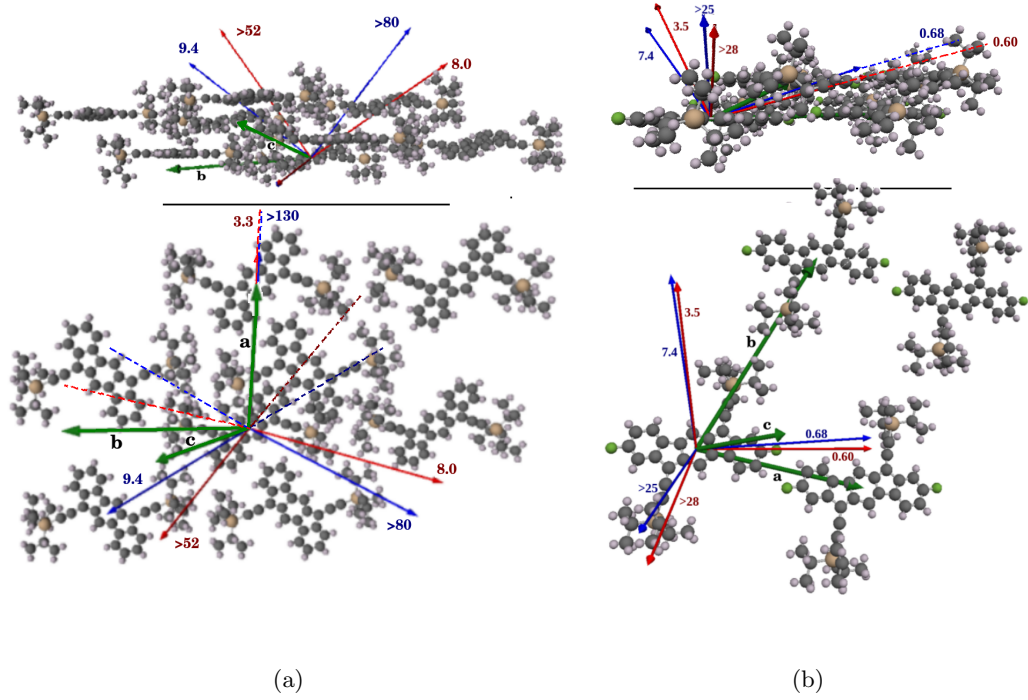


FIGURE 3.8: Crystal structure and effective mass eigenvectors of molecules with an indeno[1,2-b]fluorene skeleton. (a) IF-TIPS and (b) IF-TIPS-F crystal structures are overlaid with their lattice vectors (green) and calculated effective mass eigenvectors for both holes (red) and electrons (blue). The label on each eigenvector is the corresponding eigenvalue, the effective mass for that direction in units of electron mass. For each crystal structure, perspectives of a slice through the planes (upper) and of a single plane (the *ab* planes) (lower) are shown.

4 Summary and Conclusions

We have reported band structure and primitive effective mass values for indeno[1,2-b]fluorene derivatives with triisopropylsilylethynyl side group substituents. The thin bands of IF-TIPS, which indicate a low transfer integral, combined with the high reorganization energy for either charge carrier indicate that localization effects will dominate in a crystal or film composed of IF-TIPS molecules. Thus we expect to see fluorescence due to exciton recombination in such a crystal. The band structures of the halogenated IF-TIPS molecules however have promising properties, and may have good carrier mobilities, par-

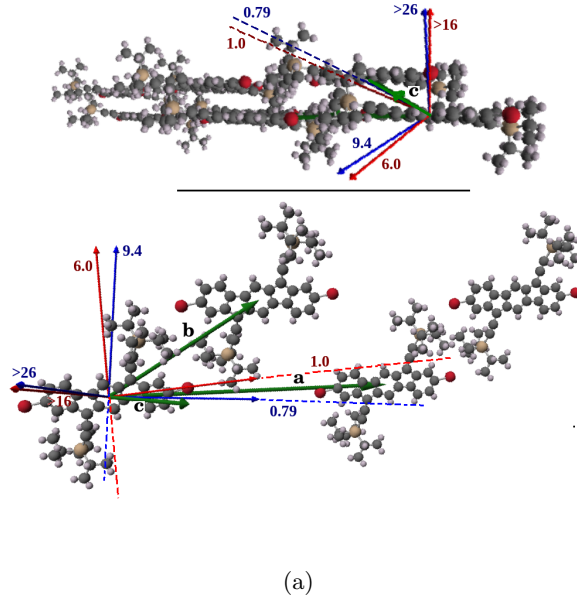


FIGURE 3.9: Crystal structure and effective mass eigenvectors of molecules with an indeno[1,2-b]fluorene skeleton *continued*. IF-TIPS-Br crystal structure is overlaid with its lattice vectors (green) and calculated effective mass eigenvectors for both holes (red) and electrons (blue). The label on each eigenvector is the corresponding eigenvalue, the effective mass for that direction in units of electron mass. For each crystal structure, perspectives of a slice through the planes (upper) and of a single plane (the **ab** planes) (lower) are shown.

ticularly IF-TIPS-F which has closely packed planes of indenofluorene backbones.

The crystal structure of IF-TIPS-F and recombination energies match well with that of ADT-TES-F, a derivative which has shown promising charge transport properties. The combination of IF-TIPS-F and ADT-TES-F molecules is a type II bulk heterojunction, and IF-TIPS-F is potentially candidate to tune the electronic properties of ADT-TES-F without large changes to the crystal structure.

Further research on these molecules using time-dependent density functional theory, in conjunction with a dispersion energy correction or range-separated functionals to account for the van der Waals interactions between molecules should shed light on excited optical properties, particularly fluorescence and absorption, for these molecules. Inves-

tigation into the effects of antiaromaticity on these molecules compared to the aromatic backbones in pentacene and anthradithiophene derivatives is also a topic of interest. It would also be useful to theoretically investigate a wider range of indeno[1,2-b]fluorene derivatives as well as molecules with different indenofluorene backbones.

5 Acknowledgments

I would like to acknowledge and thank Randolph Beerwerth for performing the effective mass calculations for these molecules.

4 *AB INITIO* CALCULATIONS TO EXPLORE COVALENT MECHANOCHEMISTRY

1 Introduction

Covalent mechanochemistry involves the investigation and manipulation of covalent bonds, or interactions. In order for a stable molecule (reactant) to break into two parts (products), an energetic barrier has to be overcome. According to the Maxwell-Boltzmann probability distribution, such a reaction may spontaneously occur but these tend to be 'rare events' such that may take much longer than a scientist's lifetime to occur. Use of catalysts, thermal energy, photoexcitations, electricity, or mechanical force can all be used to lower overcome the energy barrier for the slow reaction to speed it up. This chapter focuses on modeling how mechanical force can be used in a covalent bond breaking reaction.

Bond strength is, by definition, the lowest force at which a bond is most likely to break. Bond strength is dependent on temperature, time and force loading rates. Knowledge about how these factors affect the strength of bonds enables a deeper analysis of how atoms interact within a molecule. Mechanocatalysts are materials that contain a latent catalyst that is activated when a specific bond is broken. Bond strength information is important to determine what circumstances are necessary to activate the catalyst.

2 Theory

Mechanical bond dissociation experiments have been modeled theoretically using molecular dynamics, but this can be time consuming and computationally demanding. Furthermore, molecular dynamics calculations correspond to force loading rates on the order of 10^{11} nN/s, which is orders of magnitude larger than the loading rates that occur

in atomic force microscopy experiments. Use of density functional theory has been useful in modeling mechanically-induced chemical reactions, particularly those with low loading rate such as is found in atomic force microscopy experiments (AFM), which have loading rates on the order of nN/s.[9]

There are two approaches in the use of density functional theory: isostructural and isotensional. In the isotensional approach, force is a fixed control parameter in the calculations, while in the isostructural approach [59, 60] the distance between two atoms on a molecule, the reaction coordinate, is the control parameter from which forces can be determined. In this chapter, the focus is on the isostructural approach in using density functional theory calculations to simulate covalent mechanochemical reactions, the basis of which is the COGEF potential.

While COGEF potentials may not give details about what happens in the transition state, we can deduce bond strengths and dissociation energies from the potential energy surface by looking at the energy differences and potential energy gradients of each reaction.

2.1 COGEF potential and the tilted potential energy surface

Modeling of the breaking of a covalent molecular bond by mechanical force using density functional theory begins with the molecule in its equilibrium geometry. A reaction coordinate is chosen, generally the distance between two atoms on the molecule, and the molecule is stretched in a stepwise fashion along the reaction coordinate. In each step, the structure from the previous step is stretched along the reaction coordinate by a small amount and then its geometry is optimized to find its lowest energy structure with the geometric constraint that the value of the reaction coordinate for that step is fixed. These calculations form the basis for a potential energy profile called the COGEF, “CONstrained Geometries simulate External Force”, potential. It is the COGEF potential from which an external force can be simulated.[60] Examples of COGEF potentials for small molecules can be found in section 3 in this chapter.

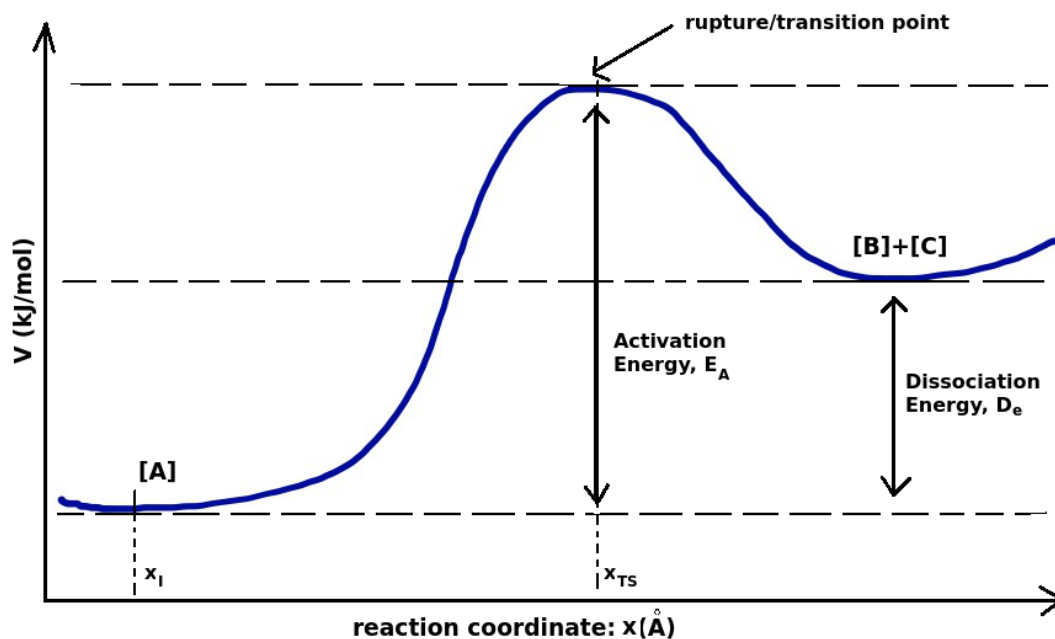


FIGURE 4.1: Example of a potential energy surface with respect to a reaction coordinate, corresponding to a chemical reaction such as $[A] \rightleftharpoons [B] + [C]$.

In an endothermic chemical reaction, an input of energy is required to overcome a energetic barrier (E_A) to go from the reactant ($[A]$) to the products ($[B]+[C]$), see figure 4.1. Application of mechanical force to the ends of a molecule causes bonds within the molecule to stretch, weakening these bonds and effectively lowering the activation energy, E_A , required to break a bond in a molecule. An applied external force, F , tilts the potential energy profile by reducing the potential energy by $-F \cdot x$. Here x is the distance that the molecule has been stretch from its relaxed state, with respect to the reaction coordinate. This is called a tilted potential energy surface, V_{eff} ,

$$V_{\text{eff}}(x) = V(x) - (x - x_0) \cdot F. \quad (4.1)$$

In equation 4.1, x_0 is the reaction coordinate length that corresponds to the relaxed molecule before it has been stretched.

Figure 4.2 is a diagram of the tilted energy profiles of a Morse potential, a good

model for a single covalent bond, tilted with different external applied forces. The external force modifies the energies and positions of the transition and initial states, and hence the activation energy of the bond is changed. In general, the transition state (x_{TS}) is the point at which the molecule breaks and corresponds to a maximum on the potential energy surface. The initial state (x_I) corresponds to the value of the reaction coordinate of the potential well on this tilted surface, and the activation energy, E_A is the difference in energy between the two points x_I and x_{TS} . At zero applied force, $x_I = x_0$.

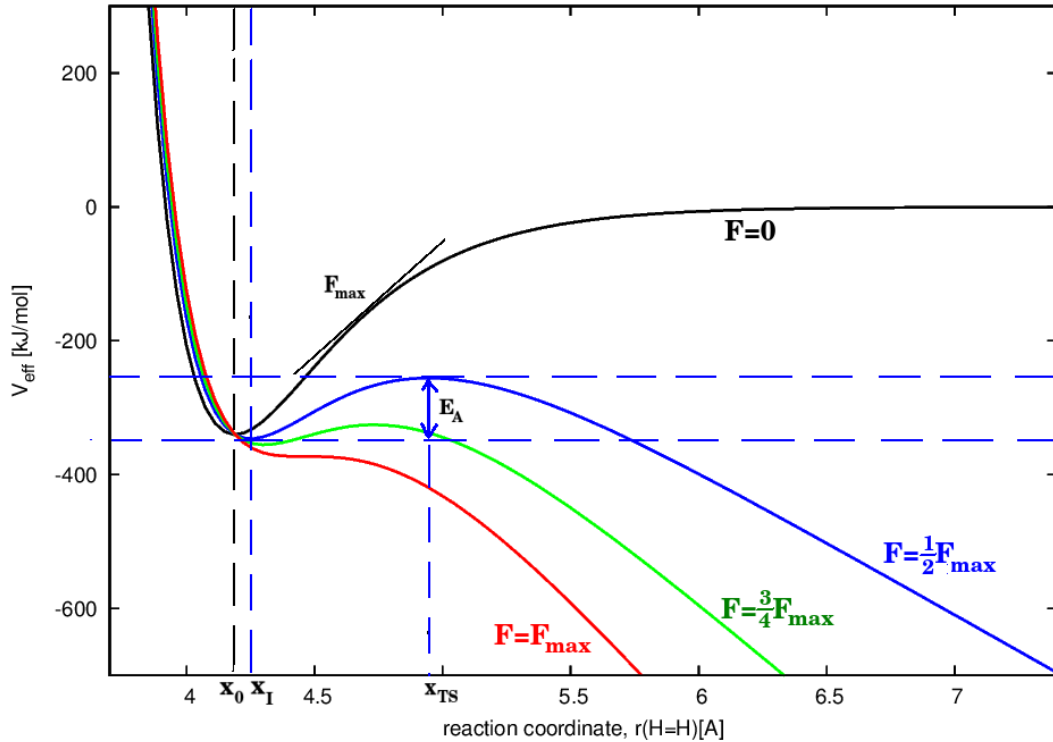


FIGURE 4.2: Model of a single C-N bond (see table 4.1). Morse potential with $D_e=340$ kJ/mol and $F_{max}=7.2$ nN with applied external forces of $F=0$ (black), $0.5 \cdot F_{max}$ (blue), $0.75 \cdot F_{max}$ (green) and F_{max} (red). These graphs correspond to a model for the C-N bond in dimethyl ammonium. F_{max} is the maximum slope of the potential, see equation 4.11. A positive force elongates the minimum energy bond length and lowers the activation energy required to break the bond.

Both x_I and x_{TS} correspond to points where $V'_{eff}(x) = 0$.

$$F = V'(x_I) = V'(x_{TS}). \quad (4.2)$$

Consequently, the derivative of equation 4.1, directly associates any applied force less than the maximum slope on the COGEF potential, $F = F(x_I) = V'(x_I) < F_{max}$, with a reaction coordinate length, x_I . The transition state, and consequently $F(x_I)$ defines the activation energy, so the reaction rate is dependent on the applied force, $k = k(x_I) = k(F)$. For forces greater than F_{max} , bond dissociation is expected to be spontaneous.[61]

2.2 Arrhenius model and the Harmonic approximation

Consider a general reaction $A \rightleftharpoons B + C$ such as is depicted in figure 4.1. In 1884 van't Hoff proposed [62] that

$$\left(\frac{\delta(\ln k)}{\delta T} \right)_P = \frac{\Delta U^0}{RT^2} \quad (4.3)$$

in order to account for the temperature dependence of the rate of a reaction. Here ΔU^0 is the change in internal energy required for the reaction, which is later expressed at the activation energy E_A . k is the ratio of the forward and back rate constants for the reaction,

$$k = \left(\frac{[B][C]}{[A]} \right)_{eq} = \frac{k_F}{k_B}, \quad (4.4)$$

In 1889, Arrhenius concluded that a temperature-dependent equilibrium exists between the reactant and product concentrations that follows van't Hoff's equation since temperature effects in the reaction are too large to be explained by the effect of temperature on the transition (or activation) energy, E_A of the reaction. Thus, the Arrhenius equation is known as the integral of equation 4.3,

$$k = Ae^{-E_A/kT}. \quad (4.5)$$

The Arrhenius kinetics model can be used to approximate the breaking of bonds in a molecule that is stretched. The temperature effect on the activation energy, E_A , is not considered to be large enough to be significant. A is a pre-exponential factor that

has the units of frequency for a first order reaction, and has been called the “frequency factor”.[62]

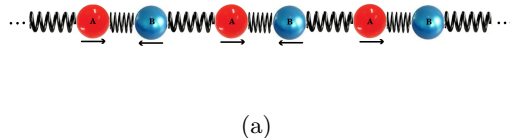


FIGURE 4.3: Infinitely long one-dimensional diatomic molecule.

An approximation for the frequency factor can be made by modeling the molecule as an infinitely long one dimensional diatomic polymer ...ABABABA.... as depicted in figure 4.3. Each bond in the molecule is assumed to have a harmonic potential and the frequency factor for the rate of bond breaking is approximated as the maximum frequency of an acoustic phonon for such a molecule, where $M(A) > M(B)$.[60]

$$A(z_a) = \frac{1}{2\pi} \sqrt{\frac{2V''(z_a)}{M(A)}} \quad (4.6)$$

At this frequency, adjacent components, A and B, are moving in opposite directions, facilitating bond breaking. this is depicted by the arrow in figure 4.3. In equation 4.6, the spring constant K of the bonds is assumed to be determined by the second derivative of V_{eff} at x_I , which is equal to the second derivative of the potential along the reaction coordinate: $K = 2V''(x_I)$. The activation energy depends on the transition state but also requires a zero-point correction corresponding to the ground state of a quantum harmonic oscillator:

$$E_A(x_I) = V_{\text{eff}}(x_{TS}) - V_{\text{eff}}(x_I) - \frac{1}{2}hA(x_I) \quad (4.7)$$

This model does have room for improvement since it does not take into account any two dimensional nature of the molecule, the finite length of the molecule, or the fact that the molecule of interest is not usually made up of only two components. That being said, theoretical results using this model have agreed well with experimental values, see

section 4. Improvements to consider would include accounting for bonds not parallel to the reaction coordinate. Does bond shearing occur in these cases? Also, rings within the stretched molecule, unless they are broken could be considered as a single unit in the molecule and have a much higher mass - affecting the frequency factor, see equation 4.6.

Using the Arrhenius kinetics model, the probability density of a bond rupturing event, $\rho(t)dt = dN(t)$, can be expressed as a standard exponential decay equation.

$$\frac{dN}{dt} = kN \quad (4.8)$$

where k is the reaction rate approximated in equation 4.5. If there is an experimental force loading rate of f_0 , the probability density of a bond at a given force $F = f_0 t$ can be calculated with a change of variable. Numerical integration of 4.9 with the assumption that one begins with an unbroken bond ($N(F = 0) = 1$), yields $\rho = \frac{dN(F)}{dF}$ where [61, 60, 63]

$$dN(F) = \frac{k(F)N(F)}{f_0} dF = \frac{N(F)}{f_0 \tau(F)} dF \quad (4.9)$$

in which $\tau(F) = 1/k(F) = 1/k(x_I)$.

Morse potential model

The Morse potential is a model for the potential energy surface of a single covalent bond, see figure 4.4. This potential is defined by a dissociation energy, D_e and the width of the potential, determined by β .

$$V(x) = D_e(1 - e^{-\beta(x-x_0)})^2 \quad (4.10)$$

β can be shown to be related to the maximum slope of the potential, which is the maximum force.

$$\beta = 2F_{max}/D_e \quad (4.11)$$

Details of a Morse potential and a tilted Morse potential have already been described in sections 2.1 and 2.2. Diatomic molecules have a COGEF potentials that match well

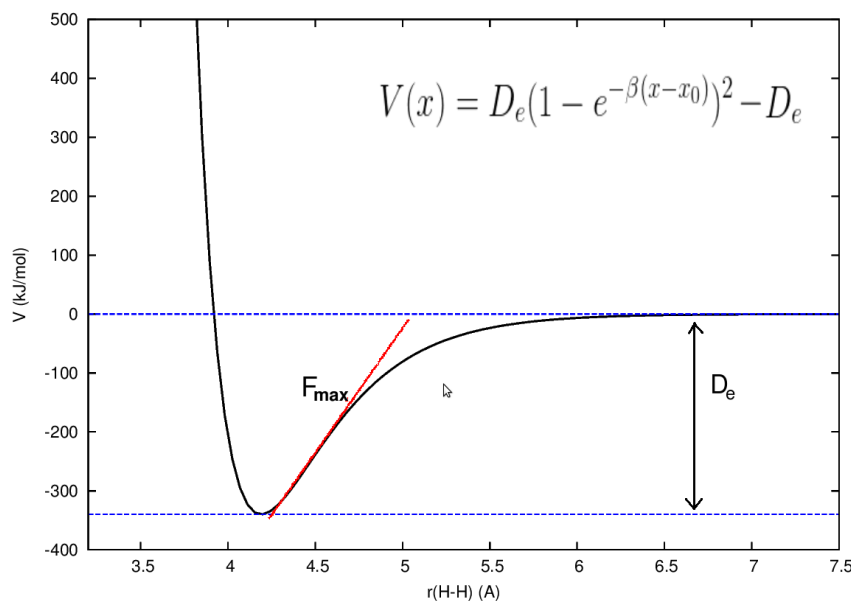


FIGURE 4.4: Plot of a Morse potential with $D_e = 340$ kJ/mol and $F_{\max} = 7.24$ nN. These values correspond to the values calculated for the C-N bond in dimethyl ammonium.

with a Morse potential, but the fit to a Morse potential is not as good when modeling larger molecules because the potential energy of more than one bond is involved when a molecule is stretched, see section 3 and figure 4.10(a). However, a Morse potential can still be used as an approximation with $D_e = \lim_{x \rightarrow \infty} V(x) - V(x_0)$ where x_0 is where the potential is at a minimum. The assumption made is that when a molecule is stretched to its breaking point, the forces and energies required to break the weakest bond are the same as if there was only the one bond to break.

Analysis of the Arrhenius model in the context of the Morse potential

In the following figures, the effects of different variables on the probability of a bond breaking are examined by using a Morse potential model, discussed in section 2.2, for the C-N bond in dimethyl ammonium as an example. In this example, $D_e = 340$ kJ/mol and $F_{\max} = 7.2$ nN (see table 4.1). External factors such as a force loading rate and temperature affect the bond strength, and the effect of these factors can be observed within Arrhenius kinetics applied to a Morse potential model. Figure 4.5 demonstrates the effect of different

loading rates on the probability of bond breakage with respect to applied external force at 300K. As the force loading rate increases, the force at which there is the most breakage (the bond strength) increases, but the probability distribution around that force broadens. Increasing force with increasing loading rate may seem counterintuitive, however at higher loading rates there is less time for thermal energy to overcome the activation energy barrier of the bond and the lifetime of the bond decreases.

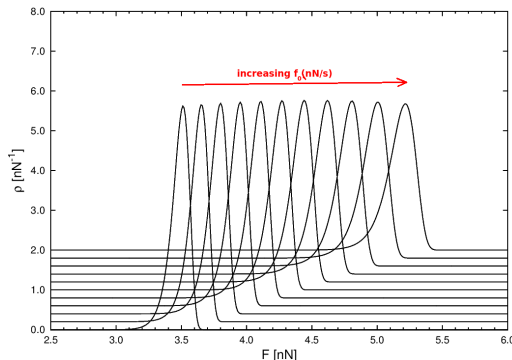


FIGURE 4.5: The effect of varying loading rates on the probability of bond breakage with respect to external applied force. Plot of probability of C-N bond breaking vs applied force for loading rates in powers of 10 from 10 pN/s to 100 mN/s, using a Morse potential model and Arrhenius kinetics at 300K with $D_e = 340$ kJ/mol and $F_{max}=7.2$ nN

Conversely, if the loading rate is fixed at 10 nN/s and the temperature is varied, the bond strength decreases with increasing temperature, see figure 4.6. This is expected, the reaction is thermally activated and higher temperatures increase the probability that the activation energy of the bond can be overcome.

The theoretical dissociation energy and maximum force from a COGEF potential will vary, depending on the basis set chosen and the functional used. In the light of this theoretical uncertainty, a discussion on the effect of different values of the dissociation energy and maximum force is included below. Using the same Morse potential model for the C-N bond described above, figures 4.7 and 4.8 show the effect of a change in the dissociation energy and maximum force respectively within 25 percent of $D_e = 340$ kJ/mol and $F_{max}=7.2$ nN respectively. For both bond dissociation energy and maximum forces,

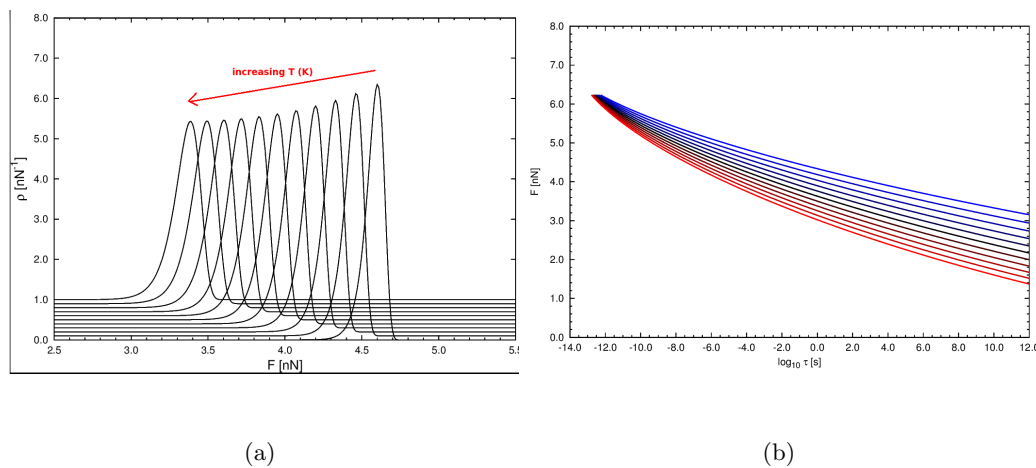


FIGURE 4.6: The effect of increasing temperature from 200K to 400K (blue to red) in steps of 20K on the probability of bond breakage with respect to external applied force. A Morse potential model for the C-N bond and Arrhenius kinetics at 300K is used with $D_e = 340$ kJ/mol and $F_{max}=7.2$ nN. (a) is the plot of probability of a bond breaking vs applied force. (b) is the plot of

increasing either value increases the bond strength. However, the width of the probability curve with respect to force applied decreases as the dissociation energy decreases, but increases if the maximum force is increased. This is reflected in the plots of the applied force and lifetime τ of a bond. For shorter lifetimes, most probable force at which the bond will break increases with decreasing time. The bond strength increases with higher dissociation energies. Figure 4.7 shows that an underestimated dissociation energy has more effect on the bond strength than an overestimated energy.

3 Small Molecules Test

One can use small molecules to get a rough comparison of bond strengths and dissociation energies for bonds in much larger molecules. This principle was applied by Grandbois [64] to get an idea of which bonds ruptured when an external load was applied to a molecule using an atomic force microscope. This model was revisited in the paper by

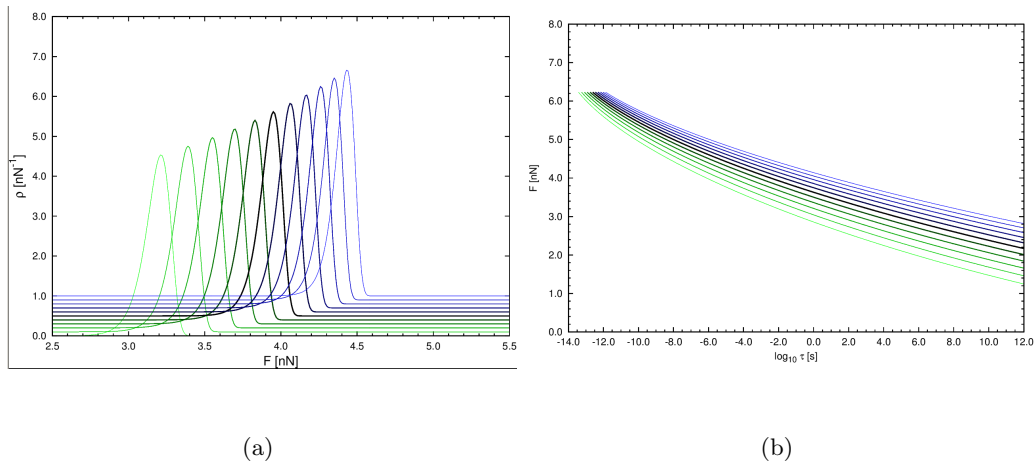


FIGURE 4.7: The effect of a change in the dissociation energy within a 25% range above (blue) and below (green) $D_e = 340$ kJ/mol on C-N bond breakage. A Morse potential with $F_{max}=7.2$ nN is assumed, and Arrhenius kinetics are applied under the conditions of 300K and loading rate 10 nN/s. The solid black lines correspond to $D_e = 340$ kJ/mol. (a) is a plot of probability vs applied force, and (b) demonstrates how

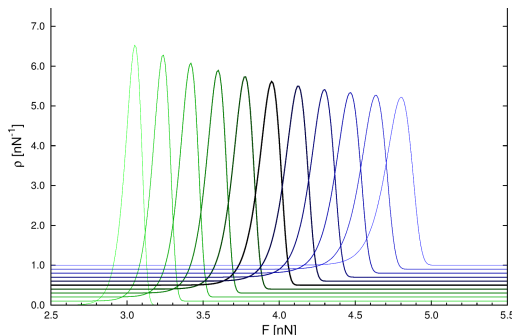


FIGURE 4.8: The effect of a change in the maximum force within a 25% range above (blue) and below (green) $F_{max}=7.2$ nN on C-N bond breakage. A Morse potential with $D_e = 340$ kJ/mol is assumed, and Arrhenius kinetics are applied under the conditions of 300K and loading rate 10 nN/s. The solid black lines correspond to $F_{max}=7.2$ nN kJ/mol.

Beyer [60], some of which has been reproduced in this section. In order to test our application of the Arrhenius kinetics model with published results [64, 60], COGEF potentials for small molecules $H_3SiCH_2CH_3$, propane ($H_3CCH_2CH_3$), dimethyl ammonium (DMA, H_3CNHCH_3), and dimethyl ether (DME, H_3COHCH_3) were calculated using isostructural stretching methods. The distance between the furthest apart hydrogen atoms on either

end of the molecule was increased in steps of 0.1 Å. These molecules were used to get estimation of bond strengths between a carbon atom and another atom, namely silicon, carbon, nitrogen or oxygen. The relaxed configurations for these molecules are depicted in figure 4.9, and the data from the COGEF potentials is summarized in table 4.1. According to this table, the Si-C bond is the weakest of the four bonds with a maximum force of 4.78 nN.

The energy for each step on the potential energy surface was calculated using the Gaussian basis set approach to density functional theory as implemented in NWChem [23] using the B3LYP hybrid functional [41]. The Gaussian basis sets from the NWChem basis set library used were 6-311++g3df_3pd [65, 66, 67, 68] and dzp_dunning.[69, 70, 71] Dzp_dunning and 6-311++g3df_3pd correspond to the D95(*d,p*) and 6-311++G(3*gf*,3*pd*) basis sets available in Gaussian. The geometry of each step was calculated using the stepper energy minimization algorithm built into NWChem with an energy convergence tolerance of 10^{-8} Ha.

The dissociation energy is taken as the difference between the energy of the unstretched molecule and the sum of the energies of the resultant molecules, and the maximum force is the maximum slope of the COGEF potential calculated at each point by finding the first derivative of the quadratic fit of that point and its nearest neighbors on the COGEF potential. In order to get results for a single bond, the symmetry within propane, DMA and DME was broken by initially displacing each atom by different random numbers within 0.01 Å in any direction. My calculations for the small molecules compare well with literature values except for the C-O bond which had values quoted that were almost 100 kJ/mol higher than those in literature, see table 4.1.

Using the information in table 4.1 derived from the COGEf potential for each molecule, I assume that the Morse potential is a reasonable approximation for the bond, and use Arrhenius kinetics, described in section 2, to estimate probabilities and time con-

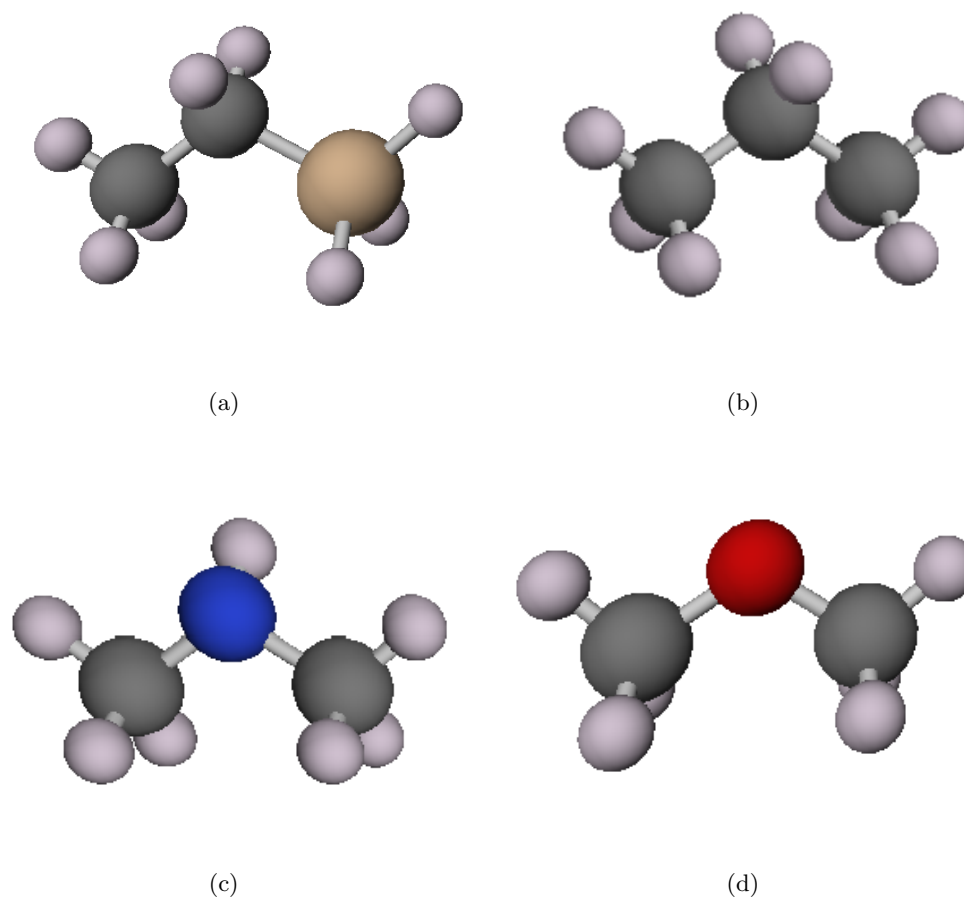


FIGURE 4.9: (a) $\text{H}_3\text{SiCH}_2\text{CH}_3$, (b) $\text{H}_3\text{SiCH}_2\text{CH}_3$ (propane), (c) H_3CNHCH_3 (dimethyl ammonium), (d) H_3CNHCH_3 (dimethyl ether)

stants, assuming a loading rate of 10nN/sec and $T=0^\circ\text{C}$. The details of these calculations are also discussed in detail in [60].

The graph on the left in figure 4.10 on is a picture of the model Morse potential and effective potential for dimethyl ammonium (DMA) when a constant force of 2.59 nN is applied to ends of the molecule. The horizontal line indicates the Dissociation energy. On the left of this same figure is a graph of the actual COGEF potential over which is overlaid the model Morse potential.

A much higher dissociation energy of 1800 kJ/mol is required to get the same

TABLE 4.1: Table of dissociation energies and maximum forces extracted from COGEF potentials of four test molecules. The second column indicates which bond broke in each molecule. The last two columns of this table are published values calculated using the program Gaussian with basis set D95(*d,p*) [60]. The reaction coordinate of each molecule is the distance between the two farthest spaced hydrogen atoms in the molecule.

Molecule	Bond	Basis Set	NWChem calculation		Literature [60]	
			D_e (kJ/mol)	F_{max} (nN)	D_e (kJ/mol)	F_{max} (nN)
<chem>H3SiCH2CH3</chem>	Si-C	dzp_dunning	341.82	4.85	337.4	4.78
	Si-C	6-311++g3df.3pd	337.69	4.81		
<chem>H3CCH2CH3</chem>	C-C	6-31G	379.48	6.89	370.8	6.92
	C-C	dzp_dunning	370.73	6.89		
	C-C	6-311++g3df.3pd	368.44	6.83		
<chem>H3CNHCH3</chem>	C-N	dzp_dunning	338.97	7.24	338.9	7.24
	C-N	6-311++g3df.3pd	337.69	7.23		
<chem>H3COHCH3</chem>	C-O	dzp_dunning	428.47	7.46	344.5	7.56
	C-O	6-311++g3df.3pd	428.95	7.49		

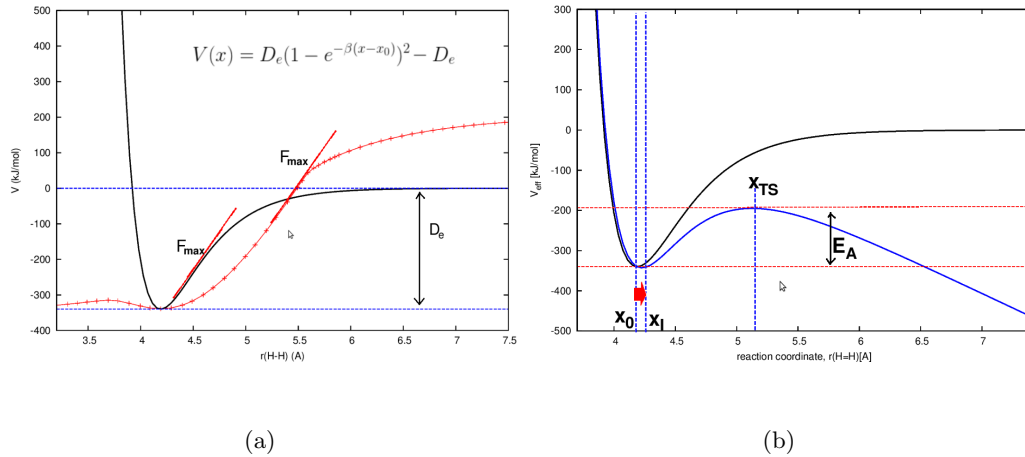


FIGURE 4.10: (a) COGEF potential for dimethyl ammonium overlaid with a Morse potential with the same dissociation energy (340 kJ/mol) and maximum slope (7.24 nN) for comparison. (b) Morse potential of (a) for DMA and its effective potential when a constant force of 2.59 nN is applied. The minimum (x_I) on the reaction coordinate shifts when a force is applied.

maximum slope at the same position as the COGEF potential, see figure 4.11.

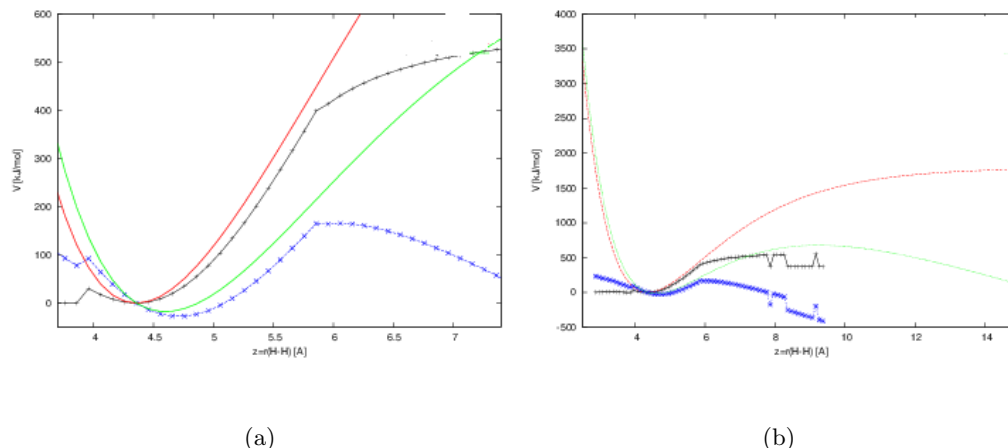


FIGURE 4.11: COGEF potential (black) and effective potential (blue) of dimethyl ammonium over which a Morse potential (red) and its effective potential (green) with dissociation energy of 1800 kJ/mol is laid for comparison. The maximum force of Morse potential is the same as that of the COGEF potential. A constant force of 2.59 nN is applied to the effective potentials as in figure 4.10. (b) is a wider perspective of (a) in order to compare the two D_e values.

By fixing the minimum point and the dissociation energy, as well as the maximum slope of the COGEF potential, i.e. maximum force, we can approximate the probabilities of the bonds in the table above with respect to the stretching force applied. The relationship between the lifetime of a bond and the applied force can also be approximated, see figure 4.12(b). It is notable in figure 4.12(c), that for two bonds C-C and C-N which have bond strengths that are very close to each other, that the C-N bond that has a higher F_{max} may be more likely to break first when higher loading rates are applied, see figures 4.12(b) and 4.12(c).

3.1 Curve crossing

When a sigma bond in a molecule breaks, the overall spin of the system will change. While the molecule is not yet broken, the singlet state will be the lowest energy configuration. However, once the molecule has split into two radicals, the lowest energy

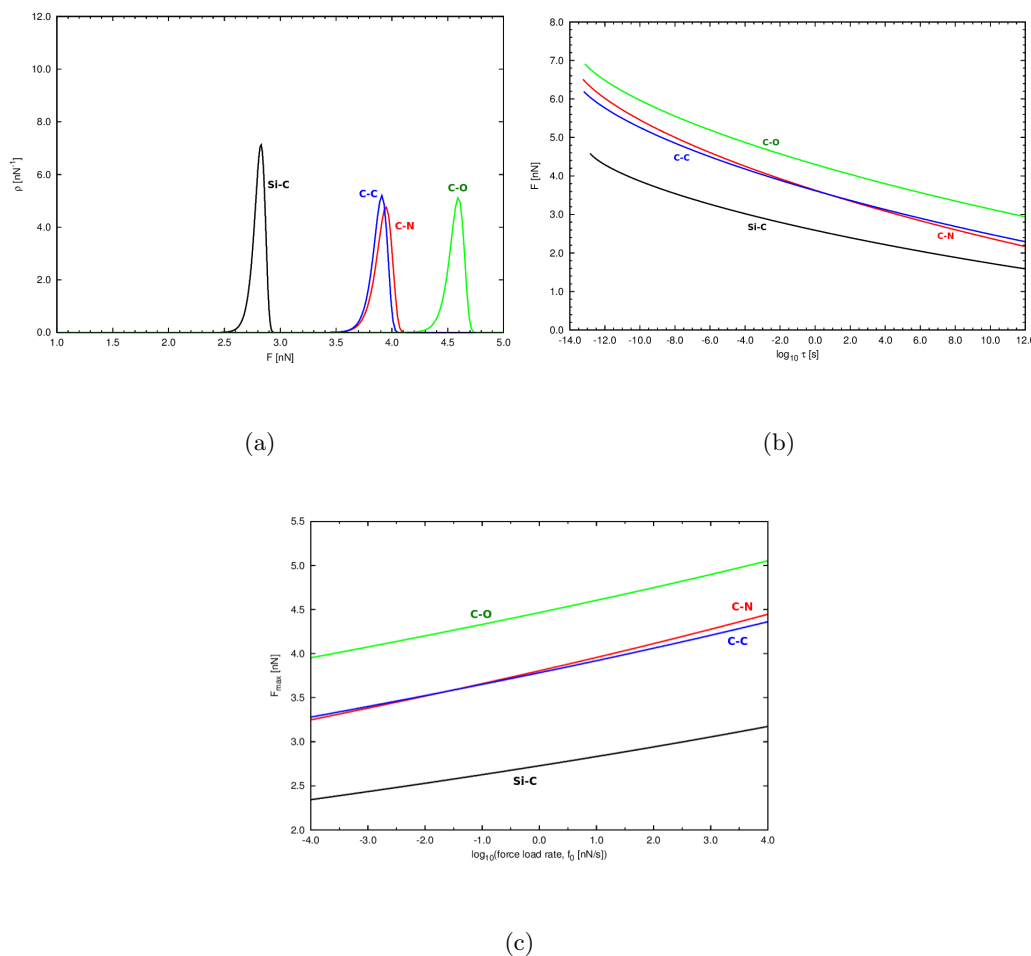


FIGURE 4.12: (a) Probability vs applied force and (b) force vs $\log_{10}(\tau)$ and (c) bond strength (i.e. force at which the bond is most likely to break) vs loading rate for the small molecules considered in table 4.1. The loading rate is set at 10 nN/s and the Arrhenius model was used calculate this data. The temperature was set to 300 K.

configuration will correspond to two separate radical that have the same spin, and thus the system will be in a triplet state (spin=1). For a small molecules, when the reaction coordinate is longer than the transition state distance, the output of NWChem jumps between the singlet and triplet value for the two molecule configuration of the products. An example of this is shown in figure 4.13 for the COGEF potentials of SiC₂H₈ and propane. By taking the output structures from the COGEF potential steps and forcing the spin

to be 1, in other words there are two more occupied α (spin-up) levels than occupied β (spin-down) energy levels, we can see in figure 4.14 that the tripe curve crosses after the maximum force occurs on the singlet curve.

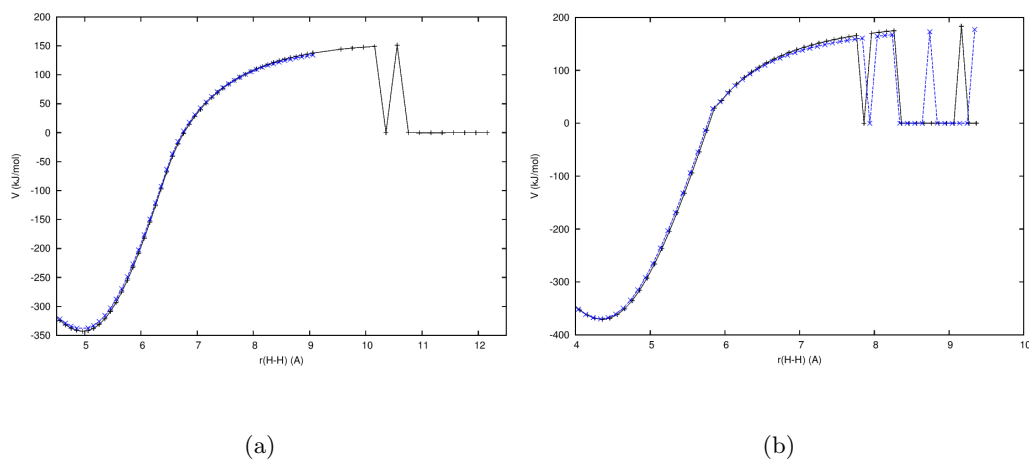


FIGURE 4.13: COGEF potentials of (a) SiC2H8 and (b) propane for longer ranges of the reaction coordinates. The NWChem calculations for longer ranges jump between the singlet and triplet state for the two molecule product. Results using Gaussian basis sets dzp_dunning (black) and 6-311++g3df_3pd (blue) are shown.

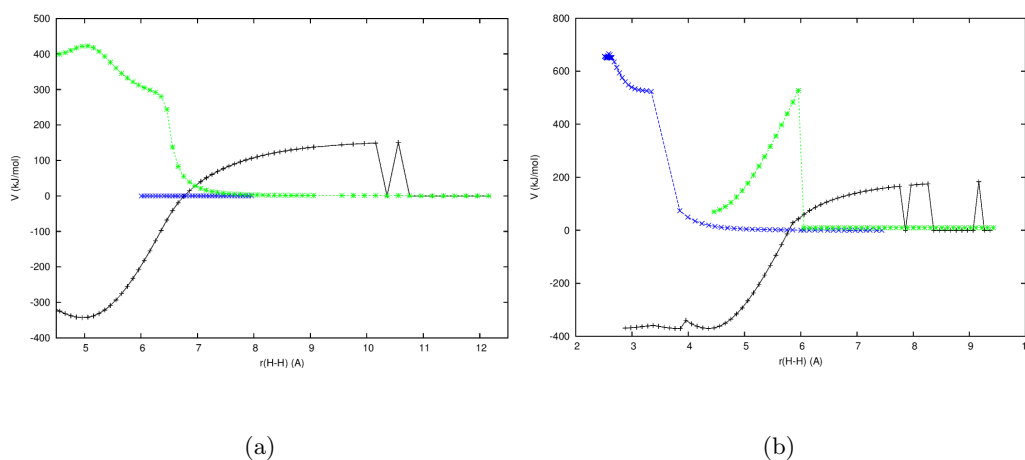


FIGURE 4.14: COGEF potentials of (a) SiC₂H₈ and (b) propane where the singlet state is specified in the NWChem input files (black), where the triplet state energy is calculated from each optimized singlet step (blue), and where the initial relaxed state (singlet) is stretched, but with triplet state specified (green). The singlet and triplet curve crossings occur just after the maximum force (circled in red on the graphs). The Gaussian basis set dzp_dunning was used in all these calculations.

4 Mechanocatalyst, C₁₈H₂₅N₃OS

Development of mechanocatalyst is a young discipline and paves the way toward self-healing materials. *N*-heterocyclic carbene (NHC), highlighted in figure 4.16(b), is a good catalyst for transesterification reactions where an organic group on an alcohol is exchanged with one on an ester. A latent, metal free catalyst can be made where the *N*-heterocyclic carbene is combined with an organic molecule with an isothiocyanate group, pictured in red in figure 4.15. This NHC-isothiocyanate is stable up to 70-80°C. In order for the catalyst to be activated, the C-C bond indicated in figure 4.16(a) has to break. Force probe atomic force microscopy (AFM) experiments have been performed on this molecule to test whether the correct bond will break when a mechanical force is applied to the ends of the molecule. The molecule is slowly stretched with a force loading rate of approximately 1 nN/s between a surface and an amine functionalized AFM cantilever,

to which the ends of the molecule are covalently bonded. The typical rupture force, the force at which the most bond breaking events occur, for the NHC-isocyanate adduct is 0.69 ± 0.56 nN. Control experiments, the green and yellow molecules and data in figure 4.15, were also performed to experimentally exclude bond rupture events that might occur within the di-isothiocyanate, the glycol linker and the thiourea pick-up bond.[26]

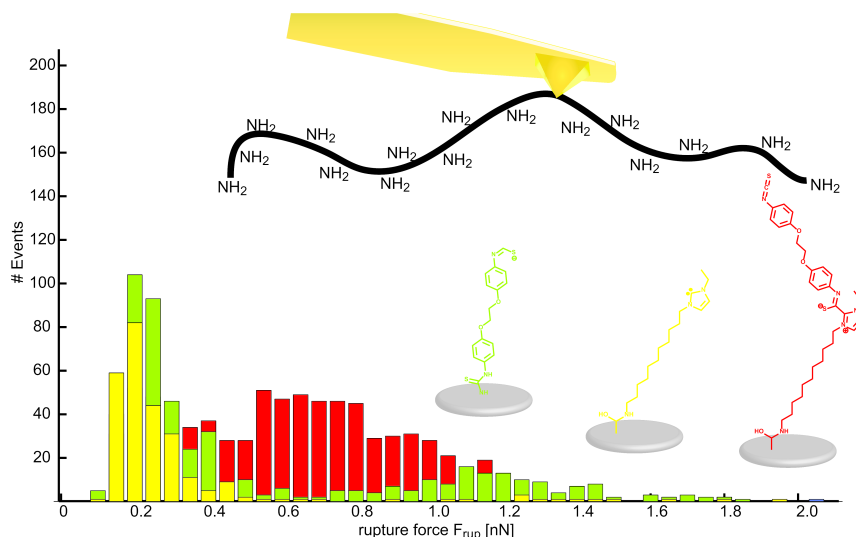


FIGURE 4.15: Results from AFM experiments performed by Monique Jacobs [26]. The central part of the red molecule is the focus of this section. The multiple peaks in the number of events with respect to applied force indicates that at least two different bonds broke. The force loading rates recorded for these experiments were on the order of 0.1 nN/s. Used with permission.

In order to verify the experimental results, I used an isostructural approach to theoretically examine the bonds within a section of the larger mechanocatalyst, pictured in figure 4.16. Figure 4.17 associates each atom in this smaller molecule with a number in order to reference the bonds within the molecule more easily. In order for the catalyst to activate, the C16-C17 bond needs to break.

4.1 Theoretical calculations and tests

Each density functional theory (DFT) calculation was performed in NWChem [23] used the B3LYP hybrid functional [41] and either the 321G [72, 73], 631G basis set[42], or

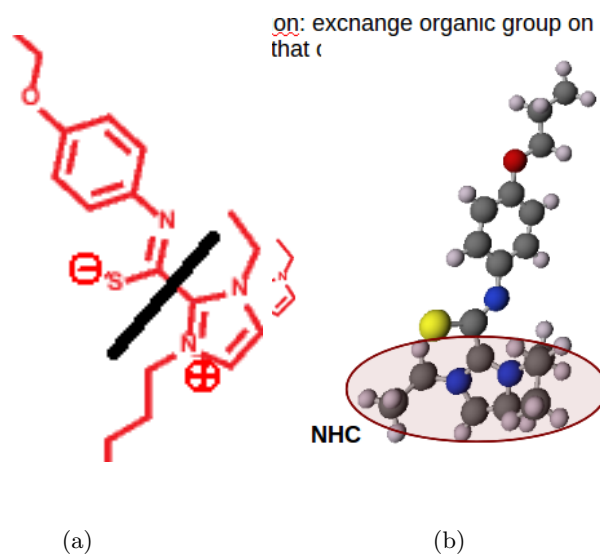


FIGURE 4.16: (a) Closer picture of the relevant section of the mechanocatalyst in figure 4.15. The black line indicates where the molecule needs to break in order to activate the catalyst. (b) Diagram of the NHC-NCS molecule with the catalyst, *N*-heterocyclic carbene, highlighted.

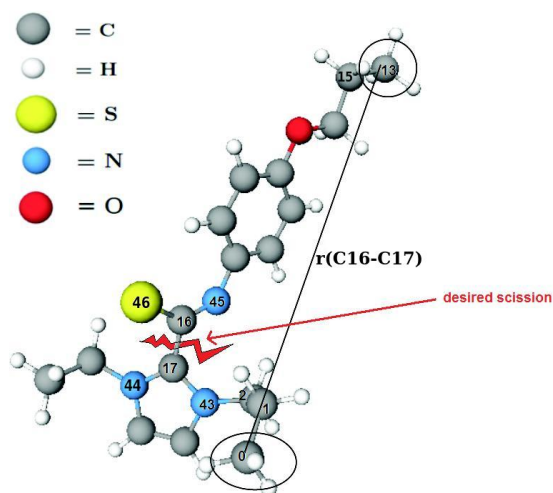


FIGURE 4.17: The $\text{C}_{18}\text{H}_{25}\text{N}_3\text{OS}$ molecule in its unstretched state. The numbers overlaid on the atoms are for referencing different bonds and anchor atoms. The line labeled $z=r(\text{C0-C13})$ indicates the reaction coordinate described as the distance between carbon atoms C0 and C13. Increasing this distance stepwise, produces a desired scission.

dzp-dunning[69, 70, 71] basis sets. In the geometry optimization of the following calculations, both of the built-in optimization methods in NWChem were utilized, but primarily the stepper method which uses an Eckart algorithm to find the minimum energy. The driver method uses quasi-newton optimization. The final energy conversion tolerance used in each stepper optimization calculation was 10^{-8} Ha. When the molecule was stretched by an amount dx along the reaction coordinate, this stretch was spread evenly over all the molecules with respect to the reaction coordinate in such a manner that the total volume of the molecule is preserved. In other words, any positive stretch along the reaction coordinate was accompanied molecules being moved closer to the reaction coordinate, perpendicular to the reaction coordinate.^f

In all cases, the dissociation energy is defined as the difference between the product molecules (in their optimal geometry) and the fully relaxed reactant molecule. It is assumed that each bond has a Morse potential, curve, and that the distortion of the COGEF potential curve from this shape can be attributed to all the other bonds that are stretched. The gradient of the potential is calculated using a first order, finite difference formula.

In order to remain within the limits of our computational capabilities and to reduce computation time, we will concentrate our analysis on the middle part of the full mechanocatalyst pictured on the right in figure 4.15, $C_{18}H_{25}N_3OS$ (NHC-NCS).

Optimization of the relaxed molecule

As a starting point, the optimal geometries of the relaxed and resultant molecules is required in order to calculate the dissociation energy for the event of a bond rupture. Due to the many dimensions in these molecules, particularly in the manner in which the molecules can rotate about their bonds, there is always a possibility that the optimization within NWChem will stop at a local minimum on the potential energy surface as opposed

^fAs dx is made smaller, the manner in which the molecule is stretched before being optimized should not matter.

to the true minimum. It is also possible that, if the energy difference between these two geometries is low, that both geometries might occur in an experimental situation. For the reactant molecule, NHC-NCS, it became evident that the first optimized geometry calculated using the built in methods in NWChem was not at the true minimum. From this first geometry, the optimized molecule was stretched and a jump in the COGEF potential was observed before any bonds in molecule were broken. Any step should be reversible due since these are adiabatic calculations, so the molecule was compressed in a step-wise fashion from the point of this energy jump. In this manner, a new minimum energy geometry was found with energy 0.4 eV lower. This same lower energy geometry can be found through optimization in NWChem if we start with a slightly different initial guess for the structure. The main difference between these geometries is the different torsion angle α (defined by atoms S46, C16, C17 and N44) between the NCS and NHC part of the molecule. In all further calculations, the relaxed geometry used will be that associated with the lowest energy (figure 4.18(a)). Both geometries and their DFT free energies are shown in figure 4.18. For both relaxed geometries, the adiabatic energy pathways converge before the bond breaks, see figure 4.19.

4.2 Adiabatic bond scission: desired bond

Applying the method described in section 4.1, the $\text{C}_{18}\text{H}_{25}\text{N}_3\text{OS}$ molecule is stretched with respect to the reaction coordinate, which is defined by atoms C0 and C13. The data extracted from the COGEF potential for different step spacings and basis sets is recorded in tables 4.2 and 4.3. Different basis sets yield different energies and maximum forces, from which we can estimate the uncertainty in our calculations. However, though the dissociation energies have about a 20% range, the maximum force does not change above a few percent. The uncertainty of the dissociation energies will mean that the calculations for the maximum force will have an uncertainty of about 1nN, see section 2.2 and figure 4.8.^g

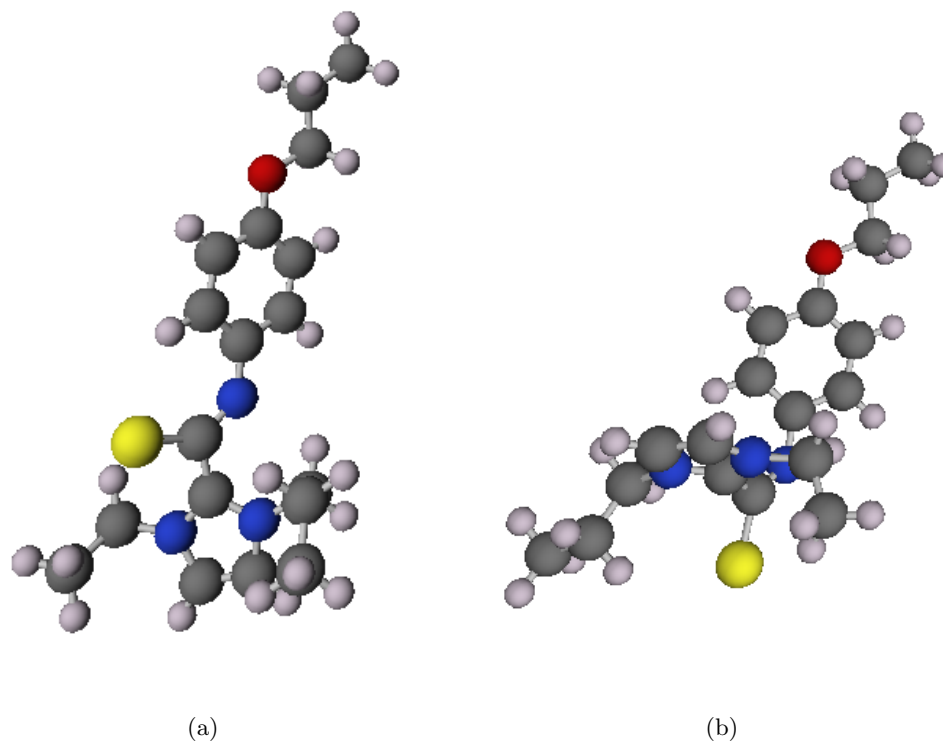


FIGURE 4.18: Representation of two relaxed structures of NHC-NCS. The lowest energy structure (a) has free energy -1338.348 Ha and torsion angle 58.8° , and another geometry that appears to be a local minimum (b) with free energy -1338.333 Ha and torsion angle 104.1° . Most of the NCS part of the molecule is in a plane, and the torsion angle is defined by atoms S46, C16, C17 and N44 (see figure 4.17 for atom numbers). The free energies are those calculated with the 6-31G basis set.

The initial reaction coordinate chosen is defined by atoms C0 and C13, the two atoms in the molecule which will certainly be stretched in the bigger molecule. The COGEF potential shown in figure 4.20 has step size 0.1 \AA , and is overlaid with the slope of that potential, which corresponds to the applied force. The maximum applied force occurs just before the bond scission event.

The fit of the Morse potential to the calculated COGEF potential is not as good which is to be expected because more bonds than one bond is stretched when an external force is applied.

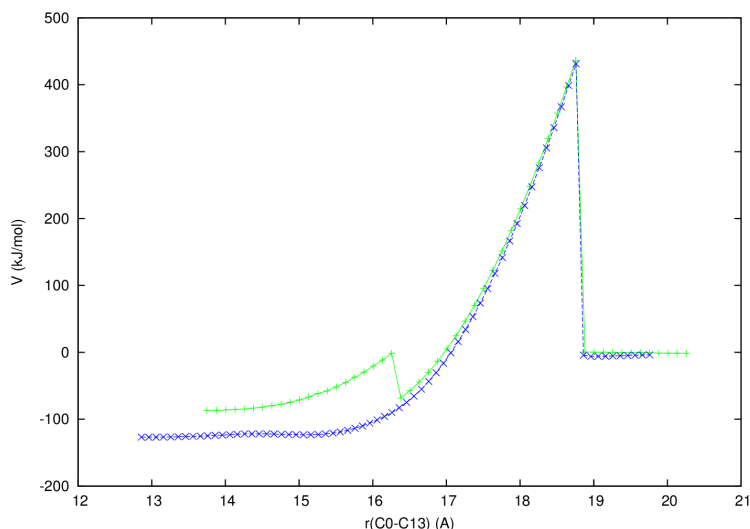


FIGURE 4.19: COGEF potential for the NHC-NCS molecule with reaction coordinate C0-C13. The 6-31G basis set has been used in each step. The blue line is the COGEF potential of the lowest energy starting structure, figure 4.18(a), and the green line corresponds to figure 4.18(b) at step 0. From the graph it is evident that that both COGEF potentials merge before the C16-C17 bond breaks. The steps progress by stretching the molecule in increments of 0.1 Å.

TABLE 4.2: Table of data extracted from COGEF potentials of $C_{18}H_{25}N_3OS$. The reaction coordinate (x) is the distance between two carbon atoms at the extremities of the molecule indicated in figure 4.17.

Basis Set	D_e (kJ/mol)	x_e (Å)	F_{max} (nN)	x_{max} (Å)	δx (Å)
3-21G	118.15	12.64	4.78	18.4	0.13
6-31G	126.95	12.85	5.38	18.75	0.1
dzp_dunning	91.61	12.75	5.10	18.36	0.1

For the desired scission, the anchor atoms of the reaction coordinate are chosen to be carbon atoms at opposite ends of the molecule C13 and C0. In order to get an idea of the strength of different bonds in this molecule, we choose different anchor atoms. With these new calculations, basis set 3-21G has been used so far. All the data in table 4.4 was calculated using the 3-21G basis set.

TABLE 4.3: Table of data maximum force extracted from COGEF potentials of $C_{18}H_{25}N_3OS$, where the step size is varied. The reaction coordinate is defined as the distance between two carbon atoms at the extremities of the molecule indicated in figure 4.17, and the 6-31G basis set has been used.

Step size	F_{max} (nN)	F_{max} - curve fit
0.13	118.15	
0.1		
dzp_dunning		0.1

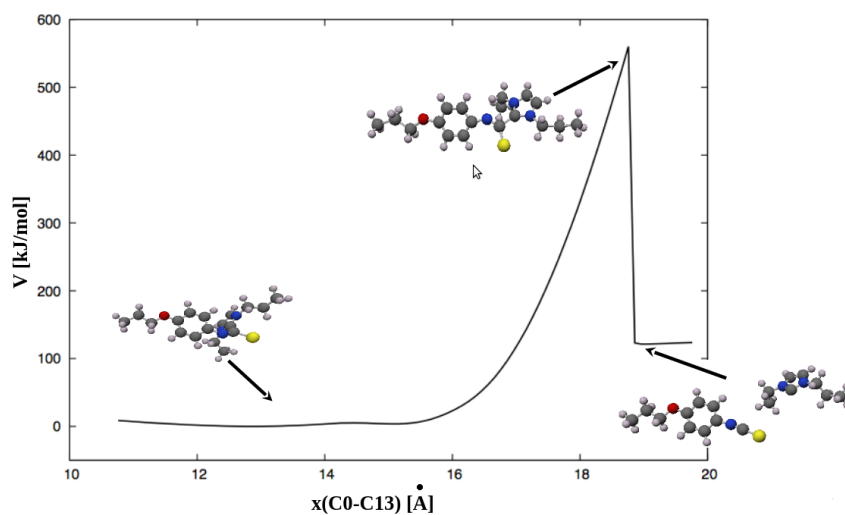


FIGURE 4.20: COGEF potential for $C_{18}H_{25}N_3OS$. Atoms C0 and C13 (see figure 4.17) are the anchor atoms defining the reaction coordinate. Stretching along this reaction coordinate produces a desired scission between atoms C16 and C17 as indicated in figure 4.17.

4.3 Calculations for different bond breakage

Experimentally, the C16-C17 bond is not the only bond that might break during each molecule stretch. Other bonds are expected to break since there are multiple peaks in a graph of the number of rupture events with respect to applied force. (Molecular vibrations that involve displacement perpendicular to the reaction coordinate C0-C13 may increase the probability that these different bonds breaks.) are transverse to the See figure 4.15.

TABLE 4.4: Table of data extracted from COGEF potentials of $C_{18}H_{25}N_3OS$. The reaction coordinate (z) is the distance between two carbon atoms at the extremities of the molecule indicated in figure 4.17. The 3-21G Gaussian basis set was used in these calculations.

Anchor atoms	Bond Broken	D_e (kJ/mol)	F_{max} (nN)
C0, C13	C16-C17 (desired scission)	118.19	4.79
C13, C17	C16-C17 (desired scission)	118.19	5.28
C0, C17	C0-C1 (undesired scission)	402.58	6.04
C0, N45	C0-C1 (undesired scission)	402.58	5.95
C1, C17	C1-C2 (undesired scission)	377.97	5.85
C13, C16	C13-C15 (undesired scission)	411.68	6.18
C2, N43	C2-N43 (undesired scission)	417.27	5.45

4.4 Molecular dynamics: different energy pathways

During adiabatic stretching of the $C_{18}H_{25}N_3OS$ molecule, the N-heterocyclic carbene (NHC) is rotated about the C16-C17 bond (see figure 4.17) and the energy of the molecules is expected to take the lowest energy path. However, this might not necessarily be the shortest path, and when force loading rates and thermal excitations are taken into account, the molecule energetic pathway might be very different from the adiabatic path. For a given molecule and reaction coordinate, the *ab-initio* density functional theory calculations are only going to yield one possible energetic pathway for the bond-breaking reaction. Over longer time scales, which are associated with low force loading rates and AFM experiments, the probability that the reaction will follow the adiabatic pathway on the potential energy surface becomes more likely. For higher loading rates and shorter time-scales, such as is found in ultrasound experiments, molecular dynamic calculations would give a better approximation for which bond will break and when it will break. However, changes to the constraints forced onto the molecule during optimization can yield different results which give approximate values for the nonadiabatic pathways,

which include different bonds breaking, or less 'unwinding' of the molecule.

Taking torsion angle and bond angles into consideration

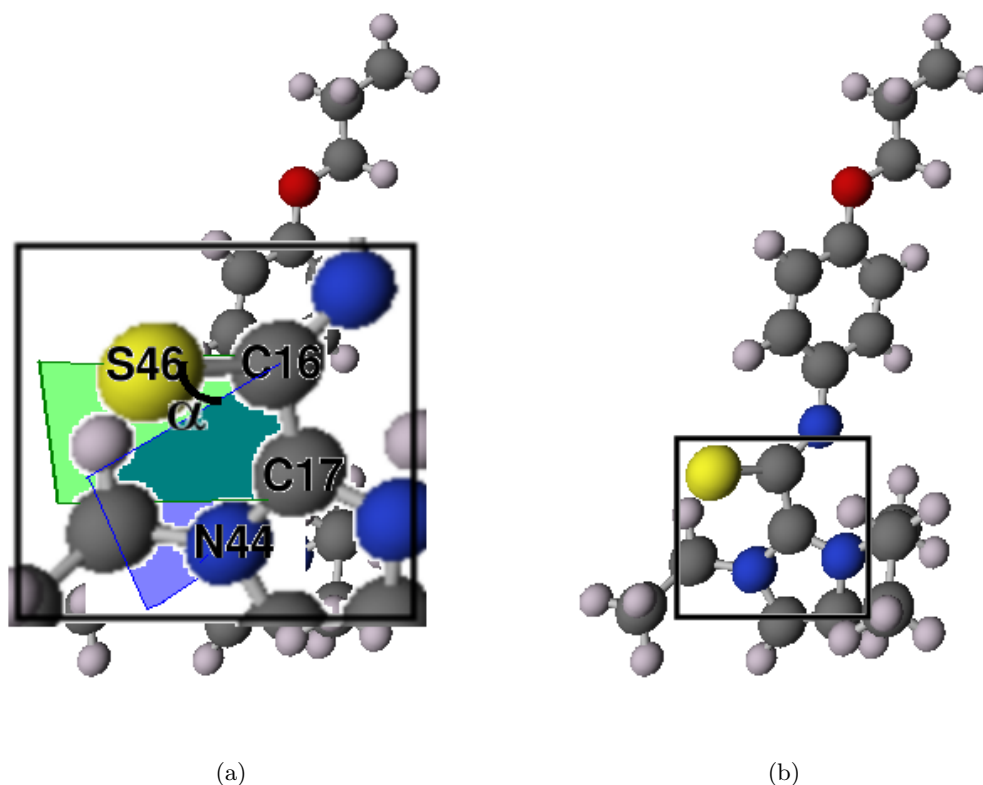


FIGURE 4.21: (a) Diagram of the the torsion angle defined by the S46-C16-C17-N44 bond. This torsion angle increases as the molecule is stretched. (b) shows the context in the molecule of the magnified section in (a).

In the calculations with the 6-31G basis set, the torsion angle between the sulfur atom (S46), the two carbon atoms (C16 and C17), and the nitrogen atom N44, see figure 4.21, rotates through 106 degrees before breaking. This is illustrated in figure 4.22. If the molecule has enough time, the very act of stretching the molecule will unwind it. This is evident in 4.22 by how the initial angle for each step does not differ significantly from the final optimized torsion angle. The initial angle is a result of merely lengthening all the bonds in the direction of the reaction coordinate. On short time scales (which correspond

to higher applied forces), it would be expected that the molecule does not have enough time to 'unwind.' Since the NHC-NCS molecule is a zwitterionic molecule, attractive electrostatic interaction between the S46 and N44 atoms may affect the force required to break the C16-C17 bond on short time scales on the order of picoseconds, which are more typical of bond breaking events in mechanical force experiments using ultrasound. If, during stretching, the torsion angle is artificially constrained to not rotate, we might be able to get some idea of the time and force required to break the bond when higher forces are applied without using molecular dynamics equations. The calculated COGEF potential force required to break the C16-C17 is expected to be higher due to electrostatic attraction between S46 and N44. Upon application to the Arrhenius model, this higher force may mean that other bonds breaking become more probable. This is confirmed by molecular dynamics circulations.[26] Attempts to constrain the torsion angle defined by the S46-C16-C17-N44 bonds by rotating the the molecule back to the original torsion angle before optimizing each step, and constraints to fix the torsion angle during optimization in NWChem have not yet been successful, and this is an area for future investigation.

Molecular dynamics calculations comparison

Molecular dynamics simulations have been calculated for this molecule, and the details of the calculations are discussed fully in [26]. The bond breakage for different constant applied pulling forces at the C0,C13 atoms have been examined. There were three force ranges of interest:

1. A range of forces (below 4nN) for which the molecule rotates about the torsion angle discussed in section 4.4 but equilibrates without breaking because the force is not high enough to break the C16-C17 bond
2. A range of forces where the molecule rotates about the C16-C17 bond before breaking at that bond

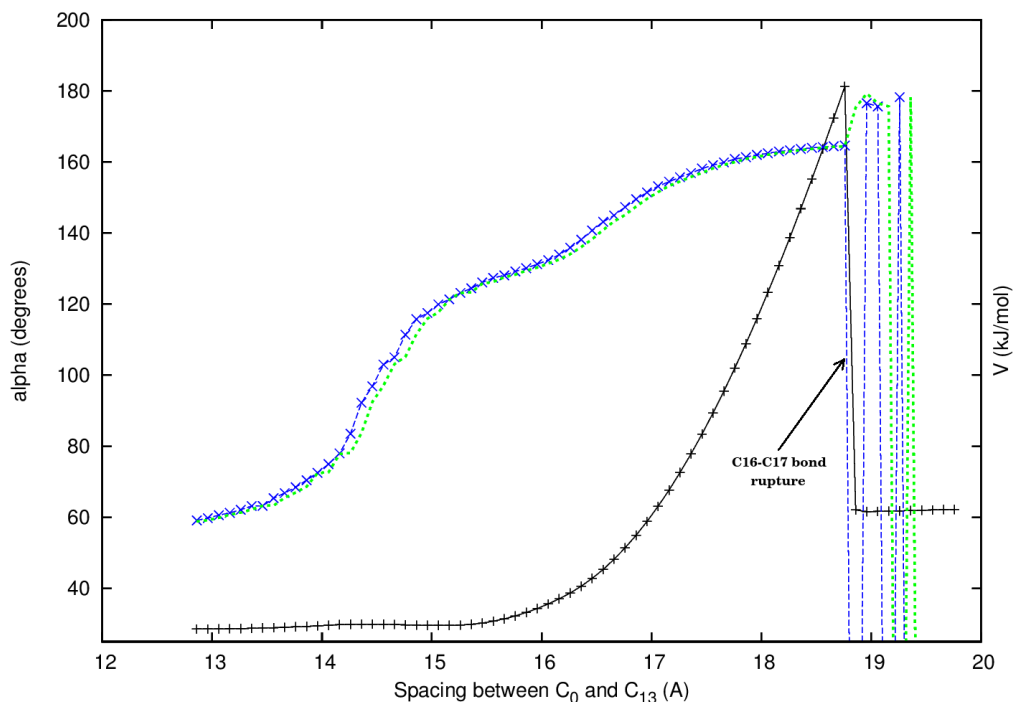


FIGURE 4.22: Torsion angle (left scale) versus reaction coordinate C0-C13, overlaid with COGEF potential (right scale, black). The torsion angle is defined as counterclockwise rotation about the C16-C17, where atoms S46, C16, C17 and N44 fully define the torsion. The blue line is the torsion angle after each step has been optimized, and the green is the torsion angle after the stretch for each step, but before optimization. This plot shows that the molecule can be considered as two parts joined by the C16-C17 bond. The parts rotate with respect to each other as the molecule is stretched. The 6-31G basis set was used in the COGEF potential calculation.

3. A range of forces for which the molecule does not have sufficient time to rotate, and the C16-C17 breaks without being preceded by a rotation about the C16-C17 axis
4. Higher forces (10nN) at which different bonds break, such as

From these calculations we might conclude that at higher loading rates, which correspond to less time, there is a higher likelihood of undesired bonds breaking within the molecule. It may be useful to consider the activation energy on the COGEF potential, as well as the potential energy surface of the pathways taken in the MD simulations in order to extracting this information using density functional theory and Arrhenius kinetics.

4.5 Theoretical results

Fit to Arrhenius model

All calculations below are based on the theory discussed by Beyer in [60] and section 2.2. The probability and time constant calculations below are calculated using the dissociation energy (De) and maximum force F_{max} extracted from COGEF potentials for the NHC-NCS molecule with different constraints applied. As described in section 4.1, for each bond we assume a Morse potential with the same dissociation energy and maximum force from the COGEF potentials to calculate lifetime and probabilities of bond-breaking with respect to force. These are shown in figure 4.23 below. According to the graphs below, the desired scission is expected to have a very short lifetime and is bond that is most likely to break for all force loading rates used in AFM experiments. For 1 nN/s force loading rate at room temperature, the bond strength of the C16-C17 (desired) bond is determined to be at 0.49 nN,[§] see figure 4.23(a), with the 3-21G basis set, which agrees well with the experimental results. The lines in figures 4.23(b) and 4.23(c) appear to converge at higher force loading rates and shorter lifetimes. When these lines converge and cross, we expect to see bonds other than the desired scission breaking as well. These rates and times are near the limits of what the Morse potential model in Arrhenius kinetics can reasonably predict, so at what force loading rates the lines will converge cannot be accurately predicted from these graphs.

[§]The bond strengths determined by the higher order basis sets for the (6-31G and dzp_dunning) are much closer to zero. Improvements on the approximation for the frequency factor in the Arrhenius equation may improve these results, and checks using the experimental controls in figure 4.15 should also agree well with experiment at the 3-21G level.

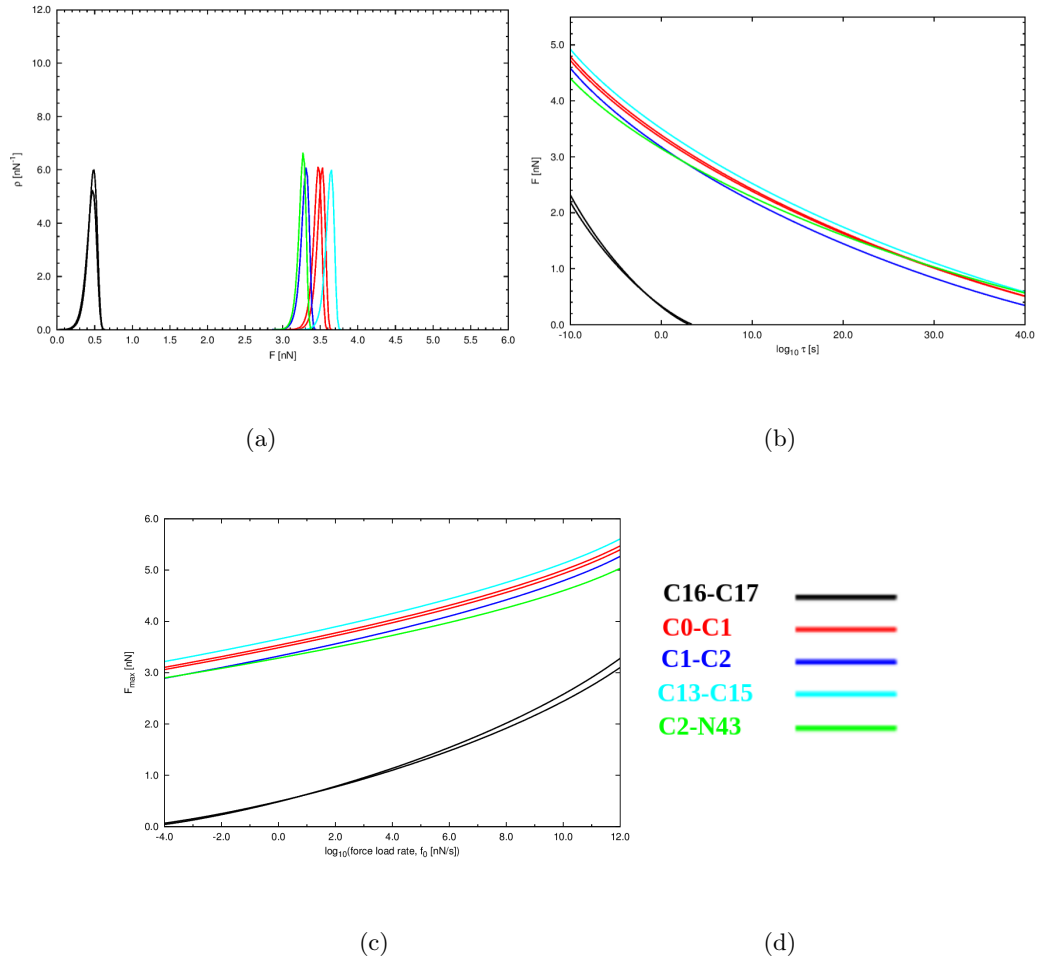


FIGURE 4.23: (a) Probability vs applied force and (b) force vs $\log_{10}(\tau)$ and (c) bond strength (i.e. force at which the most bonds break) vs loading rate for reaction coordinates of $\text{C}_{18}\text{H}_{25}\text{N}_3\text{OS}$ considered in table 4.4. The loading rate is set at 1 nN/s and the Arrhenius model was used calculate this data. The temperature was set to 300 K. (d) is the color key for these graphs. Each color corresponds to a specific bond that broke when the molecule was stretched. Multiple lines of the same color correspond to the same bonds breaking when different anchor atoms are chosen. There is not significant variation in these lines within the limits of the Morse potential model.

5 Summary and future research

The isostructural approach to using density functional theory to analyze covalent bonds has thus far agreed well with experiment. Theoretical results indicate that the C16-

C17 bond is the bond that is most likely to rupture in AFM experiments. The validity of these results could be confirmed by comparing theoretical and experimental results for the controls in figure 4.15. Improvements on the approximations used for frequency factor such as taking into account the bond angles with respect to the reaction coordinate, torsion angles within the molecule, and treating rings and other structures that not stretched while the molecule is stretched along a given reaction coordinate as single units of higher mass in the molecule are areas for future research. It would also be interesting to consider the electrostatic and viscosity effects of the surrounding solution on the molecule during mechanical bond-breaking, such as possibly implementing the application of the COSMO ("COnductor-like Screening MOdel") solvation model available in NWChem.

6 Acknowledgements

I would like to thank Monique Jacobs for our discussions on this subject, particularly for providing an experimental perspective to the topic.

5 SUMMARY

I have performed density functional theory calculations for electronic and optical properties of anthradithiophene and indenofluorene derivatives. These two sets of molecules have similar molecular and crystal structures. Because of the weaker intermolecular bonding in organic crystals, due van der Waals interactions, and not covalent or ionic bonding, localization effects due to charge carriers in the crystals are high and charge carriers are less likely to be delocalized over the lattice. Furthermore, compared to inorganic crystals, band like transport more complicated because charge carriers in organic crystals tend to have strong interactions with molecular and lattice vibrations. Regardless, calculating the effective masses and eigenvectors for these organic crystals provides important estimates of the directions where the electronic coupling between molecules is strongest in the lattice. This degree of intermolecular coupling is important in both band (coherent) and hopping (incoherent) charge transport. Functionalizing the molecules with bulky side groups such as triisopropylsilylethynyl tends to induce planar packing in the crystal, and the highest degree of molecular orbital overlap corresponded to a vector that pointed across the planes with a component along the backbone of the molecule. Analysis of the effective masses and band structure suggest that single crystal ADT-TES-F, IF-TES-F and IF-TES-Br will have observable and useful mobilities. Experimentally, observable photo-currents in ADT-TES-F [43] and a good hole mobility of $1.0 \text{ cm}^2/\text{Vs}$ for ADT-TES [28] has been recorded.

Ab-initio density functional theory calculations in NWChem and VASP are used to calculate effective masses, ionization potentials, electron affinities and reorganization energies. End-group functionalization can be used to shift the relative alignment of the HOMO and LUMO levels of molecules. The similar geometry of the different derivatives of a molecule such as anthradithiophene means that bulk heterojunctions can be formed

without adversely affecting the crystal structure. Doping a *p*-type crystal or film to create type II bulk heterojunction enables tuning of the conductivity in the crystal. If the dopant molecules have a similar crystal and molecular structure to the molecules in the pristine film, doping will not adversely disrupt the electronic properties of the crystal that are due to molecular packing. IF-TIPS-F has a very similar crystal structure and molecular arrangement compared to ADT-TES-F, and it can act as an electron acceptor to ADT-TES-F due to the relative alignment of the HOMO and LUMO levels. Consequently, IF-TIPS-F is a good candidate with which to dope pristine ADT-TES-F in order to tune conductivity.

Not only do organic molecules have potential application in devices such as solar cells or field effect transistors, where charge transport and transfer across intra- and intermolecular bonds is essential, but also in molecular force sensors or mechanocatalysts where the covalent bond properties within a molecule are exploited. In mechanocatalysts, mechanical force is used to break bonds in the molecule to activate the catalyst. This has advantages over chemical or photo activation, where the solution in which the catalyst resides might be altered by the addition of a new chemical or photons. However, specific bonds need to be broken to activate a mechanocatalyst. Information about the covalent bonds within a molecule, their bond strengths, and the probability of bond rupture becomes essential in order to design such functional materials. In the context of low force loading rates, bond strengths and activation energies can be approximated from adiabatic, isotensional stretching of a molecule in a stepwise fashion, using density functional theory. Information is extracted from the potential energy surface along the reaction coordinate. The theoretical calculations presented in this thesis on a mechanocatalyst containing a N-heterocyclic carbene, C₁₈H₂₅N₃OS, agreed well with experiment, but there are many more avenues to explore to improve on these results.

BIBLIOGRAPHY

1. Edger A. Silinsh. Organic molecular crystals : interaction, localization, and transport phenomena. American Institute of Physics, New York, 1994.
2. Professor Dr Edgar A. Silinsh. Introduction: Characteristic features of organic molecular crystals. In Organic Molecular Crystals, number 16 in Springer Series in Solid-State Sciences, pages 1–46. Springer Berlin Heidelberg, January 1980.
3. J. H. Schn, Ch. Kloc, T. Siegrist, J. Laquindanum, and H. E. Katz. Charge transport in anthradithiophene single crystals. Organic Electronics, 2(3-4):165–169, 2001.
4. Joyce G. Laquindanum, Howard E. Katz, and Andrew J. Lovinger. Synthesis, morphology, and field-effect mobility of anthradithiophenes. Journal of the American Chemical Society, 120(4):664–672, February 1998.
5. Thorsten Vehoff, Bjorn Baumeier, Alessandro Troisi, and Denis Andrienko. Charge transport in organic crystals: Role of disorder and topological connectivity. Journal of the American Chemical Society, 132(33):11702–11708, 2010.
6. H. E. Katz and Z. Bao. The physical chemistry of organic field-effect transistors. The Journal of Physical Chemistry B, 104(4):671–678, February 2000.
7. H. E. Katz, W. Li, A. J. Lovinger, and J. Laquindanum. Solution-phase deposition of oligomeric TFT semiconductors. Synthetic Metals, 102(1-3):897–899, June 1999.
8. Howard E. Katz and Jia Huang. Thin-film organic electronic devices. Annual Review of Materials Research, 39(1):71–92, 2009.
9. Jordi Ribas-Arino and Dominik Marx. Covalent mechanochemistry: Theoretical concepts and computational tools with applications to molecular nanomechanics. Chemical Reviews, 112(10):5412–5487, October 2012.
10. O. Kwon, V. Coropceanu, N. E. Gruhn, J. C. Durivage, J. G. Laquindanum, H. E. Katz, J. Cornil, and J. L. Bredas. Characterization of the molecular parameters determining charge transport in anthradithiophene. The Journal of Chemical Physics, 120(17):8186, 2004.
11. J. L. Brdas, J. P. Calbert, D. A. da Silva Filho, and J. Cornil. Organic semiconductors: A theoretical characterization of the basic parameters governing charge transport. Proceedings of the National Academy of Sciences, 99(9):5804–5809, April 2002.
12. R. B Campbell, J. M Robertson, and J. Trotter. The crystal and molecular structure of pentacene. Acta Crystallographica, 14(7):705–711, July 1961.

13. John E. Anthony, James S. Brooks, David L. Eaton, and Sean R. Parkin. Functionalized pentacene: improved electronic properties from control of solid-state order. Journal of the American Chemical Society, 123(38):9482–9483, 2001.
14. John E. Anthony, David L. Eaton, and Sean R. Parkin. A road map to stable, soluble, easily crystallized pentacene derivatives. Organic Letters, 4(1):15–18, December 2001. ACS Publications.
15. Veaceslav Coropceanu, Jrme Cornil, Demetrio A. da Silva Filho, Yoann Olivier, Robert Silbey, and Jean-Luc Brdas. Charge transport in organic semiconductors. Chemical Reviews, 107(4):926–952, 2007.
16. Paul F. Barbara, Thomas J. Meyer, and Mark A. Ratner. Contemporary issues in electron transfer research. The Journal of Physical Chemistry, 100(31):13148–13168, January 1996.
17. R. A. Marcus. On the theory of OxidationReduction reactions involving electron transfer. i. The Journal of Chemical Physics, 24(5):966–978, May 1956.
18. Bruus, Henrik and Flensburg, Karsten. Many-Body Quantum Theory in Condense Matter Physics, an introduction. Oxford University Press, USA, 2004.
19. Neil W. Ashcroft and N. David Mermin. Solid State Physics. Brooks Cole, 1 edition, January 1976.
20. Martin Pope and Charles E. Swenberg. Electronic processes in organic crystals and polymers. Oxford University Press, 1982.
21. Gary Black, Karen Schuchardt, Debbie Gracio, and Bruce Palmer. The extensible computational chemistry environment: A problem solving environment for high performance theoretical chemistry. In Peter M. A. Sloot, David Abramson, Alexander V. Bogdanov, Yuriy E. Gorbachev, Jack J. Dongarra, and Albert Y. Zomaya, editors, Computational Science ICCS 2003, number 2660 in Lecture Notes in Computer Science, pages 122–131. Springer Berlin Heidelberg, January 2003.
22. Whitney E. B. Shepherd, Andrew D. Platt, Mark J. Kendrick, Marsha A. Loth, John E. Anthony, and Oksana Ostroverkhova. Energy transfer and exciplex formation and their impact on exciton and charge carrier dynamics in organic films. The Journal of Physical Chemistry Letters, pages 362–366, 2011.
23. M. Valiev, E.J. Bylaska, N. Govind, K. Kowalski, T.P. Straatsma, H.J.J. Van Dam, D. Wang, J. Nieplocha, E. Apra, T.L. Windus, and W.A. de Jong. NWChem: a comprehensive and scalable open-source solution for large scale molecular simulations. Computer Physics Communications, 181(9):1477–1489, September 2010.

24. Johnathan N. Brantley, Kelly M. Wiggins, and Christopher W. Bielawski. Unclicking the click: Mechanically facilitated 1,3-dipolar cycloreversions. Science, 333(6049):1606–1609, September 2011.
25. Marjoke F. Debets, Sander S. van Berkel, Jan Dommerholt, A. (Ton) J. Dirks, Floris P. J. T. Rutjes, and Floris L. van Delft. Bioconjugation with strained alkenes and alkynes. Accounts of Chemical Research, 44(9):805–815, September 2011.
26. Monique Jacobs. single molecule mechano - (Bio)Chemistry. PhD thesis, Radboud Universiteit Nijmegen, Wesel, Duitsland, 2014.
27. Sankar Subramanian, Sung Kyu Park, Sean R. Parkin, Vitaly Podzorov, Thomas N. Jackson, and John E. Anthony. Chromophore fluorination enhances crystallization and stability of soluble anthradithiophene semiconductors. Journal of the American Chemical Society, 130(9):2706–2707, 2008.
28. Marcia M. Payne, Sean R. Parkin, John E. Anthony, Chung-Chen Kuo, and Thomas N. Jackson. Organic Field-Effect transistors from Solution-Deposited functionalized acenes with mobilities as high as 1 cm²/Vs. Journal of the American Chemical Society, 127(14):4986–4987, 2005.
29. S. F. Nelson, Y.-Y. Lin, D. J. Gundlach, and T. N. Jackson. Temperature-independent transport in high-mobility pentacene transistors. Applied Physics Letters, 72(15):1854, 1998.
30. Sung Kyu Park, Devin A. Mourey, Sankar Subramanian, John E. Anthony, and Thomas N. Jackson. High-mobility spin-cast organic thin film transistors. Applied Physics Letters, 93:043301, 2008.
31. P. E. Blöchl. Projector augmented-wave method. Physical Review B, 50(24):17953, 1994.
32. G. Kresse and D. Joubert. From ultrasoft pseudopotentials to the projector augmented-wave method. Phys. Rev. B, 59(3):1758–1775, Jan 1999.
33. G. Kresse and J. Hafner. Ab initio molecular dynamics for liquid metals. Physical Review B, 47(1):558, 1993.
34. G. Kresse and J. Hafner. Ab initio molecular-dynamics simulation of the liquid-metalamorphous-semiconductor transition in germanium. Physical Review B, 49(20):14251–14269, 1994.
35. G. Kresse and J. Furthmüller. Efficiency of ab-initio total energy calculations for metals and semiconductors using a plane-wave basis set. Computational Materials Science, 6:15–50, 1996.

36. G. Kresse and J. Furthmüller. Efficient iterative schemes for ab initio total-energy calculations using a plane-wave basis set. Physical Review B, 54(16):11169, 1996.
37. John P. Perdew, J. A. Chevary, S. H. Vosko, Koblar A. Jackson, Mark R. Pederson, D. J. Singh, and Carlos Fiolhais. Atoms, molecules, solids, and surfaces: Applications of the generalized gradient approximation for exchange and correlation. Physical Review B, 46(11):6671–6687, 1992.
38. John P. Perdew, J. A. Chevary, S. H. Vosko, Koblar A. Jackson, Mark R. Pederson, D. J. Singh, and Carlos Fiolhais. Erratum: Atoms, molecules, solids, and surfaces: Applications of the generalized gradient approximation for exchange and correlation. Physical Review B, 48(7):4978–4978, 1993.
39. Marcia M. Payne, Susan A. Odom, Sean R. Parkin, and J. E. Anthony. Stable, crystalline acenedithiophenes with up to seven linearly fused rings. Organic Letters, 6(19):3325 – 3328, 2004. Copyright 2004 American Chemical Society.
40. Stefan Grimme. Semiempirical GGAType density functional constructed with a long-range dispersion correction. Journal of Computational Chemistry, 27(15):1787–1799, November 2006.
41. Axel D. Becke. Densityfunctional thermochemistry. III. The role of exact exchange. The Journal of Chemical Physics, 98(7):5648–5652, 1993.
42. W. J. Hehre, R. Ditchfield, and J. A. Pople. SelfConsistent molecular orbital methods. XII. further extensions of GaussianType basis sets for use in molecular orbital studies of organic molecules. The Journal of Chemical Physics, 56(5):2257–2261, 1972.
43. Andrew D. Platt, Jonathan Day, Sankar Subramanian, John E. Anthony, and Oksana Ostroverkhova. Optical, fluorescent, and (Photo)conductive properties of High-Performance functionalized pentacene and anthradithiophene derivatives. J. Phys. Chem. C, 113(31):14006–14014, 2009.
44. Yuanping Yi, Lingyun Zhu, and Jean-Luc Brdas. Charge-transport parameters of acenedithiophene crystals: Realization of one-, two-, or three-dimensional transport channels through alkyl and phenyl derivatizations. The Journal of Physical Chemistry C, 116(8):5215–5224, March 2012.
45. Adrian P. Sutton. Electronic Structure of Materials. Oxford University Press, USA, November 1993.
46. Zhenan Bao and Andrew J. Lovinger. Soluble regioregular polythiophene derivatives as semiconducting materials for field-effect transistors. Chemistry of Materials, 11(9):2607–2612, September 1999.

47. John E. Anthony. Functionalized acenes and heteroacenes for organic electronics. Chemical Reviews, 106(12):5028–5048, December 2006.
48. Takeshi Kawase, Takeru Fujiwara, Chitoshi Kitamura, Akihito Konishi, Yasukazu Hirao, Kouzou Matsumoto, Hiroyuki Kurata, Takashi Kubo, Shoji Shinamura, Hiroki Mori, Eigo Miyazaki, and Kazuo Takimiya. Dinaphthopentalenes: Pentalene derivatives for organic thin-film transistors. Angewandte Chemie International Edition, 49(42):7728–7732, October 2010.
49. John E. Anthony, Sankar Subramanian, Sean R. Parkin, Sung Kyu Park, and Thomas N. Jackson. Thin-film morphology and transistor performance of alkyl-substituted triethylsilylethynyl anthradithiophenes. Journal of Materials Chemistry, 19(42):7984, 2009.
50. Klaus Hafner, Bernd Stowasser, Hans-Peter Krimmer, Stefanie Fischer, Michael C. Bhm, and Hans Jrg Lindner. Synthesis and properties of 1,3,5,7-tetra-tert-butyl-s-indacene. Angewandte Chemie International Edition in English, 25(7):630–632, July 1986.
51. A. Vollmer, H. Weiss, S. Rentenberger, I. Salzmann, J. P. Rabe, and N. Koch. The interaction of oxygen and ozone with pentacene. Surface Science, 600(18):4004–4007, September 2006.
52. Daniel T. Chase, Bradley D. Rose, Sean P. McClintock, Lev N. Zakharov, and Michael M. Haley. Indeno[1,2-b]fluorenes: Fully conjugated antiaromatic analogues of acenes. Angewandte Chemie International Edition, 50(5):1127–1130, February 2011.
53. Katsuhiko Ono, Hiroaki Totani, Takao Hiei, Akihiro Yoshino, Katsuhiro Saito, Katsuya Eguchi, Masaaki Tomura, Jun-ichi Nishida, and Yoshiro Yamashita. Photooxidation and reproduction of pentacene derivatives substituted by aromatic groups. Tetrahedron, 63(39):9699–9704, September 2007.
54. Whitney Shepherd, Oksana Ostraverkhova, Aaron Fix, and Micheal M. Hayley. cif files for indenofluorene derivatives. private communication, March.
55. John P. Perdew, Kieron Burke, and Matthias Ernzerhof. Generalized gradient approximation made simple. Physical Review Letters, 77(18):3865–3868, October 1996.
56. John P. Perdew, Kieron Burke, and Matthias Ernzerhof. Generalized gradient approximation made simple [phys. rev. lett. 77, 3865 (1996)]. Physical Review Letters, 78(7):1396–1396, February 1997.
57. M. J. Kendrick, A. Neunzert, M. M. Payne, B. Purushothaman, B. D. Rose, J. E. Anthony, M. M. Haley, and O. Ostroverkhova. Formation of the DonorAcceptor

- charge-transfer exciton and its contribution to charge photogeneration and recombination in small-molecule bulk heterojunctions. The Journal of Physical Chemistry C, 116(34):18108–18116, August 2012.
58. M. Bixon and Joshua Jortner. Electron transfer from isolated molecules to biomolecules. In I. Prigogine and Stuart A. Rice, editors, Advances in Chemical Physics, pages 35–202. John Wiley & Sons, Inc., 1999.
 59. Jordi Ribas-Arino, Motoyuki Shiga, and Dominik Marx. Understanding covalent mechanochemistry. Angewandte Chemie International Edition, 48(23):41904193, 2009.
 60. Martin K. Beyer. The mechanical strength of a covalent bond calculated by density functional theory. The Journal of Chemical Physics, 112(17):7307–7312, May 2000.
 61. E Evans and K Ritchie. Dynamic strength of molecular adhesion bonds. Biophysical Journal, 72(4):1541–1555, April 1997. PMID: 9083660 PMCID: PMC1184350.
 62. Keith James Laidler. Chemical kinetics. Harper & Row, 1987.
 63. Maria Francesca Iozzi, Trygve Helgaker, and Einar Uggerud. Assessment of theoretical methods for the determination of the mechanochemical strength of covalent bonds. Molecular Physics, 107(23-24):2537–2546, 2009.
 64. Michel Grandbois, Martin Beyer, Matthias Rief, Hauke Clausen-Schaumann, and Hermann E. Gaub. How strong is a covalent bond? Science, 283(5408):1727–1730, March 1999. PMID: 10073936.
 65. R. Krishnan, J. S. Binkley, R. Seeger, and J. A. Pople. Selfconsistent molecular orbital methods. XX. a basis set for correlated wave functions. The Journal of Chemical Physics, 72(1):650–654, January 1980.
 66. A. D. McLean and G. S. Chandler. Contracted gaussian basis sets for molecular calculations. i. second row atoms, $z=1118$. The Journal of Chemical Physics, 72(10):5639–5648, May 1980.
 67. Michael J. Frisch, John A. Pople, and J. Stephen Binkley. Selfconsistent molecular orbital methods 25. supplementary functions for gaussian basis sets. The Journal of Chemical Physics, 80(7):3265–3269, April 1984.
 68. Timothy Clark, Jayaraman Chandrasekhar, Gnther W. Spitznagel, and Paul Von Ragu Schleyer. Efficient diffuse function-augmented basis sets for anion calculations. III. the 3-21+g basis set for first-row elements, lif. Journal of Computational Chemistry, 4(3):294–301, September 1983.

69. Thom H. Dunning, Jr. Gaussian basis functions for use in molecular calculations. i. contraction of (9s5p) atomic basis sets for the firstrow atoms. The Journal of Chemical Physics, 53(7):2823–2833, October 1970.
70. Thom H. Dunning, Jr. and P. Jeffrey Hay. Gaussian basis sets for molecular calculations. In Henry F. Schaefer III, editor, Methods of Electronic Structure Theory, number 3 in Modern Theoretical Chemistry, pages 1–27. Springer US, January 1977.
71. Eric Magnusson and Henry F. Schaefer Iii. Multiple dtype basis functions for molecules containing second row atoms. The Journal of Chemical Physics, 83(11):5721–5726, December 1985.
72. J. Stephen Binkley, John A. Pople, and Warren J. Hehre. Self-consistent molecular orbital methods. 21. small split-valence basis sets for first-row elements. Journal of the American Chemical Society, 102(3):939–947, January 1980.
73. Mark S. Gordon, J. Stephen Binkley, John A. Pople, William J. Pietro, and Warren J. Hehre. Self-consistent molecular-orbital methods. 22. small split-valence basis sets for second-row elements. Journal of the American Chemical Society, 104(10):2797–2803, May 1982.